# Retrievals of Drizzle and Cloud Liquid Water Contents in Stratocumulus and Implications for Subgrid-scale Impacts on Model Autoconversion and Accretion Rates

Wei Zhao

A dissertation

submitted in partial fulfillment of the

requirements for the degree of

Doctor of Philosophy

University of Washington

2020

Reading Committee:

Roger T. Marchand, Chair

Qiang Fu, Chair

Robert Wood

Program Authorized to Offer Degree:

Atmospheric Sciences

University of Washington

## Abstract

# Retrievals of Drizzle and Cloud Liquid Water Contents in Stratocumulus and Implications for Subgrid-scale Impacts on Model Autoconversion and Accretion Rates

Wei Zhao

Chair of the Supervisory Committee:

Professor Roger T. Marchand

Professor Qiang Fu

Department of Atmospheric Sciences

Marine stratocumulus clouds (Sc) cover large areas of the Earth and have a substantial impact on the Earth's radiative balance by reflecting copious amounts of sunlight away from the Earth and emitting longwave radiation at a temperature close to surface. Cloud and precipitation (drizzle) liquid water content (hereafter CLWC and PLWC) are two of the most important microphysical properties of Sc which directly affect radiative transfer and the hydrological cycle, as well as play a critical role in many microphysical and planetary boundary layer processes. It is thus crucial to determine CLWC and PLWC accurately. Sc in many global climate models (GCMs)

are found to precipitate too frequently and too lightly which is likely due in part to the lack of information on the subgrid variability in CLWC and PLWC in the calculation of autoconversion and accretion rates. In most GCMs, the effects of subgrid variability have been either completely ignored or incorporated by multiplying the autoconversion and accretion rates (based on grid-mean values) by an enhancement factor to account for the subgrid variability. This dissertation aims to retrieve CLWC and PLWC jointly for Sc based on a millimeter wavelength radar, and to examine the nature of spatial variability in CLWC and PLWC and its impact on the autoconversion and accretion rates. In particular, we derive enhancement factors for autoconversion and accretion rates based on the radar observations, and examine how the enhancement factors change with different factors such as the length scale (size of a GCM grid) and the frequency of below-cloud precipitation.

In the first part of the dissertation (Chapter 2), the CLWC and PLWC are retrieved based on a combination of retrieval techniques including a novel Doppler spectra decomposition method that separates Doppler spectra into a cloud and a precipitation component. The radar Doppler spectra data from a vertically pointing Ka-band cloud radar, along with total liquid water path from a three-channel microwave radiometer (MWR) and radiosonde measurements are used in the retrievals. These observational data in this study were collected at the U.S. Department of Energy (DOE) Atmospheric Radiation Measurement (ARM) Eastern North Atlantic (ENA) site. At the scale of a single radar volume, the uncertainty of our retrieved PLWC is about an order of magnitude. By comparing to in-situ aircraft observations, we find on average they are in a good agreement. On the scale of one day, the uncertainty in the mean CLWC is estimated to be within 30% and the systematic errors in the mean PLWC are estimated to be less than 75%.

In the second part of the dissertation (Chapter 3), the variability in CLWC and PLWC and its effects on the grid-mean autoconversion and accretion rates are examined, specifically enhancement factors for autoconversion rate ($E_{auto}$) and accretion rate ($E_{accr}$). In many studies (and model implementations) enhancement factors are formulated under the assumption that variability in cloud and precipitation mixing ratio (water content divided by the air density) can be represented by a bivariate lognormal distribution with three key parameters: (i) the fractional standard deviation of the cloud-water mixing ratio, (ii) the fractional standard deviation of precipitating water mixing ratio, and (iii) the (cross) correlation coefficient (between cloud and precipitation mixing ratio). Therefore, both the enhancement factors and these three parameters are evaluated. Overall, we find that while our retrieved joint distribution is not truly a bivariate lognormal, this framework nonetheless works well given the correct values for the three key parameters.

In general, we find that $E_{auto}$ and $E_{accr}$ increase with grid size and have a maximum when precipitation fraction is about 0.4 – 0.6 (depending somewhat on how precipitation occurrence is defined and grid size). $E_{auto}$ stays relatively unchanged due to the assumption made in the retrievals that CLWC increases linearly with height in the cloud. $E_{accr}$ generally decreases from cloud base to cloud top although an increase in correlation of $q_c$ and $q_p$ and a decrease in the magnitude of the subgrid variability of $q_p$ have some offsetting effects. In addition, we find that $E_{auto}$ and $E_{accr}$ have little if any correlations with relative humidity (RH), lower tropospheric stability (LTS), and mean liquid water path (LWP) or mean cloud thickness. However, they are highly correlated with variability in of LWP, cloud thickness and cloud base, suggesting that any knowledge in subgrid variability might be useful in predicting $E_{auto}$ and $E_{accr}$.

# TABLE OF CONTENTS

# LIST OF FIGURES

# LIST OF TABLES

# ACKNOWLEDGEMENTS

First and foremost, I would like to thank both of my advisors, Roger Marchand and Qiang Fu, for the opportunity of studying in their groups and guiding me through my doctoral research. I have been extremely lucky to have both of them as advisors who are knowledgeable and supportive. Our weekly meetings, where I show my results and we discuss them, were both memorable and inspiring. These interactions have helped me to think critically and to acquire the professional knowledge about cloud microphysics, radiation and statistics which are important for my research. Roger and Qiang have also shared their personal experience with me and encouraged me to pursue what I want. I am grateful for the six years I have spent with them with all my heart. Many thanks also to Christopher Bretherton and Robert Wood for being my committee members. They are thoughtful and have generously provided insightful suggestions and comments which helped me dig deeper in my research. I also want to thank my GSR, Guozhong Cao, for all the questions and feedbacks.

I would also like to thank all other professors, staff and students in the Department of Atmospheric Sciences for making our department unbelievably friendly and supportive. All the social events, deserts, second Fridays and game nights constantly remind me how lucky I am to be part of the department. Special thanks to Erica Coleman for being the student advisor who was very patient with me, and to David Warren and Harry Edmon for solving all the problems related to computers and projectors.

I am very grateful to be in Grads 14. As an international student, they are my very first classmates and friends here in United States and have offered me enormous help and encouragement over these past few years. I also want to thank my officemates, Kelly Balmes, Hsiu-Hui Tseng and Mingcheng Wang for all the discussions about radiation, microphysics and coding. They are kind enough to endure my habit of sleeping at the desk. I thank my Chinese friends in the department for answering my questions and sharing food together.

Thank you to first responders, servicemen and servicewomen and healthcare professionals for fighting COVID-19 bravely on the frontline. In these challenging times, it is your dedications and sacrifices that keep me safe, informed and healthy.

At last but not the least, I would like to thank my parents and two sisters for their love, support and encouragement. Thank you to my wife for always believing in me.

# DEDICATIONS

To My family

# Chapter 1.

# Introduction

Marine boundary layer (MBL) clouds, especially stratocumulus clouds (Sc) are ubiquitous over subtropical ocean. These clouds are optically thick and can reflect solar radiation back to space [Randall et al., 1984]. Meanwhile, their low altitude makes them emit longwave radiation at a temperature that is close to sea surface temperature [Stephens and Greenwald, 1991; Hartmann and Doelling, 1991]. Sc therefore have a strong radiative cooling effect on the Earth and influence dramatically regional and global climate. A small increase in the coverage or reflectance (due for example to changes in the amount of liquid water) of MBL Sc has the potential to offset surface warming caused by increasing greenhouse gases in the global mean [Randall et al., 1984; Slingo, 1990], and intentionally increasing MBL clouds has been proposed as a possible geoengineering approach to mitigate the effects of anthropogenic emissions of carbon dioxide [Salter et al., 2008; Jones et al., 2009]. However, evidence suggests that (if anything) there is a positive low-level cloud feedback for Sc and Sc cloud cover will likely decrease with increased temperature [Clement et al., 2009; McCoy et al., 2017]. Nonetheless uncertainty in this result remains large for Sc [McCoy et al., 2017].

Marine Sc are maintained and governed by various microphysical and dynamical processes. The thermal emission at the top of Sc, which cools cloud top, is important not only for the radiation budget but also for generating and maintaining Sc. Cooling at the top enhances the strength of the capping inversion and drives convective instability and turbulent circulations within the

boundary layer [Lilly, 1968; Roach et al., 1982; Wood, 2012; Zheng et al., 2019]. The latent heat release in the updrafts and evaporative cooling in the downdrafts of the turbulent circulations can further fuel turbulence and strengthen entrainment at cloud top [Moeng et al., 1992; Zhou and Bretherton, 2018]. The entrainment of dry air from free troposphere evaporates liquid water and deepens or even decouples MBL [Randall, 1984; Wang and Albrecht, 1994; Mellado, 2017]. Surface fluxes are important for providing moisture which condenses on aerosols to form cloud particles. Precipitation (here meaning particles large enough to have an appreciable terminal fall velocity, greater than about ~50 microns in diameter) is largely formed and grows by collisions of and coalescence with small cloud particles. In bulk microphysical models, this is represented by the process of autoconversion (the collision of small cloud droplets to form larger precipitation drops) and accretion (the collection of cloud droplets by falling precipitation drops). Precipitation depletes cloud liquid water and aerosols, releases latent heat in the cloud, cools and moistens the region under clouds via evaporation which helps stabilize the cloud and reduce the strength of turbulence [Comstock et al., 2005; Wang et al., 2009; Wood et al., 2012; Seinfeld et al., 2016]. The concentration of aerosols can affect the size of cloud droplets and thereby the cloud albedo (reflectance), cloud lifetime and the formation of precipitation [Twomey 1977; Albrecht 1989; Rosenfeld 1999; Fan 2016]. The interactions among aerosol, cloud, precipitation and radiation, and their effects on climate are important aspects of Sc physics.

Cloud and precipitation liquid water content (hereafter CLWC and PLWC) are fundamentally important microphysical properties, impacting aerosol-cloud-precipitation-radiation interactions. Accurate knowledge of the vertical profile of CLWC and PLWC is vital for studying these interactions and evaluating how well large eddy simulation (LES) models and global climate

models (GCMs) predict clouds. Arguably, in situ aircraft observations of Sc can provide the most accurate measurements of cloud liquid water content as part of field campaigns such as the Altantic Stratocumulus Transition Experiment (ASTEX) [Albrecht et al., 1995], Dynamics and Chemistry of Marine Stratocumulus (DYCOMS-II) [Stevens et al., 2003] and Aerosol and Cloud Experiments in the Eastern North Atlantic (ACE-ENA) [Wang et al., 2016]. However, long records and high spatial coverage of the aircraft measurements are not possible. Passive satellite observations like from Moderate Resolution Imaging Spectroradiometer (MODIS), while they have global scale coverages and long data records, contain little information of the vertical distribution of the CLWC and PLWC [King et al., 2012]. The cloud profiling radar (CPR) on CloudSat [Stephens et al., 2008] has a greater ability to reveal the vertical structure, however, ground clutter contaminates the spaceborne radar signals below 1 km making it hard to study cloud and light precipitation in MBL [Hudak et al., 2008; Christensen et al., 2013]. In this dissertation, ground-based observations collected at the U.S. Department of Energy (DOE) Atmospheric Radiation Measurement (ARM) Eastern North Atlantic (ENA) site are used to retrieve CLWC and PLWC. The ARM observatory is heavily instrumented including a Ka band ARM Zenith Radar (KAZR), micropulse lidar (MPL), microwave radiometer (MWR) and so forth. These instruments have high resolution and sensitivity and can help fill the large gap between in situ and satellite datasets.

Many studies have been conducted to retrieve CLWC or PLWC using ground-based observations. For example, Atlas [1954] and Fox and Illingworth [1997] estimated CLWC profiles based on solely the radar reflectivity. Frisch et al. [1998] retrieved CLWC by distributing the total liquid water path (TLWP) estimated from a MWR proportionally following the vertical profile of radar reflectivity. However, these simple methods are only applicable to

non-drizzling clouds since precipitation droplets will typically contribute much more to radar reflectivity (while containing much less liquid water) than cloud particles [Matrosov et al., 2004; Kogan et al., 2007]. By taking advantage of the fact that the attenuation of millimeter cloud radar signals is proportional to CLWC while affected little by PLWC and the attenuation increases with radar frequency, Hogan et al. [2005] retrieved CLWC profiles using differential absorption in collocated 35 GHz and 94 GHz radar returns. Unfortunately, from the retrieval perspective, cloud and precipitation particles coexist in the majority of radar volumes. Several studies over the years have focused on radar Doppler spectra (essentially radar return power as a function of particle velocity) to obtain information on both clouds and precipitation (since precipitation is by definition composed of those particles large enough to sediment). Relatively recently, for example, Luke and Kollias [2013] attempted to separate cloud and precipitation contribution to radar signals by decomposing Doppler spectra. The authors shifted consecutive Doppler spectra to coincide their spectral peaks, averaged the power in each velocity bin and subtracted cloud component by assuming it has a Gaussian distribution. The disadvantage of this approach is that it is limited to cases with light precipitation (e.g., near the onset of precipitation). Jointly retrieval of CLWC and PLWC was achieved by Fielding et al. [2015] and Rusli et al. [2017] using physical forward models to simultaneously fit observations from cloud radar, lidar and other passive instruments. However, lidar signals are quickly attenuated in cloud making it hard to retrieve PLWC accurately, except near cloud base and the same problem exists in the method proposed by O'Connor [2005] to derive PLWC using cloud radar and lidar observations based on the theory that the ratio of the radar to lidar backscatter power is proportional to the fourth power of mean particle size.

In Chapter 2, we aim to retrieve CLWC and PLWC jointly using ground-based observations collected at the ARM ENA site. In the work, a combination of techniques is applied and the results are compared to in-situ aircraft observations.

The simultaneous retrieval of CLWC and PLWC in Sc is essential to understand autoconversion and accretion. In bulk microphysical models autoconversion and accretion rates are typically represented using a power-law formulation, given in the equations below. We provide more background on this in Chapter 3.

$$M_{auto} = a_{au} N^{b_N} {q_c}^{b_{au}} \tag{1.1}$$

$$M_{accr} = a_{ac} {q_c}^{b_{acc}} {q_p}^{b_{acp}} \tag{1.2}$$

Here, $M_{\text{auto}}$ and $M_{accr}$ are the autoconverstion rate and accretion rate, respectively, with units of kg kg$^{-1}$ s$^{-1}$. $q_c$ and $q_p$ are cloud and precipitation liquid water mixing ratio (CLWC/PLWC divided by air density), respectively. N is the cloud droplet number concentration and is considered as a constant here. $a_{au}$ $b_N$, $b_{au}$ $a_{ac}$, $b_{acc}$ , and $b_{acp}$ are constant (power-law) coefficients.

Typically, $b_{au}$, $b_{acc}$ and $b_{acp}$ are larger than 1, and the autoconversion and accretion rates are non-linear. Due to this nonlinearity, one cannot (or should not) calculate the grid-mean autoconverstion and accretion rates using the grid-mean values of $q_c$ and $q_p$. That is

$$\overline{M_{auto}} = \overline{a_{au} N^{b_N} {q_c}^{b_{au}}} \neq a_{au} \bar{N}^{b_N} \bar{q_c}^{b_{au}} \tag{1.3}$$

$$\overline{M_{accr}} = \overline{a_{ac} {q_c}^{b_{acc}} {q_p}^{b_{acp}}} \neq a_{ac} \bar{q_c}^{b_{acc}} \overline{q_p}^{b_{acp}} \tag{1.4}$$

However, conventional GCMs typically either ignore the subgrid variability or account for it by multiplying the autoconversion and accretion rates calculated using grid-mean $q_c$ and $q_p$ by a constant. In Chapter 3, we examine the subgrid variability of CLWC and PLWC based on retrievals and their impacts on grid-mean autoconversion and accretion rates. Conclusions will be summarized in Chapter 4.

# Chapter 2.

# Drizzle and Cloud Liquid Water Content Retrievals in Marine Stratocumulus Clouds

## 2.0 Overview

We retrieve precipitation (drizzle) liquid water (PLWC) and cloud liquid water contents (CLWC) simultaneously for stratocumulus clouds using data collected at U.S. Department of Energy Atmospheric Radiation Measurement Eastern North Atlantic (ENA) site. Specifically, Doppler spectra from a vertically pointing Ka-band cloud radar, microwave radiometer total (cloud + precipitation) liquid water path (TLWP), and radiosonde thermodynamic profiles are used. The Doppler spectrum for a given radar volume is separated into cloud and precipitation portions so that CLWC and PLWC can be retrieved. This spectral decomposition technique is typically applicable to less than 20% of the cloudy volumes measured by the radar because it requires that the Doppler spectrum has distinct bimodality. Consequently, a "tuned regression" approach, where a power law relationship between PLWC and reflectivity is derived from those radar volumes where the decomposition is possible on a case-by-case basis, and is applied to the remaining cloudy volumes. CLWC, on the other hand, is retrieved assuming a linearly increasing profile in cloud constrained by the microwave radiometer TLWP. A comparison with aircraft observations for two flights during the Aerosol and Cloud Experiment at ENA demonstrates that the retrieval algorithm works reasonably well. On the scale of one day, the

uncertainty in the mean CLWC is estimated to be within 30% and the systematic errors in the mean PLWC are estimated to be less than 75%, despite of the fact that for each individual radar volume, the uncertainty can be up to one order of magnitude. The simultaneous determination of PLWC and CLWC are vital to study autoconversion and accretion processes, which are examined in next chapter.

## 2.1 Introduction

Marine boundary layer (MBL) clouds are pervasive over the eastern subtropical oceans and in midlatitude regions (especially in the winter), where the areal coverage can reach 50% in the annual mean [Klein and Hartmann, 1993; Hahn and Warren, 2007; Wood, 2012]. In these regions, the majority of low clouds are stratocumulus clouds (Sc) [Warren et al., 1988; Lohmann, 2009], which are favored by a combination of large-scale subsidence and relatively cold sea surface temperature that leads to a strong temperature inversion that caps a moist boundary layer [Lilly, 1968; Klein and Hartmann, 1993; Wood, 2012]. Marine Sc have a strong cooling impact by reflecting incoming shortwave radiation back to space [Randall et al., 1984; Hartmann and Doelling, 1991; Chen et al., 2000] while emitting nearly the same amount of longwave radiation to space as the surface would have in the absence of clouds [Stephens and Greenwald, 1991; Hartmann and Doelling, 1991]. Since marine Sc are of crucial importance to the energy balance on Earth, it is thus essential to accurately represent Sc in global climate models (GCMs).

The amount of cloud and precipitation liquid water contents (hereafter, CLWC and PLWC respectively) and their vertical profiles have a large impact on radiative effects of Sc [Matrosov et al., 2004; Bender et al., 2016]. Meanwhile, CLWC and PLWC play important roles in the Sc microphysical processes. For example, CLWC is closely related to the cloud and aerosol

interactions, turbulence that couples cloud layer to surface moisture, latent heat release and evaporative cooling associated with the internal convection circulation and the entrainment of the dry air at the top of the cloud [Wood, 2012; Fan et al., 2016; Eastman et al., 2017]. Precipitation on the other hand releases latent heat in the cloud, cools and moistens under the cloud via evaporation which helps stabilize the cloud and reduce the strength of turbulence [Comstock et al., 2005; Wood et al., 2012; Wang et al., 2009; Seinfeld et al., 2016]. Autoconversion is the collision of cloud droplets to form larger precipitation drops, while accretion rate is the collection of cloud droplets by falling precipitation drops, which increases precipitation particle size and water content. CLWC and PLWC are related to these two microphysical processes and are often used in their parameterization in GCMs which determines the precipitation generation [Beheng, 1994; Khairoutdinov and Kogan, 2000; Yuan et al, 2006; Lee and Baik, 2017]. However, the lack of information about the subgrid variability of CLWC and PLWC in GCMs can cause biases in the calculated autoconversion and accretion rates which may lead to simulated precipitating too frequent but too light as reported in the literature [Stephens et al., 2010; Lebstock et al., 2013; Boutle et al., 2014; Kendon et al., 2019]. The effects of subgrid variability on the microphysical process rates are studied in next chapter. The knowledge in both mean and subgrid variability of CLWC and PLWC requires accurate measurements or retrievals of CLWC and PLWC, which can help us understand in depth microphysical processes in clouds, and evaluate and improve climate models [Bretherton et al., 2004; Stephens, 2005; Yuan et al., 2006; Leinonen et al., 2016].

In situ observations of CLWC and PLWC from aircraft such as in the Dynamics and Chemistry of the Marine Stratocumulus (DYCOMS) [Lenschow et al., 1988; Stevens et al., 2003] and Aerosol and Cloud Experiments in the Eastern North Atlantic field campaigns (ACE-ENA)

[Wang et al., 2016] are no doubt the best source of information for cloud and precipitation microphysical studies. But aircraft in situ sampling volumes are limited and can characterize only a small portion of any individual cloud or system. In order to obtain more complete and more routine observations, many remote sensing methods have been developed to retrieve CLWC or PLWC using ground-based observations. Radar reflectivity factor (Z) is one of the most widely used observations. For example, Atlas [1954] and Fox and Illingworth [1997] developed empirical relationships (typically power-law formulation) to retrieve CLWC based solely on the radar reflectivity. However, the observed radar reflectivity can have contributions due to scattering from both cloud and precipitation particles and is often dominated by the largest particles present [Fox and Illingworth, 1997; Wang and Geert, 2003; Matrosov et al., 2004; Kogan et al., 2007]. In particular for liquid phase condensate, when the total reflectivity is greater than about -10 dBZ one can use an empirical relationship to estimate PLWC with little concern regarding the contribution from cloud particles [Frisch et al., 1995; Hagen and Yuter, 2013]. However, for total reflectivity values below -10 dBZ both cloud and precipitation may contribute significantly to the radar reflectivity, making it difficult to apply a reflectivity-to-PLWC or reflectivity-to-CLWC relationship unless one has other information that makes it clear that only one or the other is present. For example, lidar data are often used to identify cloud base and the reflectivity observed below cloud base can be attributed to precipitation. This problem persists in the algorithm that combines radar with microwave radiometer (MWR) [Frisch et al., 1998] where the MWR estimate of total liquid water path (TLWP) (the vertical integral of total liquid water content) is used to constrain the CLWC profile derived from the radar reflectivity. This approach is limited to cloud with little or no precipitation.

In order to retrieve both CLWC and PLWC in the drizzling clouds, more information than reflectivity and microwave emission is needed. One approach is to utilize lidars. For example, O'Connor et al. [2005] used measurements from a millimeter cloud radar and a lidar to derive PLWC based upon the idea that the lidar backscatter is related to the second power of droplet diameter while radar backscatter is related to the sixth power. Using physical forward models, Fielding et al. [2015] and Rusli et al. [2017] were able to retrieve vertical profiles of CLWC and PLWC jointly that best fit ground-based millimeter radar and lidar observations. However, the lidar measurements are rapidly attenuated by cloud droplets, so this method limits the PLWC and CLWC retrievals only near the base of the cloud. Another approach is to utilize radar Doppler spectra. A Doppler spectrum is the distribution of backscatter-power-weighted radial velocity of hydrometeors which carries much more information than the widely used moments such as reflectivity, Doppler velocity and spectral width [Kollias et al., 2002; Shupe et al., 2004; Shupe et al., 2008; Luke et al., 2010; Kollias et al., 2011a; Kollias et al., 2011b; Luke et al., 2013]. Gossard et al. [1997] and Babb et al. [1999] deconvolved the measured Doppler spectra from a millimeter radar to separate turbulence, cloud and precipitation modes and subsequently retrieved cloud properties. However, their separation can be seriously subjective especially when the peak of cloud component lost in the precipitation component [Gossard et al., 1997; O'Connor et al., 2005]. For Sc, when both cloud droplets and drizzle droplets coexist in a volume and have large differences in particle size distribution, the Doppler spectrum would exhibit distinct bimodality with cloud and drizzle modes clearly separable [Kollias et al., 2001; Luke et al., 2013]. Since the fall velocity of cloud droplets is very small, they can serve as the tracers of air motion [Gossard et al., 1997; Kollias et al., 2001; Shupe et al., 2004; Luke et al., 2013]. Luke et al. [2013] separated cloud and drizzle spectra by artificially aligning the peaks of

several consecutive Doppler spectra, averaging them and subtracting cloud contributions from the spectra. However, this method requires a relatively long time average and can only be implemented at the precipitation onset stage (i.e. when the drizzle component is small).

Here we build upon these previous ideas to separate the cloud and drizzle components and retrieve PLWC by using a Doppler spectra decomposition method when Doppler spectra exhibit distinct bimodality. For radar volumes where Doppler spectra are not separable, a tuned regression method is applied [Matrosov, 1999]. CLWC is retrieved based upon the assumption that CLWC increases linearly with height. The data used and the retrieval methods are described in sections 2.2 and 2.3, respectively. Section 2.4 presents two case studies and compares retrieval results with airborne observations. Uncertainty estimates are given in section 2.5, with additional discussions and conclusions in section 2.6.

## 2.2 Data

In this study, observations are taken from several instruments at the Department of Energy (DOE) Atmospheric Radiation Measurement program (ARM) Eastern North Atlantic (ENA) site, including a cloud radar, a lidar, microwave radiometer, and radiosondes. All of these data are publicly available from the ARM data archive. The ENA site sits on Graciosa Island in the Azores (39.09ºN, 28.03ºW) in the northeastern Atlantic Ocean. It experiences both stratocumulus and cumulus under a wide range of weather conditions and thus serves a good test bed to study these clouds [Dong et al., 2014]. Specific ARM data used are: (1) cloud boundaries, reflectivity factors, Doppler velocity and spectral width from the Active Remote Sensing of Clouds (ARSCL) Value-Added Product (VAP) [Clothiaux et al., 2000; DOI:10.5439/1052058], (2) radar Doppler spectra [Kollias et al., 2011; DOI:10.5439/1025218], (3) TLWP derived from a

three-channel microwave radiometer [Cadeddu et al., 2009; DOI:10.5439/1025248], (4) temperature and pressure profiles from the interpolated Sonde VAP product [DOI:10.5439/1095316], and aircraft-measured particle size distribution from the (5) Fast Cloud Droplet Probe (FCDP) [DOI:10.5439/1419322] and from (6) the 2-Dimensional Stereo Probe (2DS) [DOI:10.5439/14174720] collected during the Aerosol and Cloud Experiments in the Eastern North Atlantic (ACE-ENA) field campaign [Wang et al., 2016].

The ARSCL product combines measurements from a Vaisala ceilometer, micropulse lidar, and Ka band ARM Zenith Radar (KAZR). The KAZR rotates through a sequence of operational modes with varying pulse widths and pulse repetition frequencies to optimize the radar measurements for variety of cloud and precipitation types [Chandra et al., 2015]. The ARSCL product merges these mode data to provide a best estimate for the reflectivity, Doppler velocity and spectral width on a fixed grid with a grid spacing of 30 m in the vertical and 4 seconds in time. This sampling rate is significantly better than the last generation radar at this site (10 s), which helps considerably in the application of microphysical retrievals by reducing the impact of turbulent broadening. The ARSCL data processing also includes a correction to the measured reflectivity and Doppler velocities for gaseous attenuation and velocity folding, respectively. The ARSCL product contains a cloud (or hydrometeor) mask that distinguishes radar reflectivity due to clouds and precipitation from clutter or noise, and determines cloud boundaries based on combinations of the radar, ceilometer and micropulse lidar data. The radar is a vertically-pointing 35 GHz system that is calibrated via an external corner reflector. Kollias et al. [2019] have recently evaluated the calibration of the ARM radar systems against CloudSat spaceborne 94 GHz cloud radar. For ENA, they found that a calibration offset of the KAZR can reach up to 5.2 dB. We have added a calibration correction based on Kollias et al. 2019 to the reflectivity of

the KAZR. The top three panels in Fig 2.1 show an example of the ARSCL product reflectivity, mean Doppler velocity and Doppler spectral width for a Sc observed on July 18, 2017 from the ENA KAZR. Here cloud base (from lidar) is denoted by the black dots. Note that negative velocities in Fig 2.1(b) correspond to particles moving upward (away from the radar) and positive velocity correspond to particles moving downward (towards the radar). We will use this case to illustrate retrieval methods and results in Section 2.3, partly because this cloud system was sampled in situ during the ACE--ENA field campaign. We present a comparison of the retrieved and in situ data in section 2.4.

The KAZR collects Doppler spectra during the general mode which was designed to minimize the effects of internal turbulence and wind shear on the spectra [Kollias et al., 2011]. Reflectivity, mean Doppler velocity and Doppler spectral width are the first three moments of a Doppler spectrum. The general mode is run about every 2 s so typically there are two Doppler spectra associated with each ARSCL time-sample, which we average, to reduce noise. Examples of Doppler spectra are shown in Fig 2.3 as the black line with the same velocity convention as Fig 2.1(b).

The TLWP used here is retrieved from a three-channel MWR which measures passively emitted microwaves brightness temperature at three channels of 23.834, 30 and 89 GHz. The three-channel MWR was deployed to replace an old two-channel MWR and has better temperature stability and better performance especially under drizzling conditions [Cadeddu et al., 2013]. Precipitable water vapor and TLWP are retrieved from the MWR using a neural network approach [Cadeddu et al., 2009] with a temporal sampling of 2 to 3 s. Fig 2.1(d) shows the time series of TLWP on July 18, 2017. The data collected when the MWR is wet are discarded, as will be discussed further in Section 2.3.

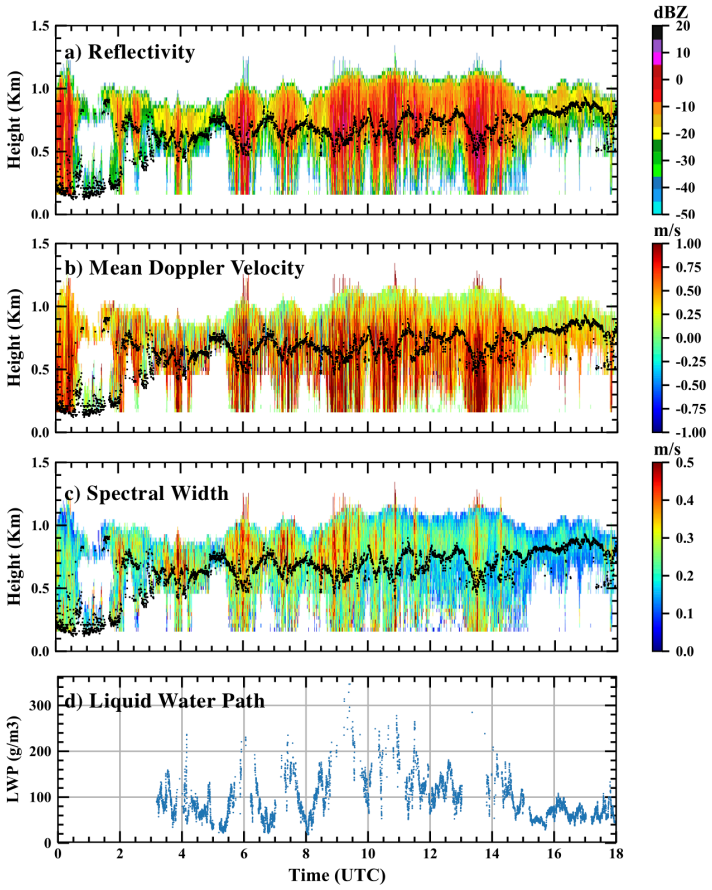


*Figure 2.1 Observations at the Eastern North Atlantic (ENA) site on July 18, 2017. The (a) reflectivity, (b) mean Doppler velocity and (c) spectral width are measured by the Ka band ARM Zenith Radar (KAZR) and the black dots indicate cloud base. The (d) liquid water path is retrieved from a three-channel microwave radiometer (MWR) with data removed when drizzle reaches to the ground.*

The Interpolated Sonde VAP product is obtained by interpolating radio sounding data onto a fixed time-height grid from surface to around 20 km using a variety of interpolation schemes [Toto and Jensen, 2016]. The resulting sampling of the VAP data is 1 min in time and 20 m in the vertical. Unlike the ARM merged sounding VAP data product, the interpolated sonde product does not incorporate ECMWF model outputs. In this study only profiles of temperature and pressure are used.

The ACE-ENA field campaign had two intensive operation periods, specifically June-July 2017 (summer) and January-February 2018 (winter). During the experiment both a FCDP and 2DS were mounted on the ARM Aerial Facility (AAF) Gulfstream-159 (G-1). The FCDP measures cloud particle size distributions from 1 to 50 μm in diameter with a resolution varying from 1.5 μm to 3 μm, while the 2DS measures particle concentration for particles between 10 and 3000 μm with a resolution varying from 10 μm to 200 μm. The temporal sampling of the airborne data is 1 s. In our retrieval evaluation we calculate CLWC using all particles measured by the FCDP including all particles below 50 μm in diameter, and we calculate PLWC using the 2DS for particles larger than 100 μm due to ignorance of small particles in our retrievals as described below. Changing the PLWC size threshold from 100 to 50 μm in the 2DS increases the PLWC by as much as 20%.

## 2.3 Retrieval Methods

In this section, we describe the techniques we use to achieve our objective of determining both CLWC and PLWC in Sc. A schematic diagram of our retrieval scheme is depicted in Fig 2.2. We start in section 2.3.1 by describing a technique introduced by Frisch et al. [1995] that was developed to derive PLWC radar volumes that contain only drizzling particles, and nominally would be applied below cloud or perhaps to radar volumes where the radar measurements are completely dominated by precipitating particles. We expand on this approach with information obtained from a Doppler spectra separation method for PLWC, so that it can be applied both within cloud and below. In section 2.3.2, the Doppler spectra separation method is introduced and applied for a subset of radar resolution volume (range gates) in the cloud where the Doppler spectra have a distinct bimodal distribution. This separation essentially decomposes a Doppler spectrum into cloud droplet component and precipitation component. A tuned regression

method following the idea of Matrosov [1999] is then adopted to retrieve PLWC at range gates where Doppler spectra are not separable. The core of the PLWC retrieval applied below and in cloud is similar and requires adjustments for the presence of air motions. This is necessary because the radar observed Doppler velocity is due both to particle sedimentation (fall velocity) and air motions, and in order to relate the measured Doppler velocity to particle fall velocity the impact of air motion must be removed. We derive air motions directly from the Doppler spectra in section 2.3.2, while below-cloud, we use a method developed by Orr and Kropfli [1999] that is described in section 2.3.3. Once the PLWC is obtained we retrieve the CLWC based on the idea that the cloud liquid water content in Sc increases linearly from cloud base to cloud top, with details given in section 2.3.4.

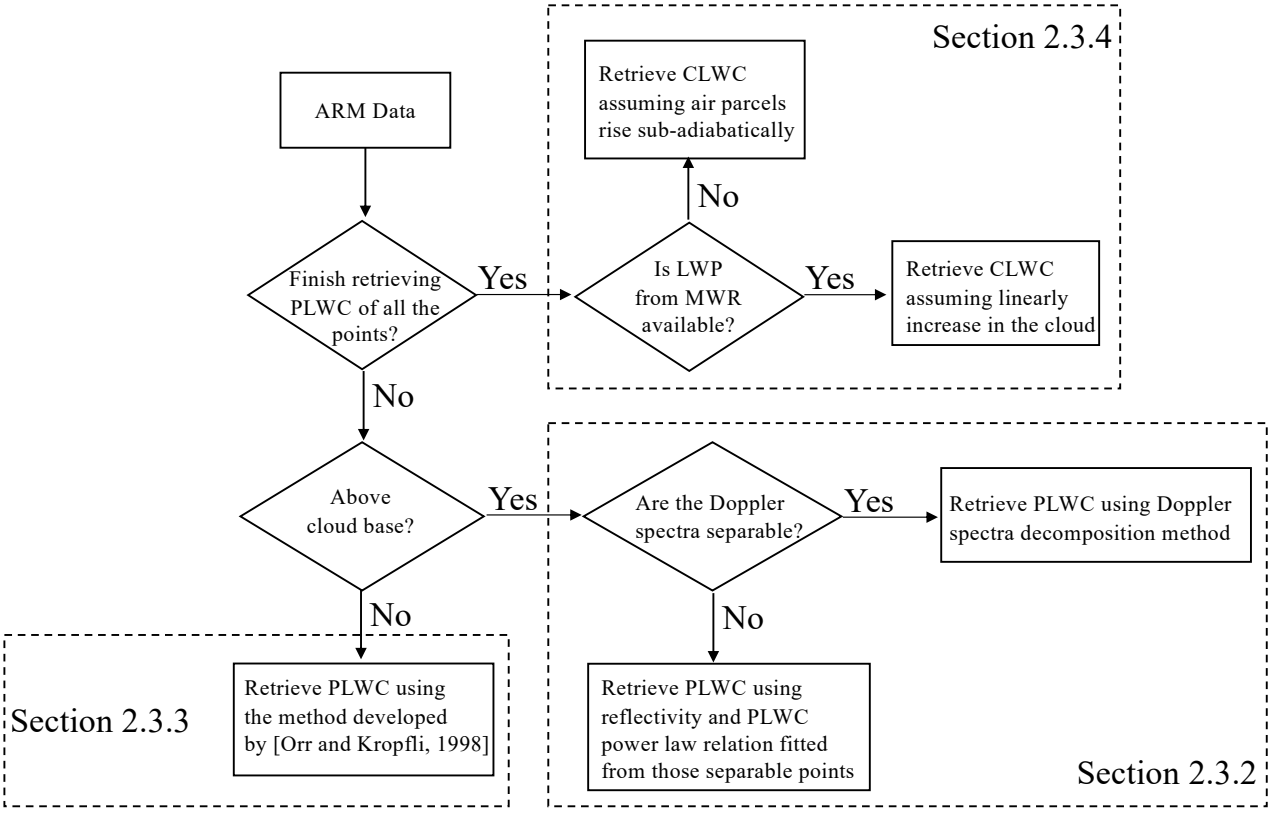


*Figure 2.2 Workflow of retrieving precipitation (drizzle) liquid water content (PLWC) and cloud liquid water content (CLWC). Algorithms in the dashed rectangles are described in detail in the corresponding sections in the chapter.*

### 2.3.1 ***Background: The Basics of PLWC Retrieval***

In this section, a technique to determine PLWC by Frisch et al. [1995] is presented briefly. In Frisch's approach, the drizzle droplet number distribution is assumed to be lognormal,

$$n(x) = \frac{N}{\sigma_x\sqrt{2\pi}} \exp - \left[\frac{(x-x_0)^2}{2\sigma_x{}^2}\right] \qquad (2.1)$$

where x and $x_0$ are the logarithm of droplet radius (r) and modal radius ($r_0$) in microns, respectively. N is the total number concentration of droplets per unit volume and $\sigma_x$ is the logarithmic width of the distribution.

Under this assumption, the PLWC can be expressed as:

$$q_l = \left(\frac{4\pi}{3}\right)\rho_w \int r^3 n(x)dx = \left(\frac{4\pi}{3}\right)\rho_w N r_0{}^3 \exp\left(\frac{9\sigma_x{}^2}{2}\right) \quad (2.2)$$

where $\rho_w$ is the density of liquid water. Note that for a typical drizzle droplet number distribution with $r_0$ = 120 μm and $\sigma_x$ = 0.35 μm, the contribution to PLWC from particles with radius smaller than 50 μm is negligible. Eq. (2.2) shows that three parameters $r_0$, N and $\sigma_x$ in the distribution need to be determined to calculate PLWC. In principle, these three unknowns can be determined using the reflectivity factor, mean Doppler velocity and spectral width measured by a radar in principle, however noise and turbulent air motions makes this difficult. We will discuss the difficulties later in the chapter.

Under the assumption of Rayleigh scattering, the radar reflectivity factor is given by (defined as) the sixth moment of the size distribution, which for a lognormal distribution is:

$$Z = \int D^6 n(D)dD = 2^6 \int r^6 n(x)dx = 2^6 N r_0^6 \exp(18\sigma_x{}^2) \quad (2.3)$$

The units of reflectivity (or more properly called the reflectivity factor), Z, are nominally $m^3$, but conventionally, the units are typically given $mm^6 m^{-3}$ in decibels (dBZ). The two variables have the following relation:

$$dBZ = 10\log(Z) + 180 \quad (2.4)$$

Following Frisch et al. [1995], in the absence of any air motion (that is, in the absence of any motion other than that due to sedimentation), the mean Doppler velocity can be written as:

$$V_D = \frac{\int V_f r^6 n(x)dx}{\int r^6 n(x)dx} \quad (2.5)$$

where $V_f$ is particle fall velocity which depends on the particle mass. Eq. (2.5) shows that once $V_f$ is specified, $V_D$ can be determined. Eq. (2.5) neglects the effect of air motions, whether updrafts or downdrafts (i.e., motions on scales larger than the radar resolution volume) or

turbulent motions (i.e., motions on scales smaller than the radar resolution volume). We will explain how we account for air motions later in the chapter. Gossard et al. [1990] found that when 45 μm < r < 400 μm and 0.3 m/s < $V_f(r)$ < 3 m/s, there is a linear relation between r and $V_f$ in a form:

$$r = aV_f + b \tag{2.6}$$

where a and b are $1.2\times10^{-4}$ s and $1.0\times10^{-5}$ m, respectively.

Substituting Eq. (2.6) to Eq. (2.5), one finds the mean Doppler velocity is given by

$$\mathrm{V_D} = \frac{r_0 \exp\left(\frac{13{\sigma_x}^2}{2}\right) - b}{a} \tag{2.7}$$

Likewise, following Frisch, the Doppler spectral width is given by:

$$\sigma_v^2 = \frac{\int V_f^2 \mathrm{r}^6 n(x)dx}{\int \mathrm{r}^6 n(x)dx} - V_D^2 = \left(\frac{r_0}{a}\right)^2 \exp(13{\sigma_x}^2)[\exp({\sigma_x}^2) - 1] \tag{2.8}$$

Eqs. (2.3), (2.7) and (2.8) can be solve for $\sigma_x$, $\mathrm{r}_0$ and N as shown below.

$$\sigma_x = \left[\ln\left(1 + \frac{\sigma_v^2}{\left(V_D + \frac{b}{a}\right)^2}\right)\right]^{\frac{1}{2}} \approx \frac{\sigma_v}{V_D} \tag{2.9}$$

$$\mathrm{r}_0 = (aV_D + b)\exp\left(\frac{13{\sigma_x}^2}{2}\right) \tag{2.10}$$

$$N = \frac{Z}{2^6 r_0^6 \exp(18{\sigma_x}^2)} \tag{2.11}$$

Substituting Eqs. (2.9), (2.10) and (2.11) into Eqs. (2.2) and (2.4), we have

$$\mathrm{PLWC} = \frac{1}{(aV_D)^3} 10^{\frac{dBZ - 132 + 26\left(\frac{\sigma_v}{V_D}\right)^2}{10}} \tag{2.12}$$

Based upon Eq. (2.12), PLWC can be retrieved with measured radar reflectivity factor, mean Doppler velocity and spectral width for precipitating particles. However, as noted above, the mean Doppler velocity and Doppler width measured by KAZR do have significant contributions

from air motions which has to be separated. We use different strategies to do this in and below clouds, which are presented in section 2.3.2 and 2.3.3, respectively.

### 2.3.2 *Retrieval of in-cloud PLWC*

In the cloud, all of the radar moments are due to a combination of cloud and precipitation with higher moments also affected by air vertical motion. Cloud particles often dominate the radar measurement at the top of Sc and drizzle particles at the bottom. Cloud particles are small and have a fall velocity of only several centimeters per second. However, as shown in Fig 2.1(b), at any instant negative velocities (i.e., particles moving up and away from radar) are frequently observed because of air updrafts. Since Eq. (2.12) was derived by assuming that mean Doppler velocity has no component from air velocity, air velocity has to be subtracted from measured Doppler velocity.

Here a Doppler spectra separation method is implemented to separate the measured Doppler spectra into a cloud and a drizzle component. The fall velocity of the precipitation is then determined by subtracting the mean Doppler velocity of the cloud component from the drizzle component. The critical idea here is that the small droplets have almost no sedimentation (a few cm/s at most) and are essentially passive tracers of the air motion. The black line in Fig 2.3(a), Fig 2.3(b) and Fig 2.3(c) show example cases where the Doppler spectra are separable. The power is given in Decibel-milliwatt (dBm) which is equal to 10 times base 10 logarithm of the power in milliwatt (mW). The noise level of the spectra (black horizontal dash line) is determined using the method detailed in Hildebrand and Sekhon [1974] and only signals above the noise level are considered. For a radar volume containing only cloud droplets or drizzle droplets, the Doppler spectrum typically appears to be normally distributed. However, when a

mixture of cloud and drizzle droplets exists in the radar volume and each category has a substantial radar return, the spectrum can have a bimodal distribution. In Fig 2.3(a), the cloud mode (blue line) is dominant. The cloud particles fall very slowly so the location of the peak (left red dash line) provides a good estimate for the air updraft or downdraft velocity. In this example, the updraft is 1.5 m/s. Note that the distribution (width) of both modes is expected to be broadened by turbulent air motion (that is, air motions which are on spatial and temporal scales that are small compared to the radar resolution volume and measurement interval). However, we assume and that the turbulent broadening will not affect the mean fall speed of either the cloud or precipitation particles. Under this assumption, the width of the cloud mode is due almost entirely to small scale turbulent motions that we expect have no preferred orientation. And indeed, we only rarely see unsymmetrical spectra from regions containing only cloud particles. For the precipitation mode, the width is mainly due to the size distribution of drizzle particles as the broadening due to turbulence, radar beamwidth and wind shear, on average, contributes only about 15% of the distribution width based on the method described in O'Connor et al [2005]. In Fig 2.3(b), the cloud and drizzle modes contribute approximately equally to reflectivity since they have very similar peak magnitudes and Fig 2.3(c) shows an example where the drizzle component is dominant. The cloud and drizzle components are determined by minimizing the mean square error between the sum of the two normally distributed components and the original Doppler spectra. The procedure is as follows:

a) Radar volumes with reflectivity smaller than -30 dBZ (which are above cloud base) are assumed to contain only cloud droplets. In the event that precipitation is present the amount would be very small (PLWC < $10^{-3}$ g/m3) and for even the ARM KAZR there would be insufficient signal-to-noise-ratio to apply any Doppler spectra processing.

b) We assume the cloud and precipitation modes in the Doppler spectra can be well represented by a sum of two Gaussian distributions as $P_c = \frac{A_c}{\sqrt{2\pi{\sigma_c}^2}} e^{\frac{(v-v_c)^2}{2{\sigma_c}^2}}$ and $P_d = \frac{A_d}{\sqrt{2\pi{\sigma_d}^2}} e^{\frac{(v-v_d)^2}{2{\sigma_d}^2}}$, respectively, where $A_c$ $(A_d)$, $v_c$ $(v_d)$ and $\sigma_c$ $(\sigma_d)$ are magnitude, mean and standard deviation of the cloud (drizzle) component.

c) The cost function $[10\log(P_c + P_d) - 10\log(P_o)]^2$ is numerically minimized, where $P_o$ is total power measured by the radar and only signals above the noise level are considered. The minimization yields best-estimate values for the six Gaussian parameters given in step b.

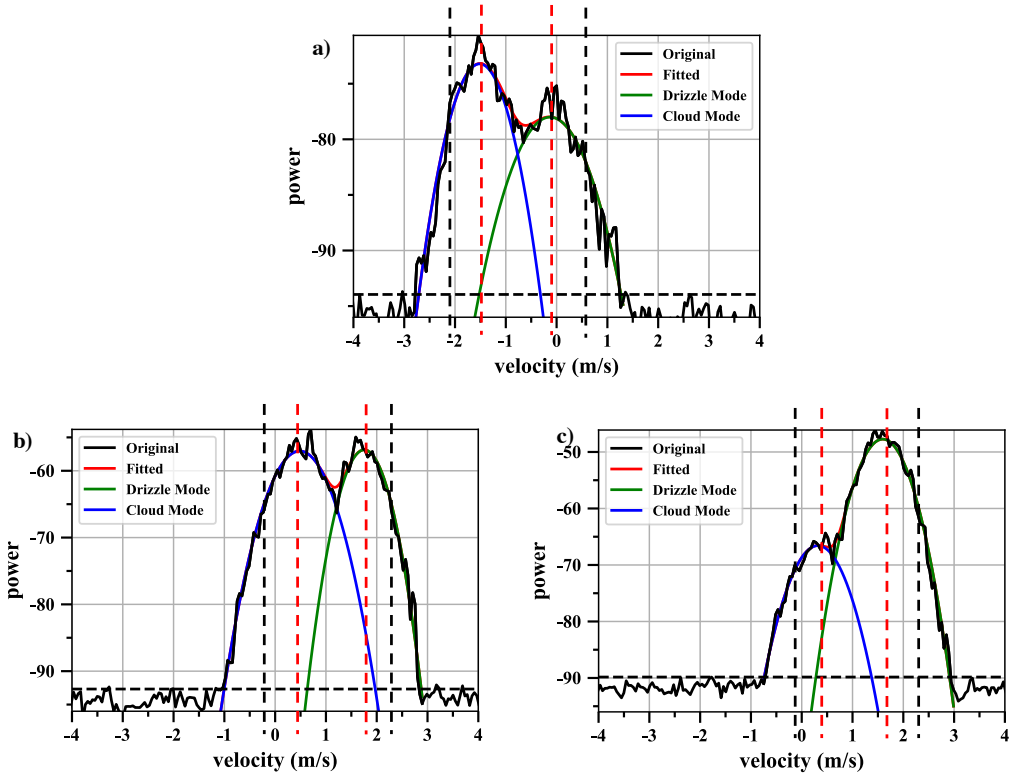


*Figure 2.3 Example of Doppler spectra decomposition for July 18, 2017 radar volume where (a) cloud mode is dominant, (b) cloud and drizzle modes are about the same, and (c) drizzle mode is dominant. In each subplot, the black line represents the original Doppler spectra measured by*

*the KAZR and the black horizontal dash line is the noise level identified using the method described in Hildebrand and Sekhon [1974]. The Doppler spectrum is decomposed into cloud mode (blue line) and drizzle mode (green line) using the algorithm detailed in the chapter and the red line is the best fitted Doppler spectrum and equal to the sum of cloud and drizzle mode. The red dash line indicates the peak associated with each mode and the distance between red and black dash line represents the spectrum width.*

Examples of $v_c$ and $v_d$, the mean Doppler velocity associated with the cloud and precipitation mode, respectively, are shown by the red dash lines in Fig 2.3, along with $\sigma_c$ and $\sigma_d$, the retrieved spectral width (distance between red and black dash lines). The reflectivity factor associated with each mode is given by the area under each Gaussian curve (if the spectra are calibrated) or can be calculated by simply dividing the total calibrated radar reflectivity factor proportionally by the area under the curve. As described earlier, since cloud droplets are small, they serve as tracers of air motion and $v_c$ is taken as the air velocity. The difference between $v_c$ and $v_d$ (the distance between the two red dash lines in Fig. 2.3), yields the mean fall velocity for the drizzle particles (which is used to obtain the PLWC as described in section 2.3.1). To be consistent with the linear fall speed regime assumption in section 2.3.1 and ensure Doppler spectra have a distinct bimodality, we consider the Doppler spectrum non-separable if the minimization yields $v_d$ - $v_c$ < 0.3 m/s.

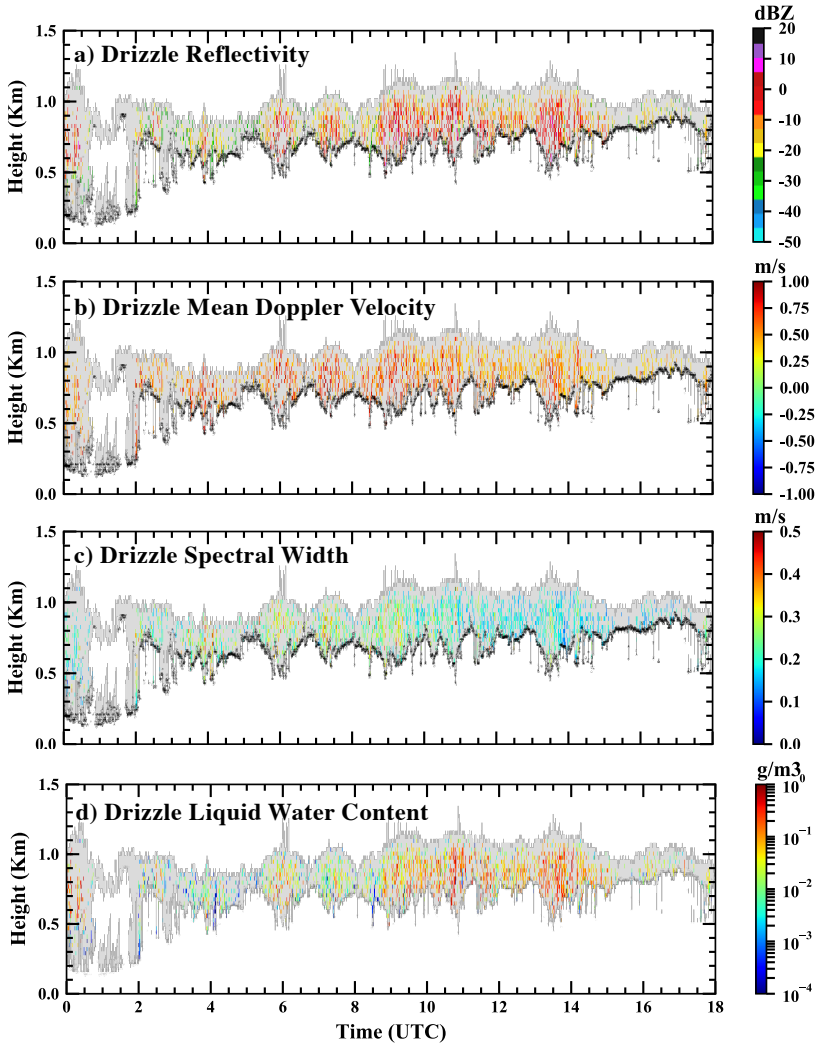


*Figure 2.4 Retrieved drizzle quantities for the same case as in Figure 2.1 using the Doppler spectra decomposition method. Shown are (a) drizzle reflectivity, (b) drizzle mean Doppler velocity, (c) drizzle spectral width and (d) drizzle liquid water content based upon the equations developed by Frisch et al. (1995). Only radar volumes where the Doppler spectra are separable are shown in color and the rest are shown in grey.*

Fig 2.4(a)-(c) shows the derived drizzle reflectivity factor, mean Doppler velocity and spectral width in the cloud for the same example shown in Fig 2.1. The corresponding PLWC is calculated based upon Eq. (2.12) and shown in Fig 2.4(d). Not all the Doppler spectra have two distinct peaks. Some spectra are totally dominated by one component and some have two peaks that are too close to separate them. Those radar volumes whose spectra do not yield separable

peaks have been left grey like radar volumes near cloud top which are totally dominated by cloud droplets. For the case on July 18, 2017, ~ 17.3% of the radar resolution volumes in the clouds were successfully separated into a distinct cloud and precipitation mode. The probability distribution function (PDF) of total reflectivity (i.e., cloud + precipitation) for the separable points and all the points in the cloud is shown in Fig 2.5(a) and Fig 2.5(b), respectively. The majority of separable points have a reflectivity value between -30 and 0 dBZ. Both PDFs peak around -10 dBZ. The lower bound shown here is forced by our requirement that the total reflectivity must be larger than -30 dBZ. We impose this restriction to ensure that there are sufficient signals above the noise floor (dashed horizontal line in Fig 2.3). Our results do not change appreciably if this threshold is lowered somewhat to -35 dBZ. We note that our results support the existence of drizzle in clouds with (total) reflectivity values below –20 dBZ [Frisch et al., 1995; Baedi et al., 2002], as also suggested by Kollias et al. [2011] who likewise find that drizzle particles exist when reflectivity is as low as -30 dBZ.

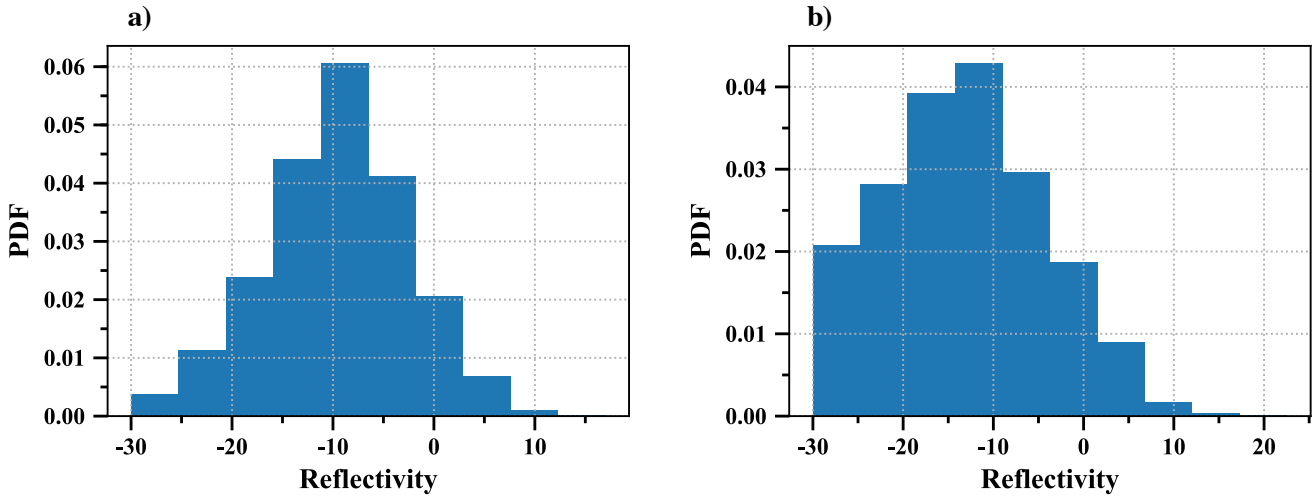


*Figure 2.5 (a) The PDF of total reflectivity where the Doppler spectra are separable, (b) The PDF of all the reflectivity in the cloud that have values larger than -30 dBZ.*

In order to calculate PLWC for those volumes whose spectra was not separable, we utilize a tuned regression method following Matrosov [1999]. Specifically, we derive a power law relationship between PLWC and total reflectivity on a case-to-case basis since aircraft observations indicate such power law relations may exist. However, one expects that drizzle water content will be larger near cloud base since drizzle particles will grow as the drizzle falls through the cloud and accretes water, while cloud liquid water will be larger higher in the cloud due to adiabatic cooling. Thus, one expects the contribution of drizzle particles to the total reflectivity will vary with altitude in the cloud, and consequently the proposed power law relation between total reflectivity and drizzle will also vary with the distance from cloud base. A 2D histogram between total reflectivity (cloud + precipitation) and corresponding PLWC for the top, middle and bottom third of the cloud are shown in Fig 2.6(a), 2.6(b) and 2.6(c), respectively, for the case on July 18, 2017. The median PLWC is calculated for every 2 dBZ of total reflectivity and denoted by the red stars in each panel, while the white dots represent the corresponding 10th and 90th percentile of PLWC in that bin. A power-law relationship between the median of PLWC and reflectivity is fitted to these data for reflectivity factors between -30 and -10 dBZ, and shown by the green line in Fig 2.6.

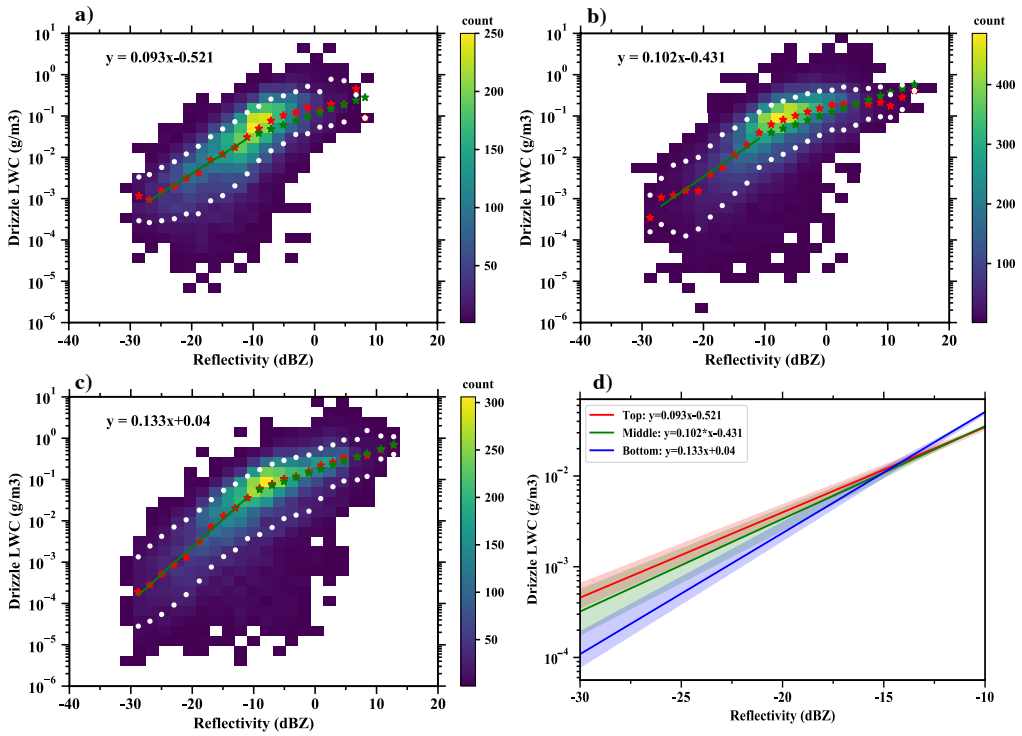


*Figure 2.6 Examples of power law relationship between precipitation (drizzle) liquid water content and reflectivity (in dBZ) for (a) top, (b) middle, (c) bottom third of the cloud on July 18, 2017. In each subplot, 2D histogram of reflectivity and PLWC in logarithmic scale is shown based upon data from Doppler spectra separable points. Reflectivity is binned into 2 dBZ interval and the median values are shown as red stars and 10th and 90th percentile are shown as white dots. The power-law is fitted for reflectivity factors smaller than -10 dBZ and is shown as a green line, with the resulting linear equation (for the log-log scale) is given in the upper left in each panel. When reflectivity is larger than -10 dBZ, PLWC is assumed to be proportional to root square of reflectivity and is shown by the green stars. The relations for the top, middle and bottom portions of the cloud are compared in panel (d) with the shading indicating the sampling uncertainty estimated using a bootstrap resampling method.*

A careful examination of the data shows a change (in slope) in the relationship between median PLWC and reflectivity (red stars) when the reflectivity is around -10 dBZ and the slope is larger when reflectivity is in the range of -30 and -10 dBZ. This is expected because as the drizzle becomes larger and more frequent, the reflectivity from drizzle particles becomes much larger

than that from the cloud particles. When reflectivity is larger than -10 dBZ, the reflectivity is heavily weighted towards drizzle as shown in Fig 2.7 which is the ratio of drizzle power to total power from the Doppler decomposition. We note that this is for those points where the cloud mode is still sufficiently large to be identified. Assuming that most of the precipitation is still small enough to Rayleigh scatter (particle size less than about 1 mm at Ka-band, which is certainly valid for drizzle), PLWC can be approximated to be proportional to the square root of reflectivity [Frisch et al., 1998]. We therefore model the relationship between PLWC and total reflectivity (Z not dBZ) above -10 dBZ as a power law with an exponent (slope) of ½. This is shown by the green stars in Fig 2.6, which demonstrates this approximation compares well to median values (red stars).

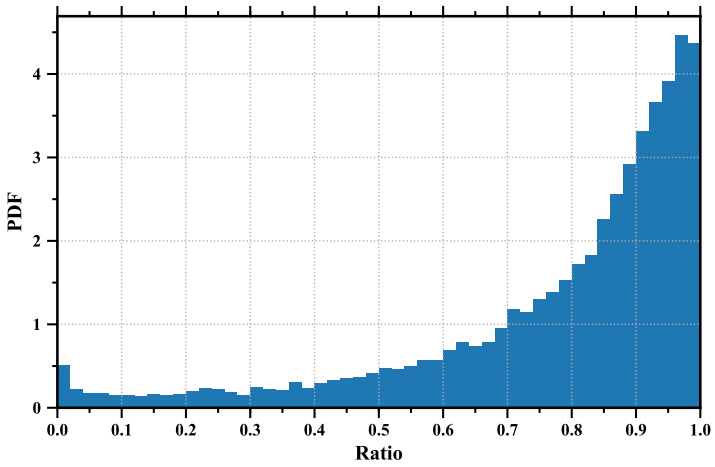


*Figure 2.7 Distribution of the ratio of the drizzle mode power to the total power (Z_drizzle / Z) based on the Doppler spectra that are separable and have a reflectivity larger than -10 dBZ on July 18, 2017.*

The resulting power-law relationships between PLWC and total reflectivity for the top, middle and bottom third of the cloud are shown by the solid lines in Fig 2.6(d), while the shading shows the uncertainty due to sampling, estimated using a bootstrap method [Marchand et al., 2006;

Zhao et al., 2017]. Specifically, the retrieved PLWC in each 2 dBZ interval is randomly resampled with replacement many times and the shadings show the 5% (upper limit) and 95% (lower limit) of the median values that are obtained from the resamples. From Fig 2.6(d), one sees the relationship between PLWC and total reflectivity does depend on vertical position within the cloud, and not surprisingly, the impact is largest when the reflectivity is small. For a given total reflectivity, generally there is more PLWC in the top of the clouds and less in the bottom. This does not mean there is more PLWC at the top of the cloud, and we stress this for a given value of total reflectivity. To understand this, we investigate the modal radius ($r_0$) and the total number concentration (N) for drizzle droplets calculated via Eqs. (2.10) and (2.11). The vertical profiles of their median values are illustrated in Fig 2.8 for our case study. It shows that $r_0$ decreases and N increases from cloud base to the top. These vertical signatures are expected as relatively small drizzle droplets are formed through the collision and coalescence of cloud droplets (which will be largest where the CLWC is largest, near cloud top) after which the precipitation particle size will rapidly grow larger through collisions with both cloud and other precipitation particles, as the precipitation falls through the clouds towards the bottom. Thus collision-coalescence increases the size and decreases the number of precipitating particles going from cloud top to cloud bottom. Since reflectivity is proportional to the six power of particle size, there is larger PLWC near the top for a given total reflectivity.

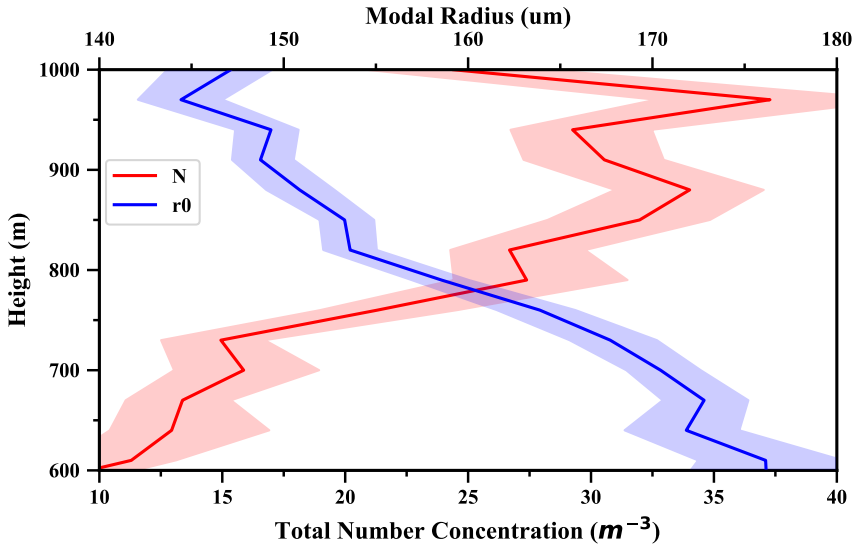


*Figure 2.8 Vertical distribution of total number concentration (red line) and modal radius (blue line) of drizzle particles in the cloud using the separable points on July 18, 2017. The shadings indicate the sampling uncertainty.*

### 2.3.3 ***Retrieval of below-cloud PLWC***

As there are obviously no cloud particles below cloud base, the spectra decomposition method cannot be used to determine the drizzle fall velocity. Instead, retrievals of below-cloud precipitation based on the Frisch et al. [1995] approach have sometimes be applied a technique proposed by [Orr and Kropfli, 1999] who argued that air velocity will be close to zero after averaging over a sufficient amount of time in a stratiform cloud system, and the average measured Doppler velocity will be approximately equal to mean drizzle fall velocity. And consequently, if one assumes that a given value of reflectivity (at a given altitude) has a characteristic drop size distribution, one can find the average fall velocity for that distribution by averaging the measured Doppler velocity as a function of reflectivity. Here, we partition the measured radar reflectivities into 2 dBZ bins ranging from -30 to 10 dBZ, just as was done in the

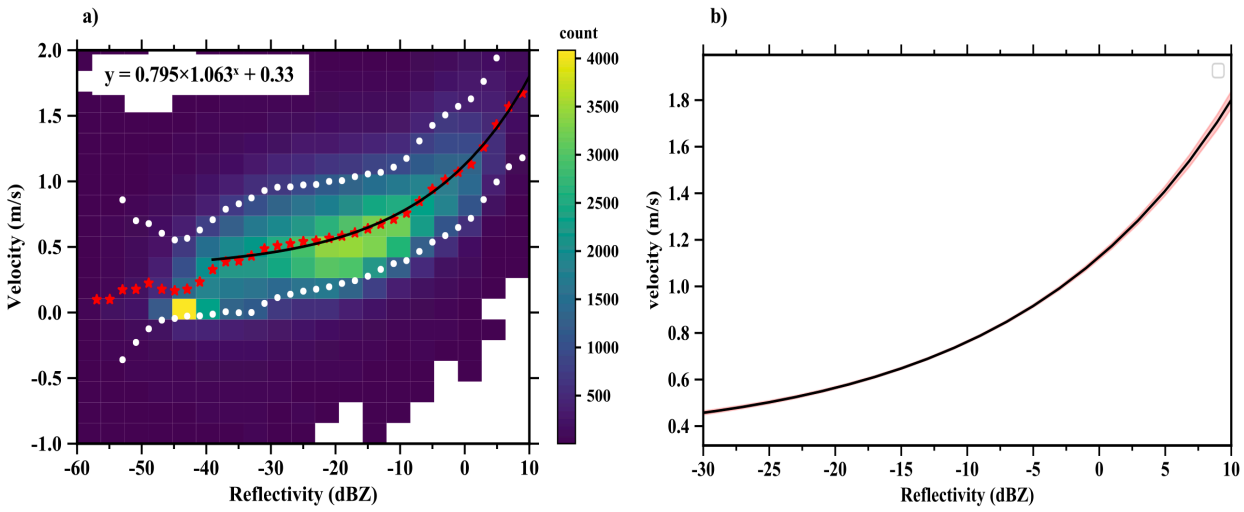


*Figure 2.9 (a) Distribution of observed radar Doppler velocity below cloud-base as a function of radar reflectivity observed on July 18, 2017. Reflectivity is binned into 2 dBZ interval and the mean Doppler velocity is given by the red stars, with the 10th and 90th percentile shown as white dots. The power-law fit to the mean Doppler velocity is shown as the black line with the mathematic formula given in the upper left (the unit of reflectivity is dBZ). The sampling uncertainty of the power-law coefficients is estimated using a bootstrap method and shown in (b) as the shading.*

previous section. In Fig 2.9, we show the corresponding distribution of measured Doppler velocities, with the red stars denoting the average measured Doppler velocity in each reflectivity bin. A power law relation is then fit to obtain the average Doppler velocity as a function of reflectivity (the equation is shown in the upper left of Fig 2.9(a)). The sampling uncertainties of the estimated fall velocity are assessed using the bootstrap method which are small. We note that we have used all below cloud-base values here, and in application one might expect the drop size distribution to change with evaporation and nominally one might therefore apply this approach over a relatively narrow range of altitudes. The Frisch equations for PLWC also require knowledge of the logarithmic width, $\sigma_x$, in addition to the mean drizzle fall velocity. Following Frisch et al. [1995], a simple approach would be to set such to a fixed or constant

value (though if the full Doppler spectra available one might estimate such from the spectra, as long as one carefully accounts for signal to noise ratio). Frisch et al. suggested a width of 0.35, which appears to be typical for Sc drizzle. For the case of July 18, 2017, the retrieved values from the separable spectra in cloud ranged from 0.1 and 0.7 with a mean value of 0.33 (Fig 2.10). Wu et al. [2018] found a value 0.38 based upon aircraft observations over the ENA site. The impact of using 0.33 versus 0.38 in the retrieval is small compared with other factors, including the systematic errors associated with the estimated fall velocity, which will also be discussed later in the chapter. The retrieved PLWC (including both in and below cloud) are shown in Fig 2.11(a). Here the tuned-regression for top, middle, and lower third of the cloud, as appropriate, have been used to obtain the PLWC for radar volumes whose spectra were not separable. As expected, large PLWC values occur when reflectivity is large. It also illustrates that PLWC increases from the cloud top to the bottom and decreases as drizzle particles fall out of the cloud due to evaporation.

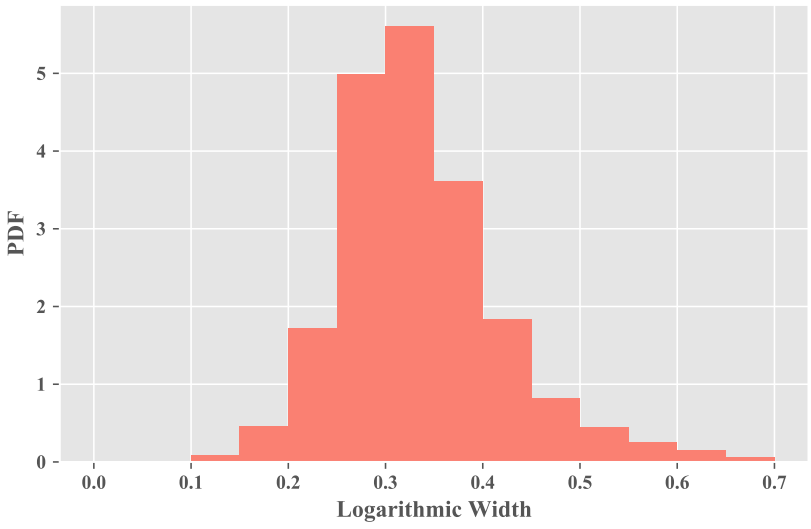


*Figure 2.10 The PDF of the logarithmic width of drizzle droplet number distribution obtained from the separable spectra in cloud on July 18, 2017.*

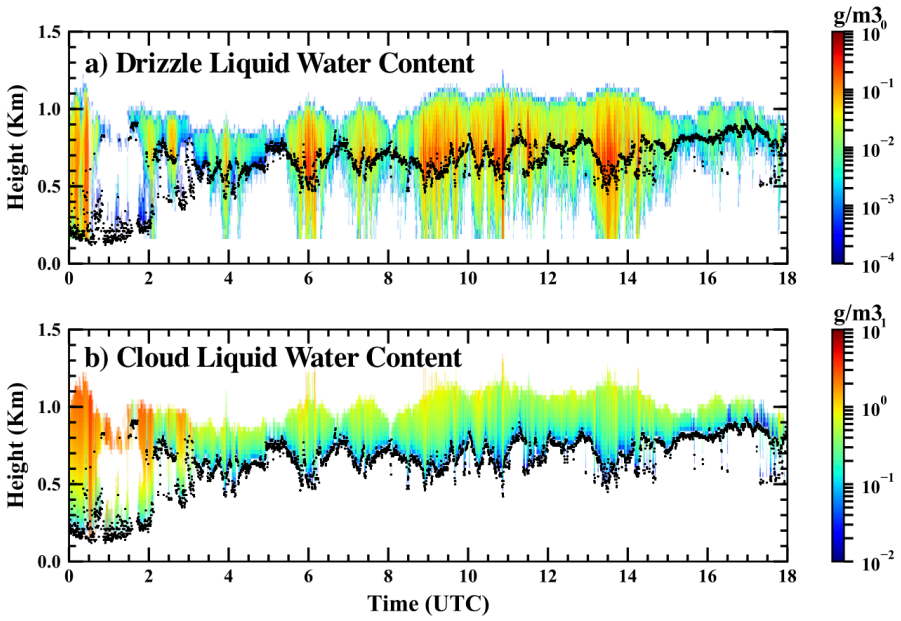


*Figure 2.11 (a) Retrieved precipitation (drizzle) liquid water content. (b) Retrieved cloud liquid water content for the same case as in Figure. 2.1 on July 18, 2017.*

### 2.3.4 ***Retrieval of CLWC***

For an adiabatic liquid water cloud [Albrecht et al., 1985; Grosvenor et al., 2018], CLWC increases linearly with height in cloud and can be generally expressed as follows:

$$\mathrm{CLWC(z)} = f_a c_w z \tag{2.13}$$

where $f_a$ is called the adiabatic factor and equal to 1 for a fully adiabatic cloud, $c_w$ is the condensation rate with height for air parcels that rise moist adiabatically, and z is the height above the cloud base. $c_w$ is calculated as:

$$c_w = \rho_a \frac{c_p}{L_v}(\Gamma_m - \Gamma_d) \tag{2.14}$$

where $\rho_a$ is the air density, $c_p$ is the specific heat of dry air at constant pressure, $L_v$ is the latent heat of evaporation for water, $\Gamma_m$ and $\Gamma_d$ are the moist and dry adiabatic lapse rates, respectively.

$\Gamma_m$ is a weak function of pressure and temperature and the value at the cloud top is used in Eq. (2.14) to calculate $c_w$ based on radiosonde observations following Grosvenor et al. [2018].

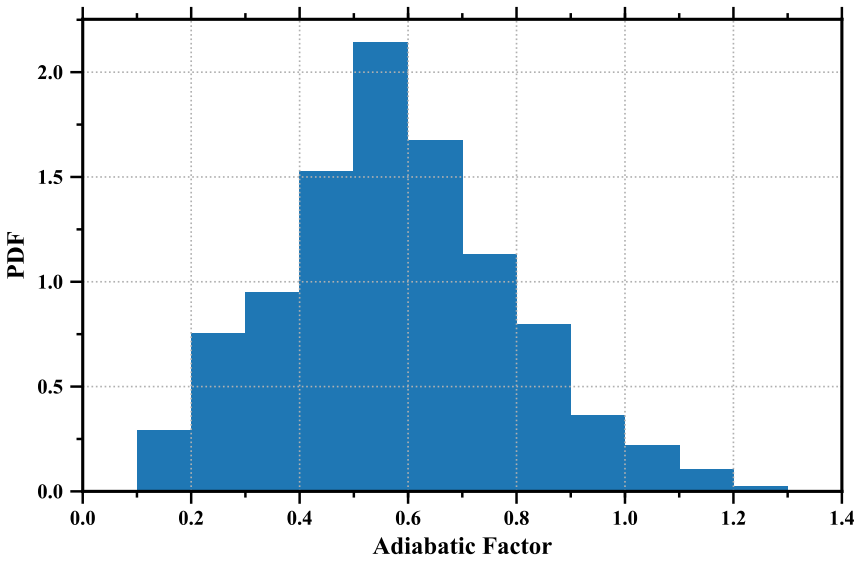


*Figure 2.12 The PDF of the adiabatic factor defined as the ratio of liquid water path (LWP) measured by MWR over LWP derived assuming that an air parcel rises moist adiabatically in the cloud on July 18, 2017.*

In situ aircraft observations of Sc indicate that the assumption of a constant cloud droplet number concentration vertically is often valid but CLWC profiles can depart from adiabatic profiles substantially due to entrainment of dry air and liquid water removal by precipitation [Albrecht et al., 1985; Boers et al., 2000; Chin et al., 2000; Painemal and Zuidema, 2011; Min et al., 2012]. The subadiabaticity of clouds are taken into account by $f_a$ in Eq. (2.13), which is found to vary in the range of 0.1 to 0.9 based on the aforementioned aircraft studies. In this study, when TLWP from MWR is available and valid, we subtract PLWP, the liquid water path due to precipitation, from the MWR TLWP to obtain the CLWP and then CLWC is calculated assuming a linear increase from cloud base to top. Note that PLWP is the integration of in-cloud and below-cloud PLWC with height retrieved using methods described in section 2.3.2 and 2.3.3.

The corresponding $f_a$ is also obtained by dividing actual CLWP by the adiabatic CLWP. The distribution of $f_a$ for the July 18, 2017 case is shown in Fig 2.12. The majority of $f_a$ values are between 0.2 and 0.9 with mean and median value of 0.58 and 0.57, respectively, which are similar to results from previous studies. $f_a$ is occasionally larger than 1, which is likely due to uncertainties of the measurements associated with MWR TLWP, cloud boundaries from the radar or the radiosonde temperature profiles [Merk et al., 2016].

When drizzle reaches the ground and the MWR is wet, the MWR retrieved TLWP will be artificially large and these bad data need to be discarded. For those times, Eq. (2.13) is used to calculate CLWC with $f_a$ taken as the median value over a time-window which we increase in size stepping from 10, 20, 60, 120 or 1440 minutes as needed with a criteria that at least 30% of the radar columns in the time-window must have a valid MWR CLWP and estimated value for $f_a$. On a few cases, if there were not enough valid $f_a$ retrievals for the whole day (1440 minutes), and a climatological value of 0.66 was used following Merk et al. [2016]. The retrieved CLWC is illustrated in the lower panel of Fig 2.11. In general, thicker clouds have larger CLWP and larger values of CLWC in the upper portions of clouds than thinner clouds, as one expects. Uncertainties in the retrieved CLWC will be discussed in section 2.5.

## 2.4 Case Studies

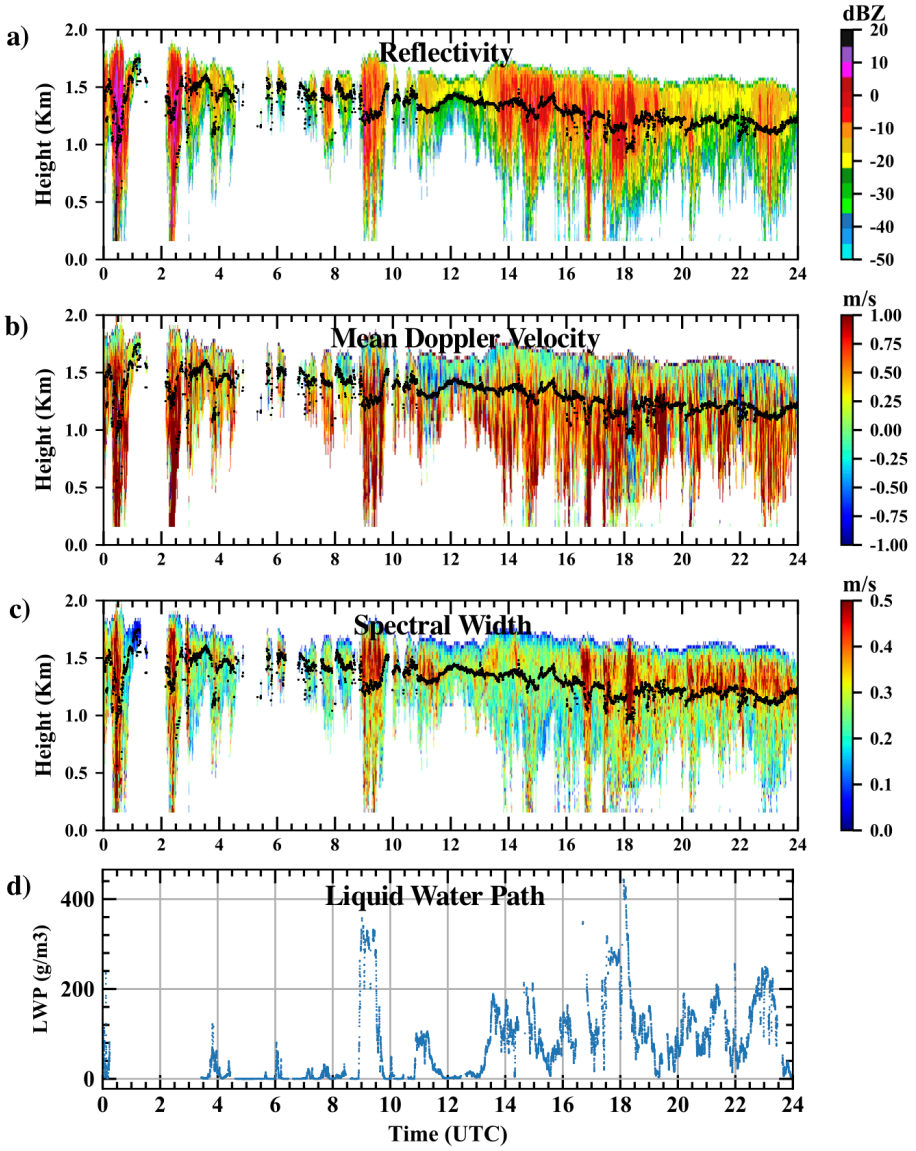


*Figure 2.13 Same as Figure 2.1 but for the case in January 15, 2018.*

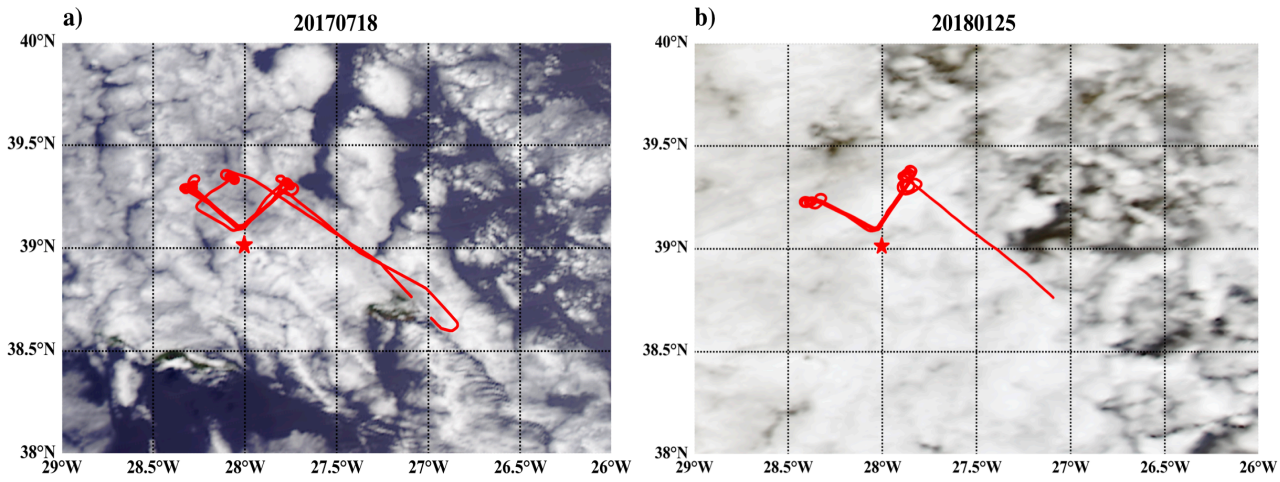


*Figure 2.14 Satellite images of the clouds over ENA site (red star) for the cases of July 18, 2017 and January 25, 2018. The red line represents the path of the aircraft.*

In this section we compare retrieved PLWC and CLWC to in situ aircraft measurements collected during the ACE-ENA field campaign. Specifically, we examine data from flights undertaken on July 18, 2017 (8.5 - 12 UTC) and January 25, 2018 (11 - 12 UTC). These flights sampled a large region of stratocumulus which encompassed the ARM ENA site. The reflectivity, mean Doppler velocity, spectral width and LWP for the July 18 flight are shown in Fig 2.1 and that for the January 25 flights are shown in Fig 2.13, along with satellite images overlaid with the longitude and latitude of the aircraft during flights in Fig 2.14. Since aircraft observations sampled spatially around the ENA site whereas the radar operates temporally, only statistical comparisons are made, which are shown in Fig 2.15 and Fig 2.16 for the July 18 and January 25 cases, respectively.

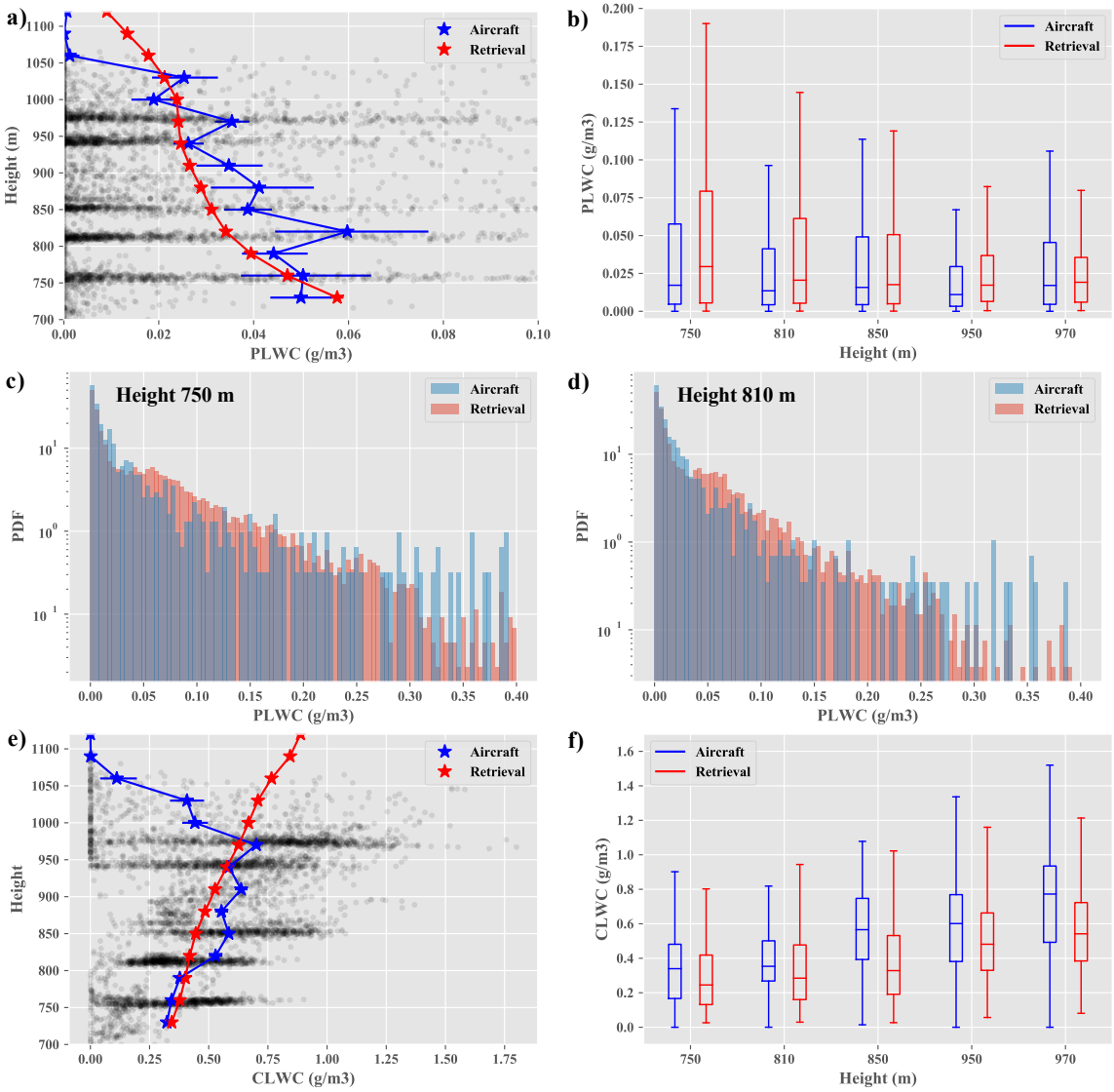


*Figure 2.15 (a) comparisons between retrieved PLWC and aircraft observations for the case of July 18, 2017. The black dots represent aircraft observations. The means of aircraft observations (blue stars) and retrieved values (red stars) at given levels are showed. (b) same as (a) but with the box and whisker plots at five levels. (c) and (d) PDF of aircraft observations and PLWC retrieval at 750 m and 810 m, respectively. (e) and (f) Same as (a) and (b) but for CLWC.*

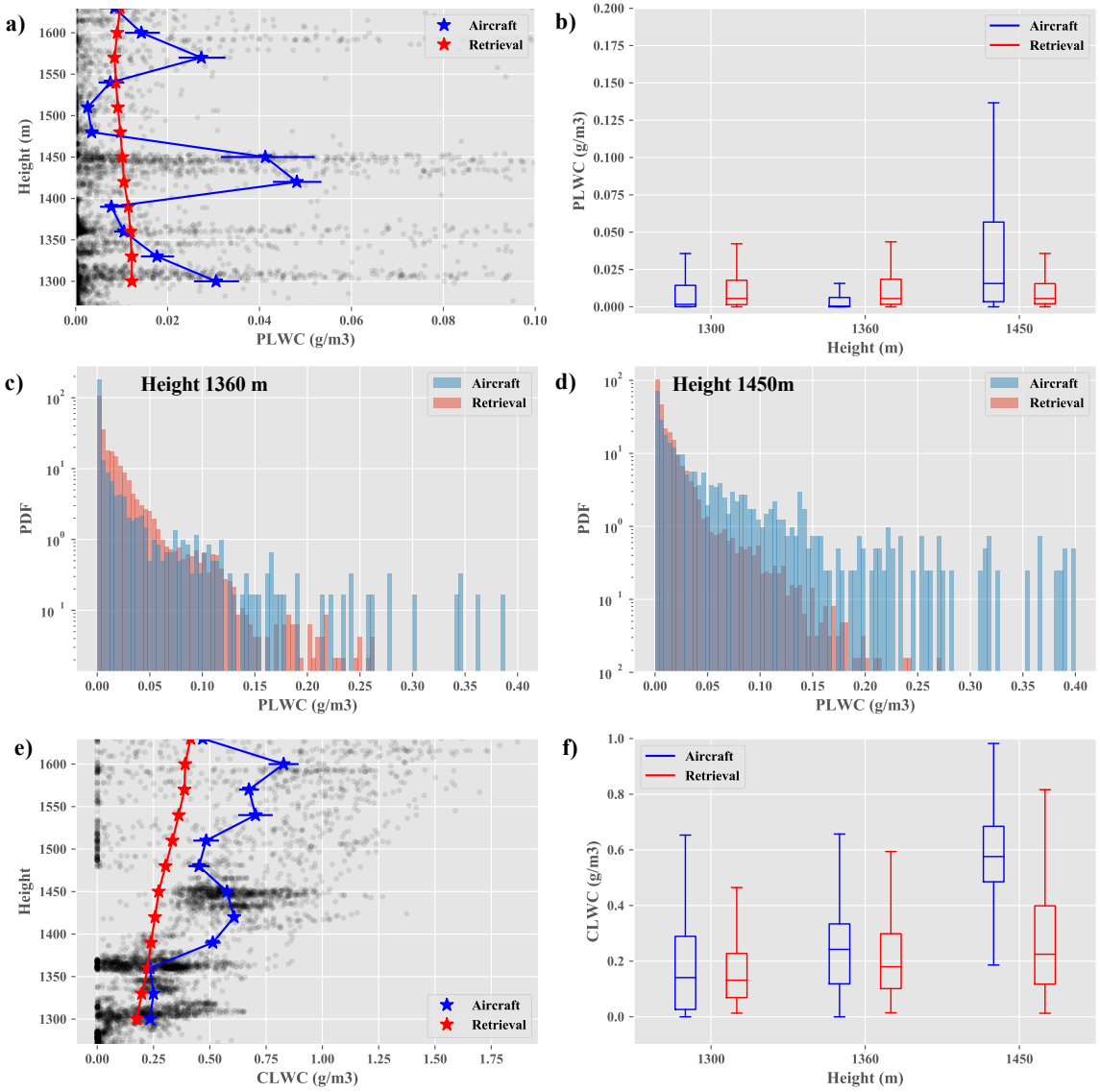


*Figure 2.16 Same as Fig. 2.15 but for the case of January 25, 2018.*

Observed PLWC at different altitudes above mean sea level is illustrated as the black dots in the top left panels (Fig 2.15(a), Fig 2.16(a)) and the corresponding CLWC is shown in the bottom left panels (Fig2.15(e), Fig 2.16(e)). At any given altitude, the observed PLWC and CLWC has a very large spread. The average of observations and retrievals at each altitude is denoted by blue and red stars, respectively, and the horizontal bars indicate the sampling uncertainty in the means (showing the 5th and 95th confidence limits estimated using a bootstrap method). The

sampling uncertainty in the average for the retrievals is small and is generally smaller than the red-stars symbols used to denote the average value. Note that outliers in the PLWC can substantially bias the mean so PLWC values that 3 times standard deviation larger than the mean at a given level are removed for both observations and retrievals. In the July 18 case both the averaged retrieved values of PLWC (Fig 2.15(a)) and CLWC (Fig 2.15(e)) compare well with aircraft observations, at least between 700 m (around cloud base) to 1000 m (near cloud top). The difference in the mean PLWC is generally within or near the sampling uncertainty of aircraft observations. The CLWC, on the other hand is biased slightly low over most of the cloud layer, but above 1000 m the observations seem suggest a decrease in CLWC. Such a decrease might be expected due to cloud-top entrainment. However, as indicted by the density of black dots, we note that the aircraft spent very little time between 1000 m and 1100 m and was flying in and out of clouds at this altitude such that this apparent decrease in CLWC is likely due in part to measurements taking during intervals when the aircraft was only partially in cloud, and not due only to entrainment. Nonetheless, it is worth stressing that the retrieval technique we have employed forces a linear profile and will not be capture any reduction in CLWC at or near cloud-top due to entrainment.

In Fig 2.15(b) and 2.15(f), box and whisker plots of PLWC and CLWC are shown at five levels where the aircraft flew extended level-legs and the majority of the airborne samples are located. Fig 2.15(b) indicates that there is considerable overlap in the interquartile range (IQR or boxes). The retrieval and observation IQR are about the same at 850 m and observation seems wider at 970 m. At the level of 750 m, 810 m and 950 m, retrievals have a larger IQR. We explore the PLWC distributions in more detail in Fig 2.15(c) and 2.15(d), which show the probability density function (PDF) of PLWC near 750 and 810 m, respectively. Although the distribution of

retrieved PLWC is similar to the aircraft observations, the retrieval contains more PLWC values in the range of 0.05 and 0.15 g/m$^3$ which can also be seen in other levels. It may also be that the occurrence of large PLWC values greater than 0.3 g/m$^3$ is too small in the retrieval. There are obvious very few aircraft samples at these larger values but it is hard to compare the values in the tail of the distribution. For CLWC as shown in Fig 2.15(f), the IRQ are comparable but the median, 25th and 75th of the retrievals are smaller than observations.

Fig 2.16 is the same as Fig 2.15 but for the January 25 case. It shows that averaged retrievals of PLWC and CLWC are close to aircraft observations in the lower portion of the cloud between 1300 m and 1370 m (Fig 2.16(a), Fig 2.16(e)). In this lower part of the cloud, the interquartile range (Fig 2.16(b), Fig 2.16(f)) is slightly larger for retrieved PLWC and smaller for retrieved CLWC as compared to the observation, similar to the earlier July 18 case. Fig 2.16(c) shows the PDF of retrieved and observed PLWC at around 1360 m. The aircraft observations have many small PLWC values (<=0.004/m$^3$) and few values beyond 0.15 g/m$^3$ as compared with retrievals. Higher in the clouds, at an altitude near 1450 m, the retrieved PLWC and CLWC have a noticeably smaller mean, median and narrower distribution (at least for PLWC) than the aircraft observations, which is also evident in the PDF of PLWC (Fig 2.16(d)). The exact reason for this substantial discrepancy is not clear but for this case, there was considerable cumulus clouds below the Sc around for example 0, 2, 9 and 18 UTC, so the aircraft might have hit a cumulus core at 1450 m which is much different from the clouds observed by the ground-based radar.

Overall, the characteristics of clouds on July 18 and January 25 are quite dissimilar. For instance, in the July 18 case, the cloud base is much lower and occurrence of negative mean Doppler velocities (upward motion) is much larger than in the January 25 case (Fig 2.1 and Fig 2.13). More importantly, observed PLWC and CLWC is generally larger on July 18 as indicated

by both the aircraft observations and radar retrievals. In Fig 2.17, we compare the tuned regressions from these two cases for the top, middle and bottom of the cloud. This result strongly supports the idea that a universal power law equation between PLWC and reflectivity does not exist (or perhaps we should write that as an approximation it is only going to be good to an order of magnitude even for an event – taken here to be a 24 hour period).

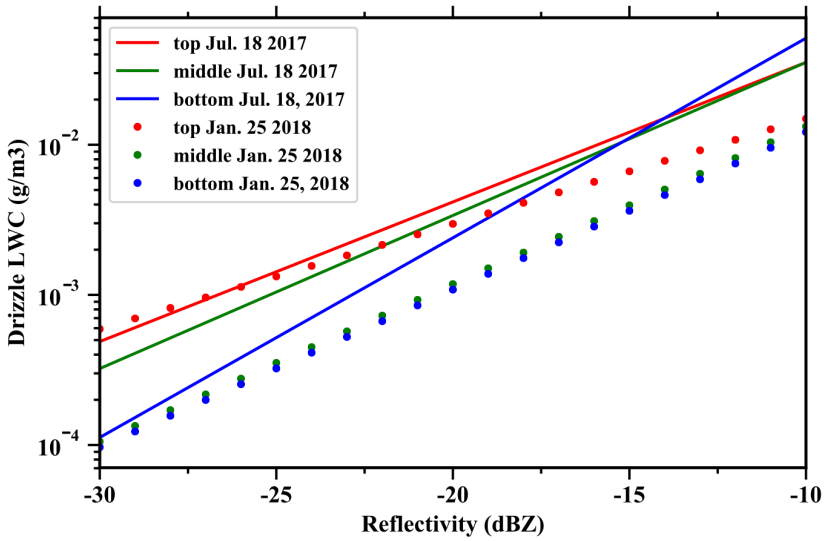


*Figure 2.17 Comparison of the relation between PLWC and total reflectivity for the case of July 18, 2017 (solid line) and January 25, 2018 (dash line) in the top (red), middle (green) and bottom (blue) of the cloud.*

## 2.5 Uncertainty

In this section, uncertainties in the retrieved PLWC and CLWC are discussed. For purposes of this discussion we divide the uncertainties into random errors, which can be largely reduced by averaging (that is, looking at retrieved quantities on larger temporal and spatial scales) and systematic errors, which cannot generally be reduced by averaging. The retrieval framework contains many assumptions that result in both random and systematic errors.

Perhaps the most important assumption for the retrieval of in-cloud PLWC is that there exists a power law relation between PLWC and reflectivity and this relation, derived from the separable points, is applicable to all other points in the cloud. At the scale of a single radar volume, this is certainly the dominant source of uncertainty in the PLWC, meaning the likely difference between the true value for PLWC and the retrieved value. The white dots in Fig 2.6 (a, b and c) show that the variability at the scale of a single radar volume is about an order of magnitude. The power-law is tuned to provide the median PLWC, and when the PLWC is averaged to larger scales, the uncertainty, that is the potential random error, will be much lower. We used a bootstrap resampling technique to estimate the systematic errors in the median, as illustrated by the shadings in Fig 2.6(d). Taking as an example the bottom of the cloud (blue line and shading in Fig 2.6(d)), when reflectivity is -30 dBZ, the median retrieved PLWC is $1.1 \times 10^{-4}$ g/m3 with a 95% confidence interval of $7.8 \times 10^{-5}$ and $1.9 \times 10^{-4}$ or about -30% to +70%. At larger values of reflectivity the potential systematic error is lower. At a reflectivity of -10 dBZ, the retrieved PLWC is 0.05 g/m3 and the 95% uncertainty is within +/- 10%.

As shown in Fig 2.8 and discussed earlier, the particle size distribution shifts towards larger sizes from the cloud top to the bottom, and consequently, we applied different tuned-regressions to the top, middle and bottom layers of the cloud. Of course, other formulations, for example based on absolute distance from cloud base or based on cloud-thickness, are possible, and there is a potential for systematic errors in the vertical profile of PLWC. Fig 2.6(d) illustrates that at the small values of total reflectivity (-30 dBZ), the difference in the tuned regression between the top and bottom of the cloud can be as high as a factor of 4. This indicates that by fitting relations separately for the top, middle and bottom of the cloud, the systematic errors can be largely reduced.

Ultimately, we rely on the comparisons with the aircraft data to try and gauge the overall uncertainty. This is obviously less than ideal as we have only data from two flights and the aircraft data have many of their own sources of uncertainty, and are not sampling the same cloud at the same time. Nonetheless, for the case of July 18, the difference between the retrieval and observational mean PLWC ranges from 7% to 75% over the altitudes which were well sampled by the aircraft. The same is true for the January 25 case in the lower part of the cloud, while as discussed in the previous section, difference in the upper part of the cloud are likely due to sampling different portions of the cloud. Overall we adopt an estimate of 75% for the systematic uncertainty for the in cloud PLWC, as this is consistent with the aircraft data and preceding discussion of various sources of systematic error.

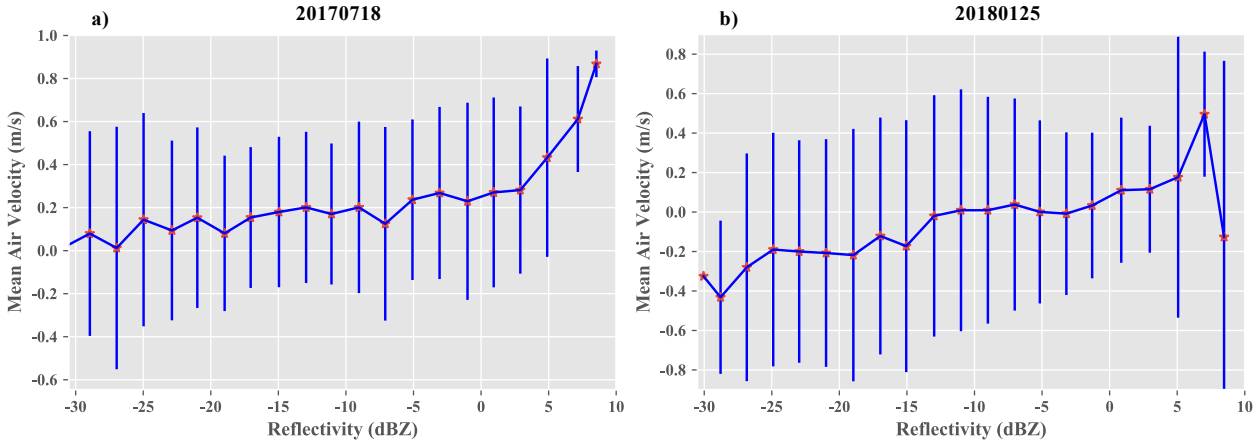


*Figure 2.18 Mean air velocity in each drizzle reflectivity interval obtained from the separable points near cloud base for the case of (a) July 18, 2017 and (b) January 25, 2018. The red stars indicate the mean and the vertical lines represent one standard deviation. Positive values indicate downward motion.*

For the retrieval of PLWC below cloud, following Orr and Kopfli [1999], we assumed there is a characteristic DSD associated for a given value of radar reflectivity, and that the difference between true fall velocity and the averaged Doppler velocity are largely due to random errors

which can rendered negligible by averaging the Doppler velocity. The sampling uncertainty in the estimated mean Doppler velocity after averaging is illustrated in Fig 2.9(b), and is very small. However, the assumption the Doppler velocity can be averaged to yield the fall velocity (that in effect, updraft-and-downdrafts balance out independent of radar reflectivity) does not appear to be true and may result in a significant systematic error. Fig 2.18 shows the averaged air velocity (at as function of the drizzle reflectivity) using the air velocity retrieved by the Doppler spectra decomposition method near cloud base. The positive values indicate downward motion. For the July 18 case, the averaged air velocity varies increases between 0 and 0.4 m/s as reflectivity increase from -30 to 5 dBZ (with larger values above 5 dBZ though there are few samples here), while for the January 25 case, the apparent air velocity increases from -0.2 m/s to 0.2 m/s. In general, one expects that the boundary layers as a whole may increases or decrease in depth such that there may be a net upward or downward motion in the atmosphere. However, typically we expect this large-scale ascent or descent to be small, only a few centimeters per second. In addition to the potential for systematic error due to the large-scale motions, the results in Fig. 2.18 demonstrate there is not a uniform or constant motion, but that larger values of reflectivity (and larger values of PLWC) are associated with net downward air motions, at least at cloud base. In principal one might use this mean retrieved air-velocity at cloud base rather than assuming there is no net air motion. However, the mean air velocity in the subcloud layer may differ from that near cloud base. A better solution might be to use vertical air motions derived from Doppler lidar (or other sources), and for the ENA site, since calibrated lidar data is collected by the ARM program it may well be better to rely on a radar-lidar retrieval below cloud base (see for example O'Connor et al [2005]). The below cloud PLWP (which is subtracted for the TLWP to obtain the CLWP) is much smaller than the CLWP, and as such the below cloud

PLWC is not a significant factor in our analysis of autoconversion and accretion (Chapter 3). And for the present we simply note that our below-cloud PLWC may contain systematic (case-by-case) errors due to air velocity.

Our retrieval of CLWC depends on four factors: (i) the assumption that CLWC in Sc increases linearly from cloud bottom to cloud top, (ii) determination of cloud-base and cloud-top (from radar and ceilometer/lidar), (iii) accurate determination of TLWP from microwave radiometer and (iv) accurate $f_a$ used. While aircraft studies generally support Sc having a linear (adiabatic-like) vertical profile of CLWC on average, it is difficult to assess how much random or systematic errors this assumption likely generates. Individual aircraft ramp-penetrations through Sc do not necessarily represent the true level of vertical variability, but nonetheless such data suggests that large instantaneous (random) order-of-magnitude deviations from a linear profile should be expected. Flight mean (systematic) differences will certainly be much smaller, though as discussed earlier vertical variations in the mean profile (due for example to cloud-top-entrainment or heavier rates of collision-coalescence in the lower portion of clouds) will not be captured in the retrieval. In comparison to the aircraft observations examined in the previous subsection, the difference between our retrieved estimated and observed mean CLWC profiles ranged from 5% to 30%, in the middle and lower portions of the cloud where entrainment is not a concern. The cloud-base and cloud-top height determined by the radar and ceilometer/lidar may also have biases. The ceilometer and lidar are generally accurate in determining the cloud base, however, when precipitation is very intense and the number concentration of precipitation particles is large enough, signals of the ceilometer and lidar will be attenuated and thus the cloud base is mistakenly biased lower [Clothiaux et al., 2000]. Since most of precipitation in ENA is drizzle, the bias is expected to be small. Uncertainty in MWR TLWP itself ranges from about

10% for TLWP of 200 g/m$^2$ to 60% for TLWP of 50 g/m$^2$ [Cadeddu et al., 2013], which can be systematic (affecting all attitudes). When TLWP is not available, the median value of $f_a$ in a time window is used. Previous studies have found that $f_a$ tends to decrease with cloud depth and rain rate [Wood, 2005; Merk et al., 2016; Braun et al., 2018] which is not considered here and will likely introduce some errors. Meanwhile, when not enough $f_a$ exists, a fixed value for $f_a$ is used which could likewise introduce a systematic error of roughly +/-50% (assuming a fixed value near 0.6 and the true value ranges from 0.3 to 0.9).

## 2.6 Summary

Due to their persistence and vast coverage, accurate ground-based retrievals of PLWC and CLWC are needed for marine Sc. In this chapter, a combination of techniques has been utilized to retrieve PLWC and CLWC using primarily radar Doppler spectra and microwave radiometer measurements collected at the ENA site (located in the Azores) by the DOE ARM program. To the degree these data can be used to estimate (retrieve) the microphysics of Sc (and other clouds), the (nearly) continuous data record being produced the ARM program these data offer researchers the opportunity to better understand microphysical processes, test models and develop new parameterization schemes. In particular, the goal of the present work was to obtain simultaneous retrievals of CLWC and in-cloud PLWC in order to evaluate the impact of spatial variability in these properties on model autocorrelation and accretions rates (which is undertaken in Chapter 3).

In order to obtain in-cloud PLWC, we used equations derived by Frisch et al. (1995) to retrieve the parameters of a log-normal precipitation distribution (from radar reflectivity, mean Doppler velocity, and Doppler spectral width) in combination with a Doppler spectra decomposition

method. The main idea of the method is to separate the Doppler spectra collected by the ARM Ka-band Zenith pointing cloud Radar (KAZR) into cloud and drizzle components, thereby allowing the reflectivity, velocity and spectral width associated with each component to be derived. Since cloud particles are small and have a negligible terminal velocity, they serve as tracers of air velocity and thus precipitation fall velocity (required by the Frisch formulation) can be retrieved and used to determine the PLWC, precipitation particle size and distribution width. However, less than 20% of the radar volumes observed in Sc are typically found to have a separable Doppler spectra, and so we use power law equations, essentially a tuned case-by-case regressions, to estimate (retrieve) the precipitation microphysics for radar volumes whose spectra are not separable. In our application, individual power-law relationships are derived for the upper, middle and bottom portions of a cloud layer to account for changes underlying precipitation drop size distributions (such as changes in the mean profile of effective radius). The retrieved PLWC is found to be sensitive to this vertical dependence especially when the total reflectivity is small. In general, we find the power-law relationships between in cloud PLWC and reflectivity vary both vertically and on a case by case basis, and there is no universal relation between PLWC and reflectivity.

Following previous works, we derived PLWC below-cloud by assuming that air velocity due to updrafts and downdrafts will average to zero (on the scale of a day). However, a comparison of our two retrieval techniques at cloud base (the boundary between two regions) suggest that this assumption is not generally valid. We do not require an accurate below-cloud PLWC for our later analysis (chapter 3) and so leave further investigation of this topic for later study.

CLWC is calculated assuming it linearly increasing in altitude (starting from zero at cloud base). When retrievals of TLWP from the MWR are used when they are available (meaning when the

MWR is not wet), otherwise, an adiabatic cloud model is used but the condensation rate adjusted by an empirical adiabatic factor (based when possible on data collected from the MWR).

Random and systematic errors with all of the above retrievals are discussed in detail in section 2.5. Overall random errors (on the scale of a single radar volume) are expected to be order-of-magnitude while systematic errors (which remain after averaging the cloud properties over a full day) are estimated to be around 75% for in-cloud PLWC based on a combination of comparison with aircraft observations and some sensitivity tests. The situation is similar for CLWC, with the additional important caveat that vertical variations in mean properties are not characterized.

# Chapter 3.

# A Cloud Radar Analysis of Enhancement Factors for Autoconversion and Accretion Rates

## 3.0 Overview

In models applying bulk microphysical schemes, including perhaps all climate models, precipitation in warm clouds is generated through autoconversion and accretion processes, and the associated (grid-mean) process rates must be calculated from the grid-mean cloud and precipitation liquid water mixing ratio predicted by the models. Typically, the effect of subgrid variability is incorporated by multiplying the process rates calculated assuming no variability, by an enhancement factor which is derived by integrating the process rates over an assumed spatial distribution for the mixing ratios. In this study, enhancement factors for autoconversion and accretion rates (i.e. $E_{auto}$ and $E_{accr}$) in stratocumulus are evaluated utilizing radar retrievals at the ARM Eastern North Atlantic site. Based on our retrievals for marine Sc (Chapter 2) and consistent with previous studies on enhancement factors, we find that enhancement factors are sensitive to the model grid-scale, and they reach their maximum when precipitation fraction is between 0.4 to 0.6, depending on the grid size and the threshold used for defining precipitation. We also find that $E_{auto}$ stays relatively unchanged vertically but $E_{accr}$ generally decreases from cloud base to cloud top. Meanwhile, the enhancement factors from event to event have little if any correlation with surface relative humidity, lower tropospheric stability, liquid water path (LWP) or cloud thickness. However, they are highly correlated with the subgrid variability in

LWP, cloud thickness and cloud base height suggesting almost any knowledge of subgrid variability could be useful in further constraining the enhancement factors.

## 3.1 Introduction

Marine stratocumulus clouds (Sc) are a vital component in the climate system due to their extensive and persistent occurrence [Hahn and Warren 2007; Wood 2012] and strong radiative cooling impact [Hartmann et al., 1992]. Many different physical processes, such as radiative cooling, turbulence, and entrainment, as well as cloud-aerosol-precipitation microphysical interactions are important in maintaining and regulating Sc occurrence [Wood, 2012]. Previous studies have found that marine Sc drizzle frequently [Nicholls and Leighton, 1986; Wood, 2005a; Wood, 2012; Wu et al., 2015] and that much, if not most, of the drizzle evaporates before reaching the ground [Comstock et al., 2004; Wu et al., 2015]. Precipitation directly depletes cloud liquid water, and indirectly can limit the flux of water vapor into the cloud layer because cooling and moistening the atmosphere beneath clouds (via evaporation) can stabilize the boundary layer [Austin et al., 1995; Comstock et al., 2005; Wood, 2012]. The radiative properties of clouds are strongly related to the number and size of cloud particles and precipitation, through its influence on cloud water, affects how much sunlight cloud can reflect back to space. Precipitation can also affect cloud lifetime and cloud-aerosol interactions by scavenging aerosols in the boundary layer, with individual precipitation particle often fusing multiple aerosol particles and depositing them into the ocean [Ohata et al., 2016; Dzambo et al., 2019], while higher aerosol numbers are thought to suppress the formation of precipitation and increase cloud life time since more-but-smaller cloud droplets will decrease the rate at which cloud droplets can grow into particles large enough to sediment. [Lohmann and Feichter, 2001; Posselt and Lohmann, 2009; Wood et al., 2015].

Models employ a variety of explicit and bulk microphysics schemes to represent precipitation. Explicit microphysical schemes predict the drop size distribution (DSD) function by dividing droplets into many bins, typically based upon the size or mass of the particles, and modeling the evolution of each bin separately [Kogan, 1991; Khain et al., 2015]. Bulk microphysical schemes, on the other hand, prescribe the form of the DSD function (e.g. a gamma or lognormal distribution) and predict the moments of the function [Kessler 1969; Khain et al., 2015]. Bulk microphysics are widely adopted due to their simplicity and high computational efficiency. In bulk microphysics, cloud droplets and precipitation droplets are usually represented using separate DSDs, with precipitation having larger droplets. This paradigm was first introduced by Kessler [1969] and is widely used in warm rain parameterizations [Wood, 2015b]. Under this paradigm, the generation of precipitation water content typically follows two pathways: autoconversion (the collision of small cloud droplets to form larger precipitation drops, which initiates precipitation) and accretion (the collection of cloud droplets by falling precipitation drops, which increases precipitation particle size and amount/mass). Over the years, many formulations for the autoconversion rate have proposed (see Table 3.1), and most can be expressed as a power law equation in terms of cloud water mixing ratio ($q_c$) and cloud droplet number concentrations (N), which can be written in a general form as:

$$M_{auto} = a_{au} N^{b_N} {q_c}^{b_{au}} \tag{3.1}$$

where $M_{\text{auto}}$ is the autoconversion rate with typical units of kg kg$^{-1}$ s$^{-1}$. $q_c$ has units of kg/kg, N has units of cm$^{-3}$, and $a_{au}$, $b_N$ and $b_{au}$ are constant coefficients. In the following sections, we present results based on the constants used in the Khairoutdinov and Kogan [2000, hereafter KK2000] parameterization with $a_{au}$ = 1350, $b_N$ = -1.79, $b_{au}$ = 2.47, since this scheme is widely

used, was specifically developed for Sc, and appears to produce more realistic simulations than some earlier formulations [Wood et al., 2002]. Results for other combinations of these constants as shown in Table 3.1 can be easily obtained.

*Table 3.1 Parameterization schemes for autoconversion rate ($M_{auto}$) and the corresponding $b_{au}$ and $b_N$ as in equation (3.1). The unit is kg kg$^{-1}$s$^{-1}$ for autoconversion rate, kg kg$^{-1}$ for cloud water mixing ratio ($q_c$) and m$^{-3}$ for total number concentration ($N_c$). $\rho_a$ and $\rho_w$ represent air and liquid water density, respectively and both have the unit of kg/m$^3$. Part of the data is recompiled from Table 1 in Wood (2005b).*

| Scheme | Autoconversion Rate ($M_{auto}$) | $b_{au}$ | $b_N$ |
|---|---|---|---|
| Berry (1968) | $\frac{3.5 \times \rho_a \times 10^{-2} q_c^2}{0.12 + 1.0 \times 10^{-12} \frac{N_c}{\rho_a q_c}}$ | ~3 | ~-1 |
| Kessler (1969) | $\begin{cases} K(q_c - q_c^*) & for\ q_c > q_c^* \\ 0 & for\ q_c \le q_c^* \end{cases}$ | 1 | 0 |
| Tripoli and Cotton (1980) | $\frac{0.104 g E_{cr}}{\mu \rho_w^{1/3}} \rho_a^{5/3} q_c^{7/3} N_c^{-1/3} h(q_c - q_{crit})$ | 7/3 | -1/3 |
| Beheng (1994) | $6.0 \times 10^{28} n^{-1.7} \rho_a^{3.7} (q_c \times 10^{-3})^{4.7} (N_c \times 10^{-6})^{-3.3}$ | 4.7 | -3.3 |
| KK (2000) | $1350\, q_c^{2.47} {N_c}^{-1.79}$ | 2.47 | -1.79 |
| Liu and Daum (2004) | $\left(\frac{3}{4\pi\rho_w}\right)^2 \kappa_2 \beta_6^6 \rho_a^2 q_c^3 N_c^{-1} h(R_6 - R_{6c})$ | 3 | -1 |
| Seifert and Beheng (2006) | $\frac{K_{cc}}{20x^*} \frac{(V_c+2)(V_c+4)}{(V_c+1)^2} \times \rho_a^3 q_c^4 {N_c}^{-2} \left[1 + \frac{\Phi_{au}(\tau)}{(1-\tau)^2}\right]$ | 4 | -2 |

Accretion rate is likewise approximated by a nonlinear power law equation in terms of cloud water mixing ratio and precipitation water mixing ratio ($q_p$) with the following form:

$$M_{accr} = a_{ac} {q_c}^{b_{acc}} {q_p}^{b_{acp}} \tag{3.2}$$

where $M_{\mathrm{accr}}$ is the accretion rate (in kg kg$^{-1}$ s$^{-1}$), $q_p$ has units of kg/kg, and $a_{ac} = 67$ with $b_{acc}$ = $b_{acp}$ = 1.15 in KK2000. Again, various parameterization schemes fit this general form, as shown in Table 3.2. It is worth noting that different formulations for accretion rate agree much better with each other in terms of the constants than do the formulations for autoconversion rate.

*Table 3.2 Same as Table 3.1 but for accretion rate ($M_{accr}$). $b_{acc}$ and $b_{acp}$ are the coefficients as in equation (3.2). Part of the data is recompiled from Table 1 in Wood (2005b).*

| **Scheme** | **Accretion Rate ($M_{accr}$)** | $b_{acc}$ | $b_{acp}$ |
|---|---|---|---|
| Kessler (1969) | $0.29 N_c^{1/8} \rho_a^{7/8} q_c q_r^{7/8}$ | 1 | 7/8 |
| Tripoli and Cotton (1980) | $0.884 E_{cr} \left(\frac{g\rho_a}{\rho_w R_m}\right)^{1/2} q_c q_r$ | 1 | 1 |
| Beheng (1994) | $6 q_c q_r \rho_a$ | 1 | 1 |
| KK (2000) | $67 (q_c q_r)^{1.15}$ | 1.15 | 1.15 |
| Seifert and Beheng (2006) | $K_{cr} \rho_a q_c q_r \Phi_{ac}(\tau)$ | 1 | 1 |

In many climate models, boundary layer clouds over the ocean produce precipitation that occurs too frequently and too lightly [Dai, 2006; Stephens et al., 2010; Nam and Quaas, 2012; Trenberth

and Zhang, 2017; Chen and Dai, 2019]. This includes simulations from CAM4, CAM5 and the so-called Multiscale Modeling Framework (MMF) associated with the CAM [Wang et al. 2012; Marchand et al. 2009; Zhao et al., 2017]. In the MMF, a small 2D or 3D cloud-resolving model is embedded into each grid cell of a host model to replace cloud and precipitation parameterizations. The over prediction of light precipitation suggests an imbalance between autoconversion and accretion rates [Wang et al., 2012; Morrison and Gettelman, 2008; Wu et al. 2018, hereafter W2018].

Because the autoconversion and accretion rates are non-linear functions, one should not calculate the process rates based on model-grid-mean values for $\overline{q_c}$, $\overline{N}$ and $\overline{q_p}$, but rather the spatial variability of the microphysics needs to be considered [Pincus and Klein, 2000; Larson et al., 2001; Wood et al. 2002, Yuan et al. 2006; Weber and Quaas 2012; Song et al., 2018]. Note that only the in-cloud variability of the variables is considered here. In practice, the spatial variability is often represented by a probability distribution function (PDF) with a simple analytical form and the processes rates can be analytically integrated over the PDF, such that the effect of the subgrid variability can be represented by an enhancement factor, where the process rate is given by the value calculated assuming no variability multiplied by the enhancement factor.

For example, Lebsock et al. [2013], hereafter L2013, adopt a lognormal distribution to represent subgrid variability of $q_c$ within cloud and a bivariate lognormal distribution to represent the covariance between $q_c$ and $q_p$. Using CloudSat and MODIS data, they found the covariance between $q_c$ and $q_p$ is important to the accretion rate, and neglecting this covariance results in a significant underestimate of the accretion rate. Similar conclusions were drawn by Boutle et al.

[2014, hereafter B2014] who adopted the same PDF form but used data from CloudSat and a combination of aircraft in situ measurements and ground-based measurements. B2014 suggested biases in both autoconversion and accretion rates of a factor ranging from about 2 (for a grid size near 5 km) to 5 (for a grid size near 100 km) will occur if one neglects subgrid variability and covariability. That subgrid variability is important to the parameterization of microphysical processes at scales of only a few kilometers is also supported by results published by Larson et al. [2012] who examined the impact of a PDF parameterization for subgrid variability, the Cloud Layers Unified By Binormals (CLUBB), in the System for Atmospheric Modeling (SAM) cloud resolving model. Larson et al. found that including CLUBB in the simulations significantly improved cloud and drizzle water contents at 4 km and 16 km grid spacing, reducing the sensitivity of the simulations to horizontal grid spacing. Likewise, the subgrid variability of N has also been investigated. W2018 found the effect of subgrid variability of N on autonconversion rate is comparable to that of $q_c$ based on radar retrievals of Sc in Azores (39.09ºN, 28.03ºW). Using MODIS data, Zhang et al. [2019] demonstrated that both subgrid variability of N and the covariability of N and $q_c$ were important for simulating the autoconversion rate in GCMs especially over tropical oceans.

In this chapter, we examine both autoconversion and accretion enhancement factors for marine stratocumulus observed at the ARM Eastern North Atlantic (ENA) site based on simultaneous-retrieval of cloud liquid water content (CLWC) and precipitation liquid water content (PLWC), as described in Chapter 2. In section 3.2 we describe the data and the bivariate-lognormal PDF approach that has often been used to represent subgrid variability of $q_c$ and $q_p$ in order to calculate the autoconversion and accretion rates enhancement factors. In section 3.3, we investigate the performance of the PDF approach by comparing it to the unbiased (true)

enhancement factor calculated directly using local quantities. As in previous studies we examine the dependency of enhancement factors on the model horizontal grid scale, but also explore the dependency on precipitation fraction, the vertical position in the cloud, surface relative humidity (RH), and lower-tropospheric stability (LTS), as well as the grid-scale mean and standard deviation in cloud liquid water path (LWP), cloud thickness and cloud base height. Perhaps surprisingly the vertical dependence of autoconversion and accretion has not been widely considered in previous investigation of enhancement factors. Additional discussions and conclusions are given at the end in Section 3.4. In particular, we discuss our results in the context of previous studies.

## 3.2 Data and Methods

### 3.2.1 *Cloud Microphysical Data*

The retrieval algorithm described in Chapter 2 is applied to determine CLWC and PLWC for each radar range gate in the cloud using measurements from the Atmospheric Radiation Measurement (ARM) program Ka-band Zenith Radar (KAZR) located in the Azores [Kollias et al., 2011; DOI:10.5439/1025218]. This location has a high occurrence of Sc and a long-term ground-based observations which greatly facilitate Sc studies [Dong et al., 2014]. In brief, the retrieval algorithm uses a Doppler spectra decomposition technique to separate the Doppler spectra that exhibit a bimodal distribution into cloud and precipitation components and thereby determine the reflectivity factor, Doppler velocity and spectral width associated with each component. Precipitation fall (sedimentation) velocity is determined from difference in the Doppler velocity between the two components, since the mean Doppler velocity of the cloud component is due almost entirely to the (range-bin mean) air velocity. PLWC is then calculated

using the retrieved precipitation reflectivity, fall velocity and precipitation spectral width following the theory developed by Frisch et al. [1995]. Not all the radar range bins have a separable Doppler spectrum. Empirical equations are fitted based on the separable retrievals and are used to extrapolate the data to the radar range bin with non-separable spectra. CLWC is calculated assuming it linearly increases with altitude in the cloud and with the liquid water path (LWP) constrained by retrievals for total LWP from the microwave radiometer [Cadeddu et al., 2009; DOI:10.5439/1025248]. When microwave radiometer retrieval for total LWP are not available (most frequently because the MWR surface is wet), an adiabatic cloud model is implemented with CLWC adjusted by an adiabatic factor that is tuned on a case by case basis to match good data from the MWR.

For simplicity, our analysis is restricted to days with near overcast single-layered clouds that meet the following criteria:

i) Maximum cloud top is below 2.5 km.

ii) Largest change in the cloud base (maximum - minimum) does not exceed 1.5 km.

iii) Cloud fraction (fraction of time clouds is above the radar) is larger than 80%.

From observations collected between October 1, 2015 and April 1, 2018, 48 cases (days) were identified. We convert time to approximate horizontal distance using wind speed from the Interpolated Sonde Value-Added Product [DOI:10.5439/1095316]. We also use temperature and relative humidity from this product.

### 3.2.2 *Subgrid Variability*

Here, we use the fractional standard deviation (Eq. 3.3) to characterize subgrid variability:

$$f = \frac{\sigma}{\mu} \tag{3.3}$$

where σ is the standard deviation of a variable q and $\mu$ is its mean value. Large values of $f$ indicate large relative variability and vice versa. In L2013 and B2014, the spatial variability of $q_c$ and $q_p$ are represented by a lognormal distribution analytically,

$$\mathrm{P(q)} = \frac{1}{\sqrt{2\pi} q \sigma_{ln}} \exp\left(-\frac{(ln(q)-\mu_{ln})^2}{2\sigma_{ln}^2}\right) \tag{3.4}$$

where $\mu_{ln}$ and $\sigma_{ln}$ are the mean and standard deviation of the variable's natural logarithm. The parameters, $\mu_{ln}$ and $\sigma_{ln}$, can be estimated from observations in several ways. Two practical ways are the method of moments (MOM) [Hazelton, 2011] and the maximum likelihood estimation (MLE) [Hogg and Tanis, 2020]. The MOM works by equating the distribution moments with the moments of samples, i.e. $\mathrm{E(q)} = \frac{\sum_{i=1}^{n} q_i}{n}$ and $\mathrm{E}(q^2) = \frac{\sum_{i=1}^{n} {q_i}^2}{n}$, Where E(q) here is the expected value given by (defined as) $\mathrm{E(q)} = \int q\mathrm{P(q)}\, dq$. For lognormal distribution, Eq. (3.4), one can shows that $\mathrm{E(q)} = \exp\left(\mu_{ln} + \frac{{\sigma_{ln}}^2}{2}\right)$ and $\mathrm{E}(q^2) = \exp(2\mu_{ln} + 2{\sigma_{ln}}^2)$. $\mu_{ln}$ and $\sigma_{ln}$ can be then obtained and expressed as:

$$\mu_{ln}^{MOM} = -\frac{\ln(\sum_{i=1}^{n} q_i^2)}{2} + 2\ln(\sum_{i=1}^{n} q_i) - \frac{3}{2}\ln(n) \tag{3.5}$$

$$\sigma_{ln}^{MOM} = \sqrt{\ln(\sum_{i=1}^{n} q_i^2) - 2\ln(\sum_{i=1}^{n} q_i) + \ln(n)} \tag{3.6}$$

By construction, the mean and standard deviation of variable q based on the MOM are:

$$\mu^{MOM} = \frac{\sum_{i=1}^{n} q_i}{n} \tag{3.7}$$

$$\sigma^{MOM} = \sqrt{\frac{\sum_{i=1}^{n}\left(q_i - \frac{\sum_{i=1}^{n} q_i}{n}\right)^2}{n}} \tag{3.8}$$

The MLE technique works by finding the parameters that maximize the likelihood (probability) of getting the samples observed. The likelihood function for samples from the lognormal distribution is [Hogg and Tanis, 2020]:

$$\mathrm{L}(\mu_{ln}, {\sigma_{ln}}^2|\mathrm{q}) = \prod_i^n P(q_i|\mu_{ln}, {\sigma_{ln}}^2) = \prod_i^n \frac{1}{\sqrt{2\pi} q_i \sigma_{ln}} \exp\left(-\frac{(ln(q_i)-\mu_{ln})^2}{2\sigma_{ln}^2}\right) \tag{3.9}$$

Simply put, the likelihood for getting some set of values $q_i$ is given by the multiplicative product (Π) of the probability of getting each value given $\mu_{ln}$ and ${\sigma_{ln}}^2$. One can show that maximizing this function for $\mu_{ln}$ and ${\sigma_{ln}}^2$ yields:

$$\mu_{ln}^{MLE} = \frac{\sum_{i=1}^{n} \ln(q_i)}{n} \tag{3.10}$$

$$\sigma_{ln}^{MLE} = \sqrt{\frac{\sum_{i=1}^{n}\left(\ln(q_i) - \frac{\sum_{i=1}^{n} \ln(q_i)}{n}\right)^2}{n}} \tag{3.11}$$

The mean and standard deviation of variable q ($\mu = \mathrm{E}(q)$ $and$ $\sigma = \sqrt{\mathrm{E}((q-\mu)^2)}$, respectively) based on the lognormal distribution obtained by using the MLE are:

$$\mu^{MLE} = \exp\left(\mu_{ln} + \frac{{\sigma_{ln}}^2}{2}\right) \tag{3.12}$$

$$\sigma^{MLE} = \sqrt{[\exp({\sigma_{ln}}^2) - 1]\exp(2\mu_{ln} + {\sigma_{ln}}^2)} \tag{3.13}$$

The values of fractional standard deviation are calculated using Eq. (3.3) for both methods and are used to calculate enhancement factors as described later. If enough samples are drawn from a true lognormal distribution, the values estimated by the MOM and MLE will be the same. However, since the PDF of $q_c$ and $q_p$, in practice, are not perfectly lognormally distributed, which method is better is examined in the section 3.3.

### 3.2.3 *Enhancement Factor*

The effect of subgrid variability on the grid mean autoconversion rate can be calculated by integrating Eq. (3.1) over Eq. (3.4). B2014 show that:

$$\overline{M_{auto}} = \int M_{auto}\, P(q_c) dq_c = a_{au} N^{b_N} \int {q_c}^{b_{au}} P(q_c)\, dq_c = E_{auto}(f_c, b_{au}) M_{auto} \quad (3.14)$$

where $E_{auto}$ is the analytical enhancement factor given as:

$$E_{auto}(f_c, b_{au}) = (1 + f_c^2)^{\frac{-b_{au}}{2}} (1 + f_c^2)^{\frac{b_{au}^2}{2}} \quad (3.15)$$

where $f_c$ is the fractional standard deviation of $q_c$. The benefit of using the PDF approach is that the analytical form of $E_{auto}$ can be directly derived and calculated if $f_c$ is known. For a given $b_{au}$ (2.47 here), $E_{auto}$ increases monotonically with $f_c$ as shown by the black line in Fig. 3.1. As indicated by Eq. (3.15), $E_{auto}$ will increase with $b_{au}$ as long as $b_{au}$ is no less than 1 which is satisfied by all the autoconversion schemes listed in Table 3.1. Here, N has been assumed to be a constant, which means the subgrid variability of N (and any correlation with $q_c$) is ignored. The implication of this assumption will be discussed later.

For accretion process, one has to integrate Eq. (3.2) over the joint distribution of $q_c$ and $q_p$. Again, following B2014, we represented the joint distribution as a bivariate lognormal distribution, which is:

$$P(q_c, q_p) = \frac{1}{2\pi q_c q_p \sigma_c \sigma_p \sqrt{1-\rho^2}} \exp\left(-\frac{(ln(q_c)-u_c)^2}{2{\sigma_c}^2(1-\rho^2)}\right) \exp\left(-\frac{(ln(q_p)-u_p)^2}{2{\sigma_p}^2(1-\rho^2)}\right) \exp\left(-\frac{\rho(q_c-u_c)(q_p-u_p)}{\sigma_c \sigma_p (1-\rho^2)}\right) \quad (3.16)$$

Integrating Eq. (3.2) over this distribution yields:

$$\overline{M_{accr}} = E_{accr}(f_c, f_p, \rho, b_{ac}) M_{accr} \tag{3.17}$$

Where $f_p$ is the fractional standard deviation of $q_p$, $\rho$ is the cross correlation coefficient between $q_c$ and $q_p$ and the analytical accretion enhancement factor $E_{accr}$ is:

$$E_{accr}(f_c, f_p, \rho, b_{ac}) = (1 + f_c^2)^{\frac{-b_{acc}}{2}} (1 + f_c^2)^{\frac{b_{acc}^2}{2}} (1 + f_p^2)^{\frac{-b_{acp}}{2}} (1 + f_p^2)^{\frac{b_{acp}^2}{2}}$$
$$\exp\left(\rho b_{acc} b_{acp} \sqrt{ln(1 + f_c^2)\, ln(1 + f_p^2)}\right) \tag{3.18}$$

As shown by Eq. (3.18), $E_{accr}$ is a function of $f_c$, $f_p$ and $\rho$. How these parameters affect $E_{accr}$ is demonstrated in Fig. 3.1 ($b_{acc}$ and $b_{acp}$ set to 1.15 following KK2000). As shown by the orange line, with $f_p$ fixed at 0.90 (the mean value we obtain later for a grid size of 50 km) and $\rho$ set to 0.53 (again the mean value for a grid size of 50 km), $E_{accr}$ increases monotonically with $f_c$. If $\rho$ is set to 0 (blue line) meaning if correlation between cloud and precipitation liquid water is ignored, $E_{accr}$ decreases significantly compared to that with $\rho$ (orange line), which demonstrates the importance of covariability between $q_c$ and $q_p$. If $f_p$ is also ignored ($f_p = 0$ and $\rho = 0$, red line), $E_{accr}$ becomes only slightly smaller. In the next section, the assumption that $q_c$ and $q_p$ are lognormally distributed and how the analytical enhancement factors (Eqs 3.15 and 3.18) derived from this assumption compare with unbiased (true or directly calculated) values are examined. Furthermore, how the unbiased $E_{auto}$ and $E_{accr}$ change with various variables are investigated such as grid size (scale), precipitation fraction, vertical position in the cloud, surface RH, LTS, LWP and cloud thickness.

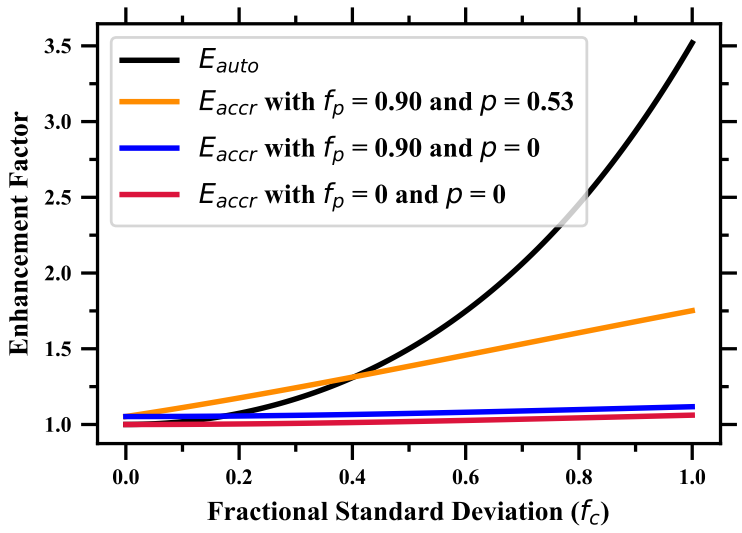


*Figure 3.1 Example demonstrated dependence of $E_{auto}$ (black) and $E_{accr}$ on the fractional standard deviation ($f_c$). Orange line represents $E_{accr}$ when $f_p$ = 0.90 and $\rho$ = 0.53. Blue line represents when $f_p$ = 0.90 and $\rho$ = 0.*

## 3.3 Results

### 3.3.1 *Case Study*

We begin with an examination of a stratocumulus cloud deck observed on July 18, 2017. Fig 3.2(a) shows the reflectivity factor observed by the ARM KAZR cloud radar. Here, the black dots represent cloud base which was determined from a combination of ceilometer and micropulse lidar [Clothiaux et al. 2000]. There is a large area below cloud base where the radar reflectivity reveals drizzle is present, and drizzle is present to varying degrees in all the cases examined in this study. Two periods from this day that are highlighted in Fig 3.2(a) are shown in greater details in Figs 3.2(b) and 3.2(c). Based on the wind speed from the interpolated radiosonde data, these segments correspond to a grid size of about 50 km. In the first period (Fig 3.2(b)), the drizzle is relatively light and reflectivity factors are relatively small as compared with the second period (Fig 3.2(c)). The third and fourth row of panels in Fig 3.2 show the associated

time series of in-cloud layer-mean $q_c$ (third row of panels) and $q_p$(bottom panels) for the first period (left panels) and the second period (right panels). These plots demonstrate that large variability in both $q_c$ and $q_p$ exists in both periods, and I will examine the impact this has on the enhancement factors, momentarily. Here and later in this chapter, the term "in-cloud layer-mean" indicates that the drizzle liquid water mixing ratio has been averaged over the depth of the cloud (in the vertical) but does NOT include drizzle below the cloud. Comparing these two periods, the mean of $q_c$ is about the same (0.3 g/kg during period 1 and 0.35 g/kg during period 2), but the mean of $q_p$ is much larger during the second period, 0.01 and 0.05 g/kg, respectively. The in-cloud layer-mean $q_c$ and $q_p$ values are positively correlated with correlation coefficients ($\rho$) being 0.66 and 0.84 for period 1 and 2, respectively.

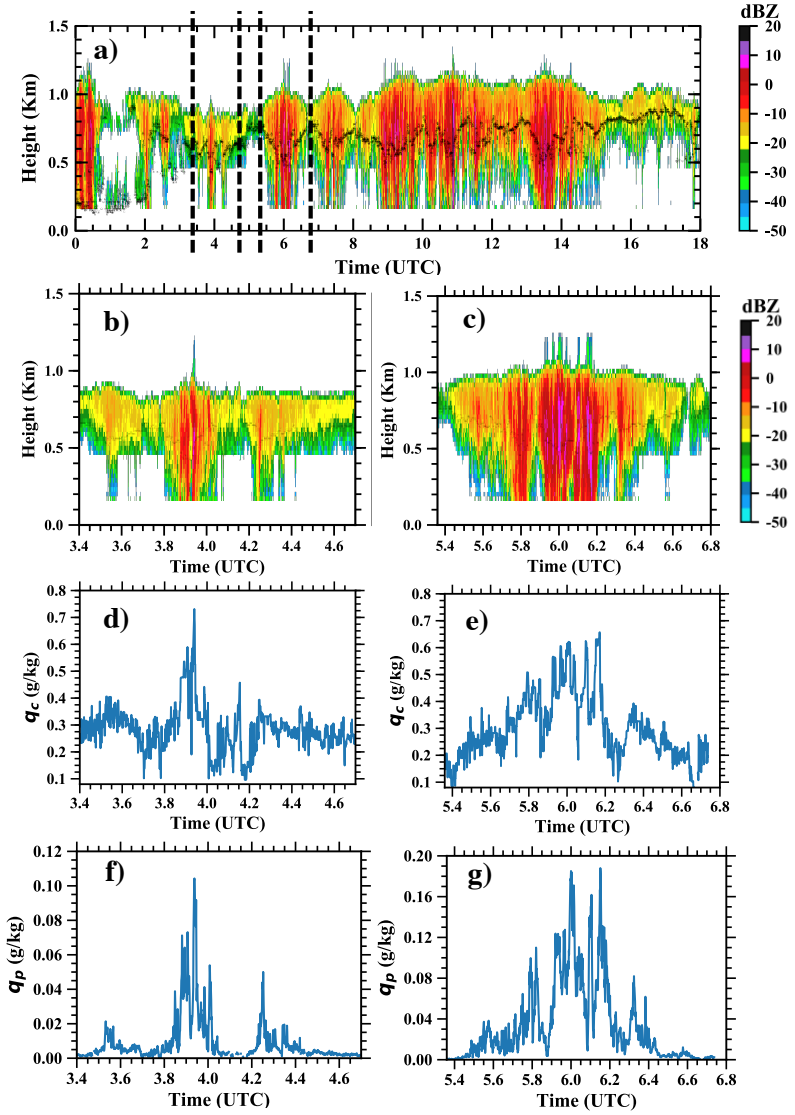


*Figure 3.2 (a) Reflectivity factor on July 18, 2017 at the ARM ENA site with two periods (denoted by the dash lines) highlighted. Each period is equivalent to a region of about 50 km. The black dots indicate cloud base. (b), (d) and (f) show the reflectivity factor, in-cloud layer-mean of $q_c$ and $q_p$, respectively for the first (earlier) period. (c), (e) and (g) are counterparts for the second period.*

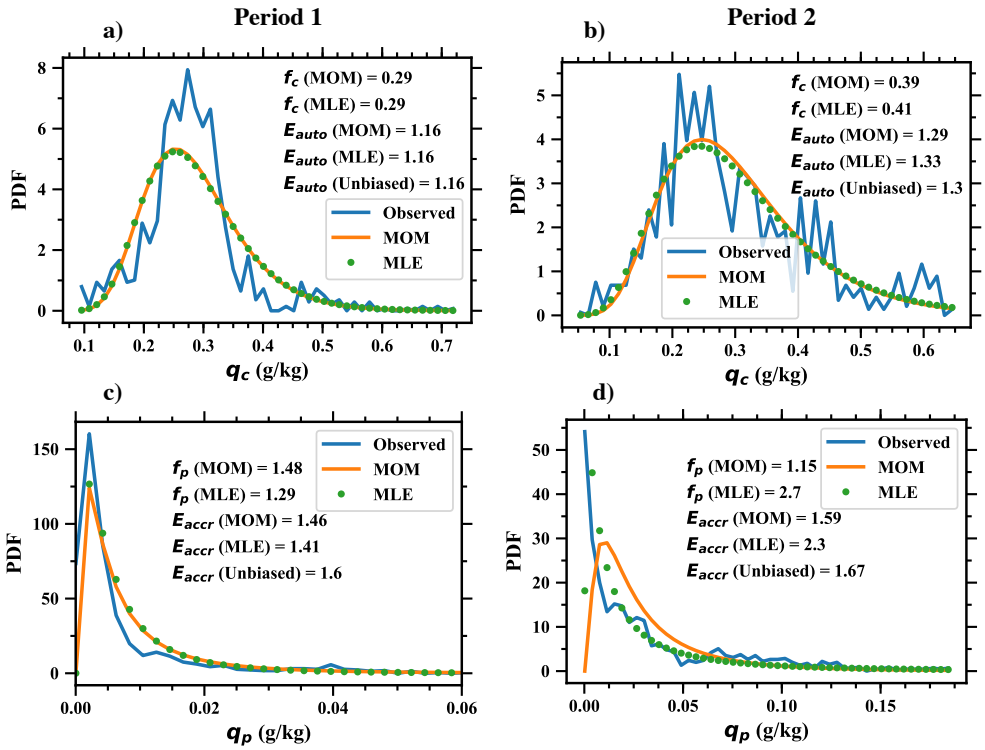


*Figure 3.3 PDF that is observed (blue solid line), estimated by the MOM (orange solid line) and the MLE (green dot line) for $q_c$ of period 1 (a), $q_c$ of period 2 (b), $q_p$ of period 1 (c) and $q_p$ of period 2 (d). The corresponding fractional standard deviations ($f$) and enhancement factors ($E$) are shown in each subplot.*

The derivations of Eqs. (3.15) and (3.18) for the enhancement factors are based on the assumption that $q_c$ and $q_p$ have a lognormal distribution. We evaluate this assumption in Fig 3.3 for both $q_c$ (upper panels) and $q_p$ (bottom panels) in period 1 (left panels) and period 2 (right panels). In each subplot, a histogram obtained from the observations is shown in blue, the PDF whose parameters are estimated by the MOM is shown by the brown solid line, and the PDF based on parameters obtained from the MLE is shown by the green dot line. The corresponding $f_c$ or $f_p$ using both methods are shown in each subplot along with the enhancement factor $E_{auto}$ or $E_{accr}$ calculated using Eqs. (3.15) and (3.18). The unbiased or true value for $E_{auto}$ or $E_{accr}$ is also listed and is computed directly from retrieved quantities, that is the grid-mean of the local

microphysical rates (calculated from Eqs. (3.1) and (3.2) based on the layer-mean retrieved values from the cloud radar) divided by the microphysical rate calculated using the 50 km-mean value for $q_c$ and $q_p$. Although not perfectly lognormal, the distributions of observed $q_c$ in period 1 (Fig 3.3(a)) and period 2 (Fig 3.3(b)) are close to lognormal, and not surprisingly the difference between the MOM and MLE estimates is small, and the estimated $f_c$ and $E_{auto}$ compare well with the unbiased (true) value. The observed $q_p$ (Fig 3.3(c) and Fig 3.3(d)) is much more skewed compared to $q_c$ and a lognormal distribution does not fit the observations as well. The estimated $E_{accr}$ by the MOM and MLE for period 1 is 1.46 and 1.41, respectively, whereas the unbiased value is 1.6. For period 2, the unbiased value is 1.67 but estimated $E_{accr}$ is 1.59 by the MOM and 2.3 by the MLE. Overall the result based on the MOM estimates compares better to the unbiased (true) value than the MLE result. Meanwhile, $E_{auto}$ and $E_{accr}$ are larger in period 2 than in period 1 indicating that enhancement factors and LWP might be correlated which will be investigated in detail in section 3.6.

Overall, we find that the MOM approach works better than MLE in estimating $E_{auto}$ and $E_{accr}$. Fig 3.4(a) shows a scatter plot between the unbiased $E_{auto}$ and $E_{auto}$ estimated using the MOM approach for a grid size of 50 km based on all 48 days of data which we have processed, and Fig 3.4(b) shows a similar scatter plot using the MLE approach. The mean $E_{auto}$ is 1.35 by the MOM and 1.44 by the MLE compared to the unbiased mean value of 1.36. Meanwhile, the correlation coefficient is nearly 1 using the MOM, which is notable better than the 0.81 obtained using the MLE. For $E_{accr}$, the MOM values are again better correlated with the unbiased values (than MLE) though the MOM values are consistently biased low by about 5%.

Regardless of which technique is used to estimate the fractional standard deviations, the important point here is that while the observed (radar retrieved) distributions of $q_c$ and $q_p$ do not appear to be completely lognormal, this assumption does not appear to be a serious problem for modeling the enhancement factors using Eqs. (3.15) or (3.18) and does not cause much bias, at least for subtropical marine Sc investigated here. In the following section, we investigate the dependency of unbiased $E_{auto}$ and $E_{accr}$ on various variables and use the MOM based estimates when evaluating the ability of the PDF formulation to predict $E_{auto}$ and $E_{accr}$.

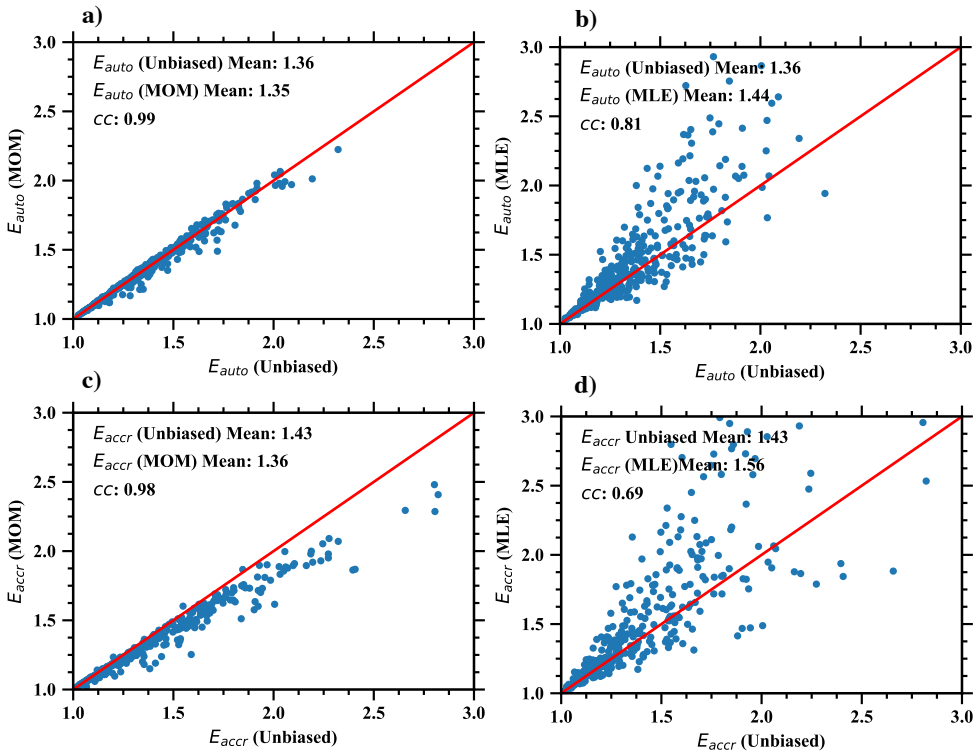


*Figure 3.4 Statistical comparisons of unbiased $E_{auto}$ with $E_{auto}$ calculated through the MOM (a) and the MLE (b) for a grid size of 50 km. The mean values and their correlation coefficient (cc) are shown in the plot. (c) and (d) are counterparts for $E_{accr}$. The results are based on 48 cases all of which are single-layered near overcast Sc at the ARM ENA site. The same is true for the rest of figures.*

### 3.3.2 *Dependence on Grid Size*

Intuitively, one might expect that as the model grid size becomes larger, the subgrid variability will increase (because larger-and-larger circulations become unresolved) and consequently enhancements factors will become larger. Fig 3.5 shows box-and-whisker plots of $E_{auto}$ (a), $E_{accr}$ (b), $f_p$ (c) and $\rho$ (d) for grid sizes varying from 5 to 200 km (blue lines). We note that the change of $f_c$ is not shown because $f_c$ has a similar pattern of variation with grid size as $E_{auto}$. The box shows the 25th percentile, median (orange line) and 75th percentile of the data. Results show that the mean and median of $E_{auto}$, $E_{accr}$ and $f_p$ increase relatively rapidly from 5 to 100 km and then more slowly from 100 to 200 km as most of the variability is already incorporated by the time one reaches a 100 km grid-scale. While there is some scale dependency in the cross correlation coefficient between $q_c$ and $q_p$ the change is modest especially at scales larger than about 50 km (though we note there is a significant vertical dependence, which is discussed in the next section). This scale dependency in $E_{auto}$, $E_{accr}$ and $f_p$ is mainly due to the standard deviation of $q_c$ and $q_p$ rather than the mean. The PDF of $E_{auto}$ at grid size of 50 and 200 km is compared more directly in Fig. 3.6(a), which demonstrates a clear shift toward larger enhancement factors at a grid size of 200 km compared to 50 km, and the same is true for $E_{accr}$ shown in Fig 3.6(b). The mean of $E_{auto}$ at the grid size of 50 and 200 km are 1.36 and 1.49, respectively, whereas the mean of $E_{accr}$ is 1.4 and 1.66, respectively. This is not to suggest that the effect of subgrid variability should be ignored at small scales. Even at a scale of 5 km, the mean of $E_{auto}$ and $E_{accr}$ are about 1.1. The calculation of $E_{auto}$ using the PDF model (Eq. 3.15) has the same dependency on grid scale as the unbiased $E_{auto}$ shown here, and similarly, $E_{accr}$ based on the PDF has the same pattern as the unbiased values.

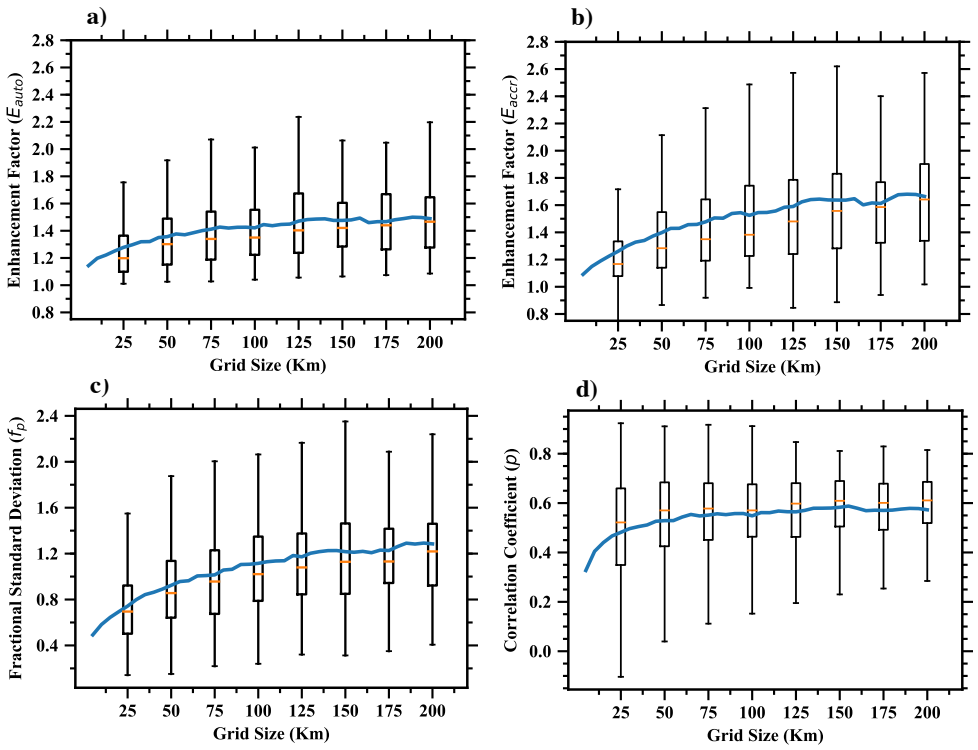


*Figure 3.5 Change of $E_{auto}$ (a), $E_{accr}$ (b), $f_p$ (c) and ρ (d) with grid size (blue solid line). Box and whisker plots at specific grid size are shown with each box showing the 25th and 75th percentile of the data and the orange line showing the median.*

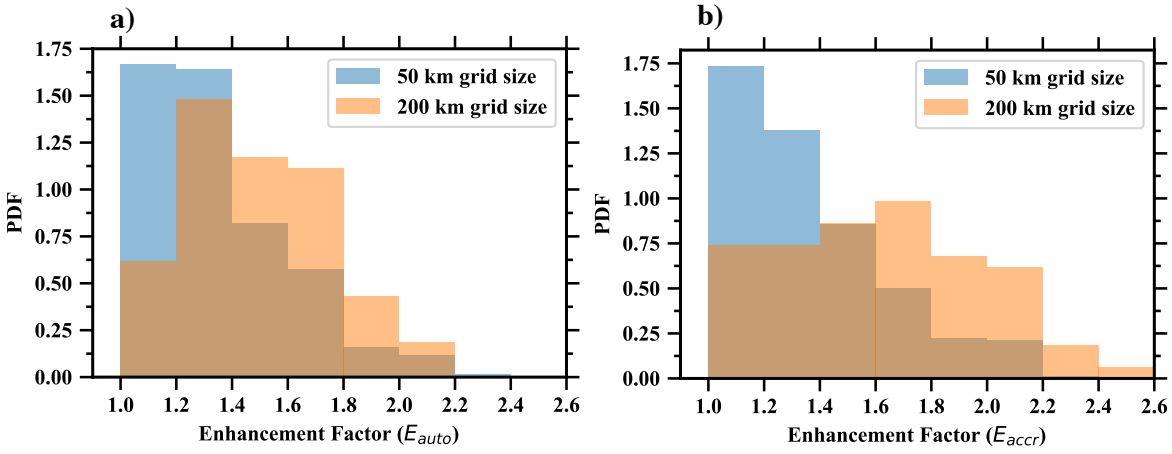


*Figure 3.6 PDF of $E_{auto}$ (a) and $E_{accr}$ (b) for the grid size of 50 km and 200 km.*

### 3.3.3 *Dependence on Precipitation Fraction*

Using aircraft and satellite observations, B2014 examined the dependence of $f_p$ on precipitation fraction (the fraction of time that precipitation is detected at a grid-scale), which we revisit here. We note B2014 also examined the dependence of $f_c$ on cloud fraction, but our analysis is restricted to single-layered near overcast clouds.

As described in section 3.2, our radar-based microphysical retrieval algorithm determines the amount of precipitation that is present down to very small values of radar reflectivity (-30 dBZ) such that precipitation water in very small quantities is almost always present and using a threshold for "precipitation present" of 0 g/m3 would yield a precipitation fraction that is large. In order to make our results compare to B2014, we instead define precipitation fraction as the number of radar profiles whose reflectivity at cloud base is larger than -20 dBZ divided by the total number of profiles in a grid (50 km). This is still a fairly sensitive measure for precipitation occurrence, as -20 dBZ corresponds to a rain rate of roughly 0.01 mm/hr (at cloud base), and precipitation this light rarely reaches the surface (before completely evaporating). We note that the threshold is only for calculating precipitation fraction but not for filtering out smaller $q_p$ values, meaning all the layer-mean in-cloud $q_p$ are used to calculate $f_p$ regardless of the threshold.

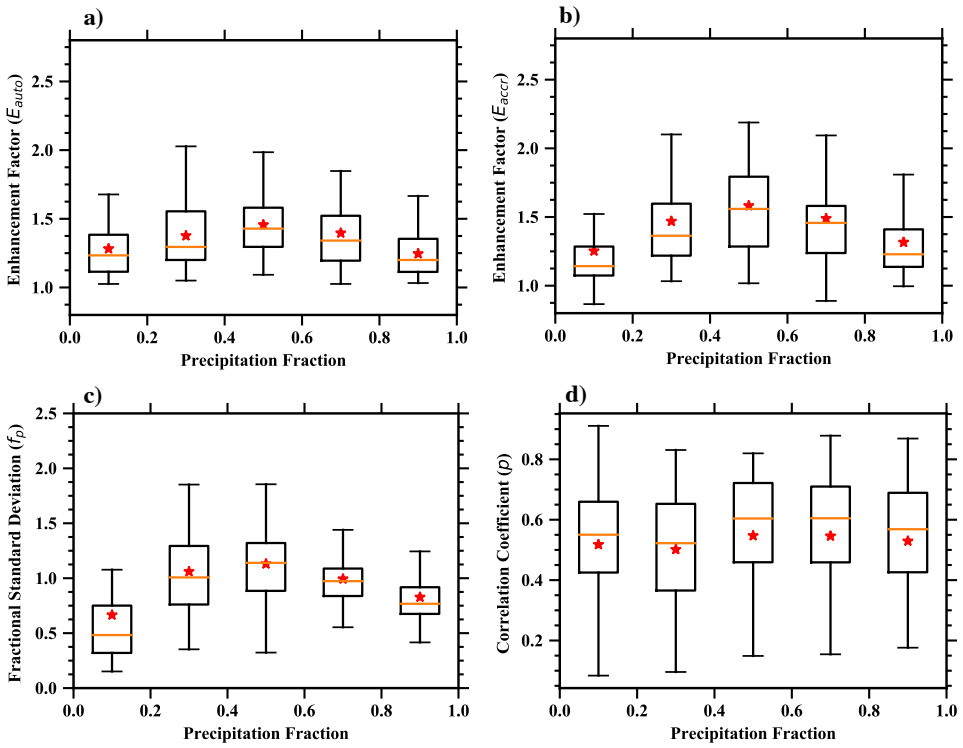


*Figure 3.7 Box and whisker plots of $E_{auto}$ (a), $E_{accr}$ (b), $f_p$ (c) and ρ (d) at different precipitation fractions. The box shows the 25th and 75th of the data, the horizontal orange line represents the median and the red star represents the mean. The results are calculated for a grid size of 50 km.*

In Fig 3.7, box-and-whisker plots of $E_{auto}$ (a), $E_{accr}$ (b), $f_p$ (c) and $\rho$ (d) are shown with precipitation fraction broken into pentads. The box shows the 25th percentile, median (orange line) and 75th percentile of the data in each precipitation fraction interval with the mean values are denoted by the red stars. Fig 3.7 demonstrates that both the mean and median of $E_{auto}$ and $E_{accr}$ are largest when precipitation fraction is between 0.4 and 0.6. $f_c$ (not shown) has a similar pattern of variation with precipitation fraction as $E_{auto}$. The change in $E_{accr}$ is mainly due to $f_p$ (Fig 3.7(c)) and $f_c$ as $\rho$ stays relatively unchanged with precipitation fraction (Fig 3.7(d)). The similar dependency of $f_c$ and $f_p$ as $E_{auto}$ and $E_{accr}$ indicates that if $f_c$ and $f_p$ are given to Eqs. (3.15) and (3.18) to calculate enhancement factors based on the PDF model, the resulting $E_{auto}$

and $E_{accr}$ will have the same dependency on precipitation fraction as the unbiased values shown here. Meanwhile, the magnitude of the change is also well captured. The magnitude and position of the peak in enhancement factors (with respect to precipitation fraction) do change with the threshold used to define when precipitation is present. When the threshold of -25 dBZ (-15 dBZ) is used, the mean of $f_c$, $f_p$, $E_{auto}$ and $E_{accr}$ peak when precipitation fraction is between 0.6 (0.2) and 0.8 (0.4). Furthermore, when grid size increases (100 km), the peak of the $E_{auto}$ and $E_{accr}$ tend to shift to the smaller precipitation fraction. However, the change of $\rho$ on precipitation fraction remains small regardless of grid size and threshold applied.

On a minor note, B2014 didn't examine the dependence of the correlation coefficient with precipitation fraction, but L2013 using a combination of satellite retrieved precipitation from CloudSat (radar) and MODIS cloud liquid water path (visible-shortwave infrared) suggested that the mean value of $\rho$ did not exhibit any dependence with precipitation fraction for shallow marine boundary layer clouds. While there are concerns about the ability of CloudSat to detect precipitation from shallow clouds (with cloud bases below 1 km), our results for ENA nonetheless support the idea that there is little dependence in the correlation coefficient with precipitation fraction.

### 3.3.4 *Vertical Dependence*

We investigate the vertical dependence of autoconversion and accretion enhancement factors by mapping the ground-based radar retrievals according to their height relative to the cloud boundaries, such that a relative height of 0 indicates cloud base and 1 indicates cloud top. Fig 3.8 shows the results for $E_{auto}$ (a), $E_{accr}$ (b), $f_p$ (c) and $\rho$ (d) using box-and-whisker plots at six relative height levels in cloud. The values shown here are specific to a grid size of 50 km.

However, the relative values at all height bins behave qualitatively similarly at all scales, with larger grid scales having larger values (enhancement factors) consistent with the results discussed in section 3.2 based on the layer-mean mixing ratios. In each subplot, mean values are denoted by the red stars, while the mean values for thin clouds are denoted by the blue dots and thick clouds by the red dots. Thin clouds are those with a mean cloud thickness (from the combination cloud radar and lidar) smaller than 300 m (averaged over the 50 km grid scale), and thick clouds are those thicker than 300 m.

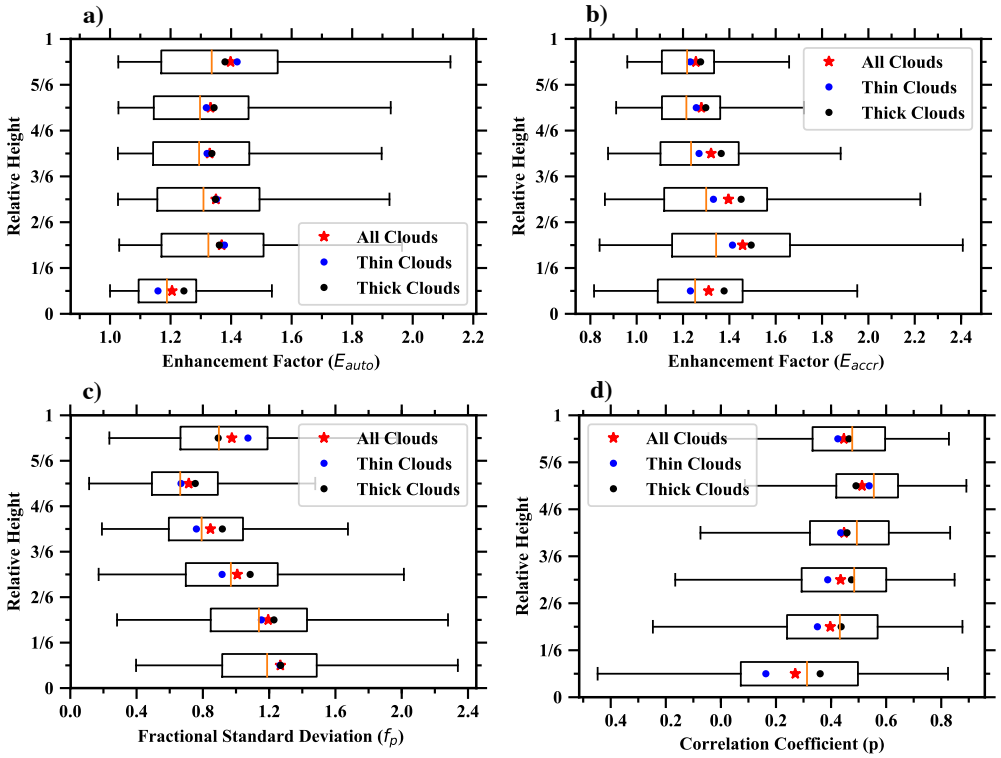


*Figure 3.8 Box and whisker plots of $E_{auto}$ (a), $E_{accr}$ (b), $f_p$ (c) and ρ (d) at different height for all clouds (considering both thick and thin clouds) with mean values of all clouds (red star), thin clouds (blue dot) and thick cloud (black dot). A relative height of 0 represents cloud base and 1 represents cloud top.*

Fig 3.8(a) shows that the mean value of $E_{auto}$ (red star) and $f_c$ (not shown) does not change much with altitude and between thin and thick clouds. We stress the underlying radar retrieval assumes that the CLWC increases linearly with height in the cloud (on the time scale of a few seconds and equivalent horizontal scale below 100 m), and therefore one might not expect to see much vertical dependence as a consequence of this assumption. In general, aircraft studies for stratocumulus do typically show that the mean vertical profile is linear, except at times close to cloud top where entrainment can be significant. In Fig 3.8(b), the mean value of $E_{accr}$ depends modestly on the vertical position, increasing from 1.31 at the bottom to peak near 1.46 in the bottom third of the cloud, and then steadily decreasing to 1.26 at the top - a variation of about 16%. Meanwhile, $f_p$ decreases (Fig 3.8(c)) and $\rho$ increases (Fig 3.8(d)) from cloud base toward cloud top exerting offsetting effects on the variation of $E_{accr}$. The vertical change of $E_{auto}$, $E_{accr}$, $f_p$ and $\rho$ are consistent in different grid sizes only scaling accordingly as a manner demonstrated in section 3.3.2 and $E_{accr}$ having larger variations when grid size is larger. The vertical dependence in $E_{auto}$ and $E_{accr}$ suggests that one might choose to ignore the vertical dependence in the parameterizations of $E_{auto}$ in models or perhaps focus on layer-mean mixing-ratio as inputs to model parameterization but not for $E_{accr}$. The potential impacts of vertical dependence may also be needed when using in situ aircraft data, since aircraft do not measure layer-mean quantities and likewise if model parameterization are used to predict $f_c$, $f_p$ and $\rho$ rather than $E_{auto}$ and $E_{accr}$ (as suggested by Boutle) since the values obtained for $f_p$ and $\rho$ do vary with vertical position within the cloud. Fig. 3.8 also shows there is small difference (on average) for relatively thin or thick clouds. We will investigate and discuss the dependency of $E_{auto}$ and $E_{accr}$ on cloud thickness further in section 3.3.6.

### 3.3.5 *Correlation with Surface Relative Humidity and Lower Tropospheric Stability*

Fig 3.9 illustrates how $E_{auto}$ (left panels) and $E_{accr}$ (right panels) change with surface relative humidity (RH; upper panels) and lower tropospheric stability (LTS; bottom panels). LTS is defined as the difference in the potential temperature between 700 hPa and the surface [Klein and Hartmann, 1993] and is a measure of the strength of the boundary layer inversion [Wood, 2012]. Surface RH and LTS have been found to correlate with fractional cloud cover in marine Sc, as well cloud base height, cloud top height, and cloud thickness [Klein and Hartmann, 1993; Wood and Hartmann, 2006; Eastman et al., 2011, Naud et al. 2018].

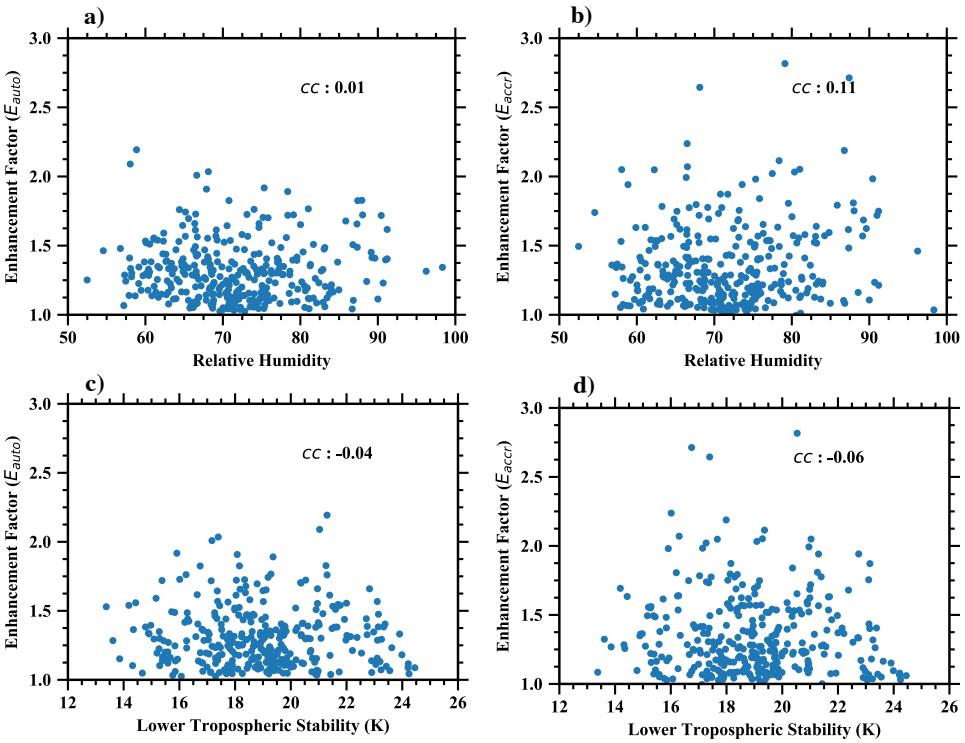


*Figure 3.9 Scatter plot of surface relative humidity versus $E_{auto}$ (a) and $E_{accr}$ (b) with correlation coefficient (cc) shown. (c) and (d) are counterparts for lower tropospheric stability.*

A relationship between the enhancement factors and surface RH or LTS would likely be easy to implement in large scales models. However, our results show there is little if any correlation between $E_{auto}$ and $E_{accr}$ and either surface RH or LTS. The correlation coefficient between $E_{auto}$ and $E_{accr}$ and surface RH is 0.01 and 0.11, respectively, while for LTS, the value is 0.05 for both enhancement factors. The results shown in Fig. 3.9 (and these specific values) are for a grid size of 50 km, and correlations coefficient at other grid sizes are equally small. We also investigated using the estimated inversion strength (EIS) [Wood and Bretherton 2006], rather than LTS as a measure of stability index with essentially the same result. We note, however, that all the cases examined here are single-layered and near overcast and in boundary layers with LTS values between 14 and 24 K, and our results do not extend beyond stratocumulus.

### 3.3.6 *Correlation with Liquid Water Path and Cloud Thickness*

The change of $E_{auto}$ and $E_{accr}$ with in-cloud TLWP (PLWC below cloud base is excluded) is explored in the scatter plots in the upper panels of Fig 3.10. As in the previous section, results are shown here a grid size of 50 km, and qualitatively similar results are obtained at all grid sizes. As is typical for Sc, the LWP is often in the range of 25 and 250 g/m2. An analysis by W2018 found the mean value of $E_{auto}$ and $E_{accr}$ was larger when LWP is greater than 75 g/m2. In our case study example (section 3.1) a cloud segment with larger LWP had larger enhancement factor than the nearby segment with a smaller LWP. Likewise in our analysis of vertical dependence in Fig. 3.8 we found that "on average" thicker clouds (which general have higher LWP) had a slightly larger $E_{accr}$ than thinner clouds. However, Fig 3.10(a) shows basically no correlation between $E_{auto}$ and the grid-mean in-cloud LWP, and for $E_{accr}$, this is only a very weak correlation of 0.13.

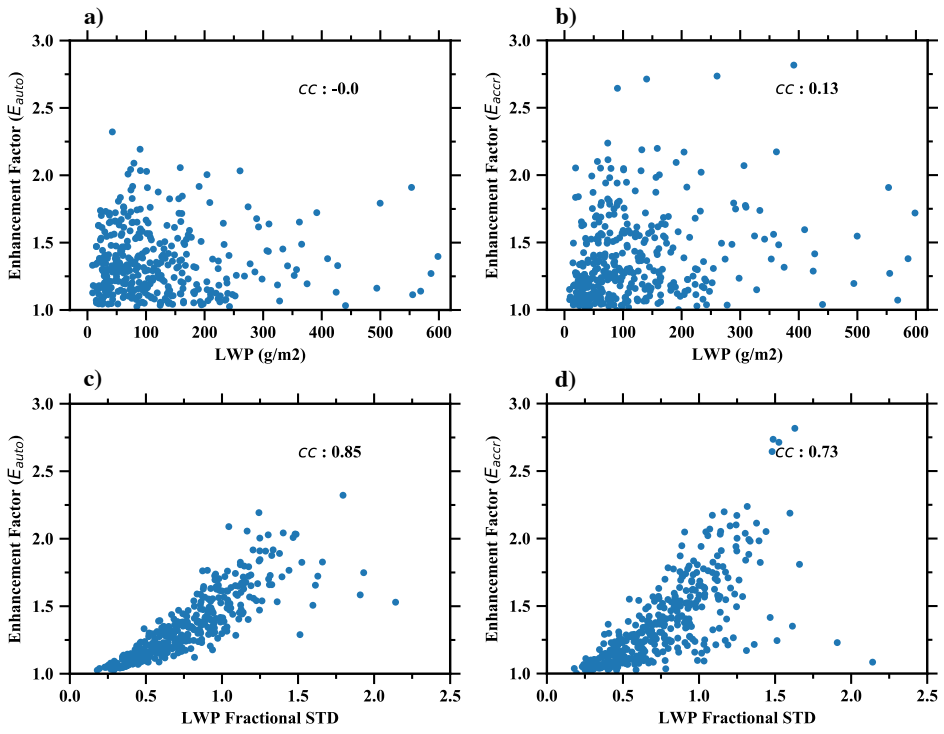


*Figure 3.10 Scatter plot of LWP versus $E_{auto}$ (a) and $E_{accr}$ (b) with correlation coefficient (cc) shown. (c) and (d) are counterparts for fractional standard deviation of LWP.*

On the other hand, we do find that the fractional standard deviation of LWP (given by the standard deviation of the LWP divided by the mean, following Eq. 3.3) is strongly correlated with $E_{auto}$ and $E_{accr}$ as shown in Fig 3.10(c) and Fig 3.10(d). The correlation coefficients are 0.85 and 0.73, respectively. This result should be expected since there is little vertical dependence in $E_{auto}$ and variability in the layer-mean $q_c$ is directly related to variability in LWP and cloud thickness. To a lesser degree, larger LWP is also associated with stronger updrafts and greater formation of precipitation such that one expects LWP will also be correlated with the layer-mean $q_p$, and consequently $E_{accr}$ (which depends on both $f_c$ and $f_p$) is significantly correlated with the fractional standard deviation of LWP.

Not surprisingly, a similar situation exists for cloud thickness, as illustrated in Fig 3.11. The top panels show that there is little (if any) correlation between cloud thickness and $E_{auto}$ or $E_{accr}$ (correlation coefficients are smaller than 0.1). Thicker clouds do have a slightly larger $E_{accr}$. $E_{accr}$ in thin clouds is 1.37 and is 1.42 in thick clouds, but cloud thickness would seem to have little predicative power as regards either enhancement factor (which is largely consistent with there being little vertical dependence) and this is true for both mean cloud base height and cloud top height (the cloud top height can be an indicator of boundary layer depth). Like the situation with LWP, $E_{auto}$ and $E_{accr}$ both have strong correlations with the fractional cloud thickness as shown in the bottom panels of Fig 3.11. The correlation coefficient is 0.79 for $E_{auto}$ and 0.63 for $E_{accr}$, which are slightly smaller than counterparts of LWP. Variations in cloud base height (Fig 3.12) are important here, but correlation coefficients are smaller (0.38 and 0.36, respectively), showing that variations in cloud top height are also important. Overall, these results indicate that almost any information of subgrid variability might be useful in further constraining (or parameterizing) the enhancement factors, while grid mean properties are generally weak indicators.

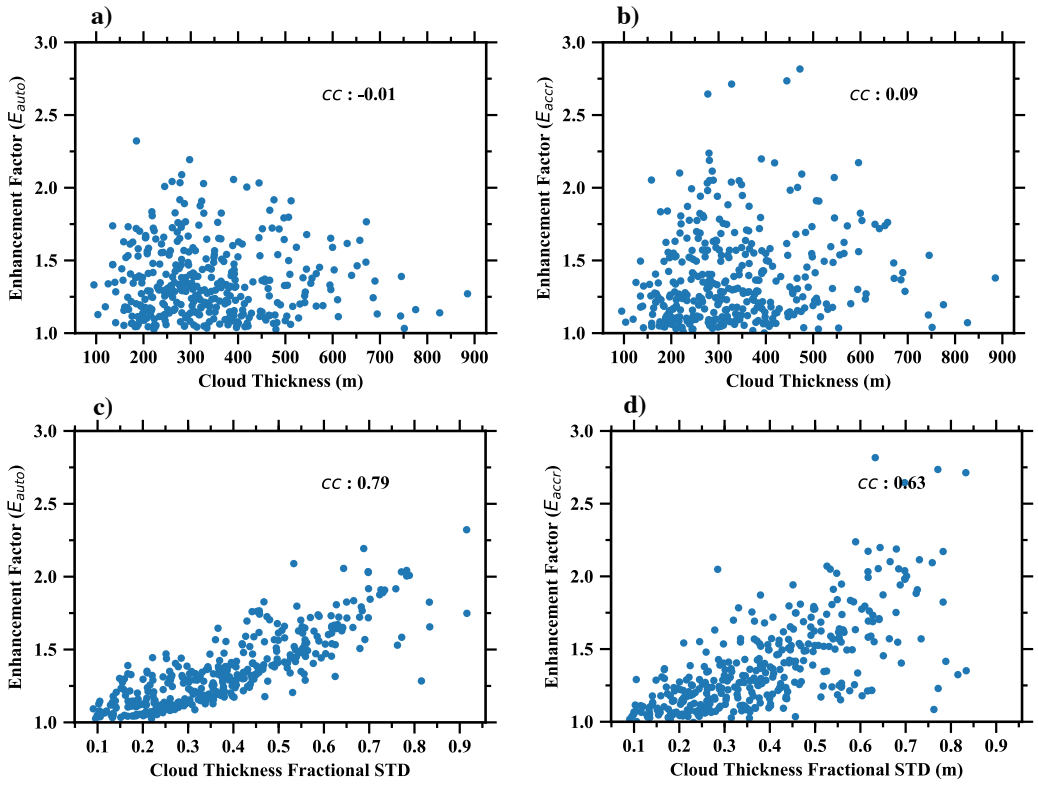


*Figure 3.11 Same as Figure 3.10 but for cloud thickness*

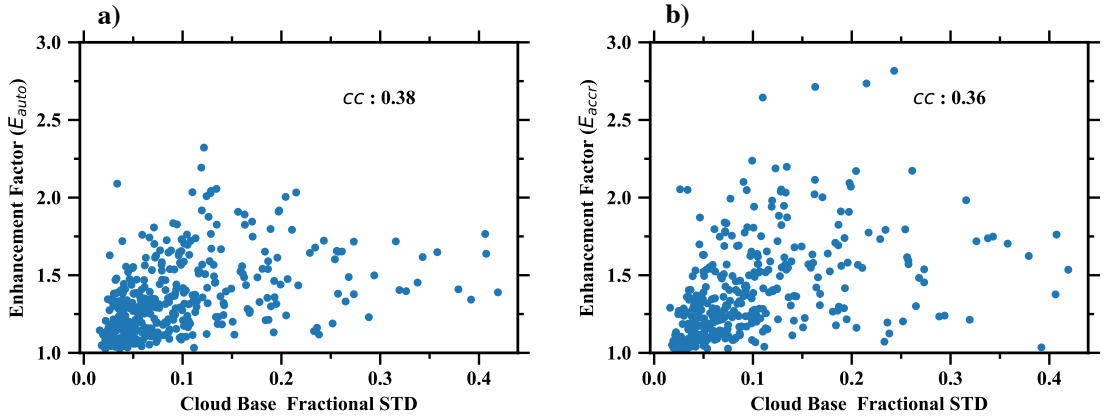


*Figure 3.12 Scatter plot of fractional standard deviation of cloud base versus $E_{auto}$ (a) and $E_{accr}$ (b) with correlation coefficient (cc) shown.*

## 3.4 Conclusions

Autoconversion and accretion are processes that are of critical importance in the modeling of precipitation. In bulk microphysics schemes, the process rates for both autoconversion and accretion are typically parameterized using nonlinear power law relationships of the cloud and precipitation mixing ratio ($q_c$ and $q_p$, respectively, see Eqs. 3.1 and 3.2). There is a considerable spatial variability in these mixing ratios on scales well below what is resolved in climate models as discussed in section 3.1. This subgrid variability combined with the nonlinear nature of the processes rates means that one cannot simply use the grid-mean mixing ratios to obtain the correct grid-mean process rate. Simply using the grid-mean mixing ratios will lead to underestimation of the process rates. Typically, the effect of subgrid variability is incorporated in climate models (and other models with grid-scales that are more than a few kilometers) by multiplying the processes rates calculated using the grid-mean mixing ratios by an enhancement factor which is derived by integrating the process rate over an assumed bivariate lognormal distribution for the mixing ratios.

In this study, we derived and analyzed enhancement factors for marine Sc (see criteria in section 3.2) observed at the ARM program site in the Eastern North Atlantic based on retrieved cloud and precipitation mixing ratios from a combination of radar Doppler Spectra, ceilometer cloud base, passive microwave radiometer retrievals of LWP and radiosonde data following observational studies by Wood et al. [2002], B2014, L2013, and W2018. Consistent with these previous studies, we find that both $E_{auto}$ and $E_{accr}$ have a significant scale dependency and they increase with the constants in Eqs. 3.1 and 3.2 (i.e. $b_{au}$, $b_{acc}$ and $b_{acp}$) as larger values indicate more nonlinearilty. $E_{auto}$ and $E_{accr}$ increase relatively quickly as grid-size increases from 5 to

100 km and more slowly between 100 and 200 km since much of the variability has been incorporated in the first 100 km. B2014 investigated the scale dependency of $f_c$ and $f_p$ up to 100 km and found a similar trend but the actual magnitude of $f_c$ and $f_p$ are smaller than what we have found here. The reason is probably due to the fact that B2014 applied thresholds to filter out smaller values of $q_c$ and $q_p$. However, despite of demonstrating a similar scale dependence, $E_{auto}$ and $E_{accr}$ calculated by W2018 are larger than the values found here in all grid sizes. For example, at the grid size of 30 (180) km, W2018 found the mean of $E_{auto}$ and $E_{accr}$ to be 1.96 (3.20) and 1.53 (1.72), respectively compared to the corresponding values of 1.36 (1.49) and 1.4 (1.66) found here for the grid size of 50 (200) km. The main reason is that the retrieval of $q_c$ (CLWC) and $q_p$ (PLWC) in W2018 is quite different from that used here. In W2018, when the reflectivity at cloud base is smaller than -37 dBZ, CLWC for the whole vertical profile was retrieved assuming CLWC is proportional to radar reflectivity with cloud particles number concentration (N) calculated from parameterizations [Dong et al., 2014]. The same approach was used to calculate CLWC at one range gate above the cloud base by assuming the reflectivity due to CLWC equals the difference between total reflectivity and the reflectivity at cloud base. When the reflectivity at cloud base is larger than -37 dBZ, the adiabatic model of CLWC was used but instead of accounting for the subadiabaticity using adiabatic factors based on LWP from microwave radiometers or some statistical constant values as described in Chapter 2, they calculated the adiabatic factors using the aforementioned CLWC at one range gate above the cloud base. It is hard to say which approach is better (detailed comparisons are needed) but it is likely that the adiabatic factors may lead the differences in $E_{auto}$. The retrieved CLWC was then used to calculate reflectivity due to cloud droplets which was subsequently subtracted from total reflectivity to retrieve reflectivity contributed by precipitation. The reflectivity and two other

parameters (shape parameter, normalized rain droplet number concentration of the rain particle size distribution) which were obtained from below cloud base using methods described in O'Connor et al. [2005] were used to estimate PLWC in W2018. Both approaches have large uncertainties. In our case, we use derived power law equations to calculate PLWC based on total reflectivity meaning that for given reflectivity and the relative position in cloud, only one value of PLWC is calculated. This will likely underestimate the subgrid variability of $q_p$ and further research is needed to investigate the effect of uncertainties. L2013 did not examine scale dependency but showed the mean of $E_{auto}$ and $E_{accr}$ at a grid size of 141 km is 2.29 and 1.60, respectively. Their reported $E_{auto}$ is larger than what we found but smaller compared to W2018 (3.18 at a grid size of 150 km). However, the results are hard to compare as L2013 compiled the data based on Sc globally.

Our results also indicate that $E_{auto}$ and $E_{accr}$ have some dependency on precipitation fraction. $E_{auto}$ and $E_{accr}$ reach their maximum when precipitation fraction is between 0.4 and 0.6 at a grid size of 50 km if a threshold of -20 dBZ at cloud base is used to define precipitation occurrence. The precipitation fraction at which $E_{auto}$ and $E_{accr}$ reach their maximum may change with grid size with the maximum tends to move toward to smaller precipitation fraction in larger scales. The location of the maximum is also sensitive to the threshold with larger reflectivity thresholds pushing the maximum to lower precipitation occurrences (see section 3.3.3). This is at least qualitatively similar to B2014 who used the threshold of 0.001 g/kg in $q_p$ to define precipitation present using aircraft observations, although they did not include smaller values of $q_p$ when calculating $f_p$. They found that mean $f_p$was largest when precipitation fraction is around 0.2. These results support the idea of using precipitation fraction to parameterize enhancement factors.

In regard to find other quantities that might be useful in parameterizing the enhancement factors, we examine the dependency of $E_{auto}$ and $E_{accr}$ on surface RH, LTS, grid-mean LWP and grid-mean cloud thickness. Unfortunately, we found little if any correlations between enhancement factors (or $f_c, f_p, \rho$) to these variables suggesting that grid mean properties which are relatively easy to obtain in the model are weak indicators to parameter the enhancement factors – at least when restricted to marine Sc. Not surprisingly, $E_{auto}$ and $E_{accr}$ are strongly correlated with variations of LWP, cloud thickness and cloud base height which suggests that any information on subgrid variability (of at least cloud properties) might prove useful in parameterization efforts.

Perhaps the most unique aspect of the present work is a more thorough examination of vertical variations of $E_{auto}$ and $E_{accr}$. At the outset of this study, we reasoned that if $f_p$ and $\rho$ were important to enhancement factors in accretion (based on Eq. 3.17) then one should expect a significant vertical dependence in the enhancement factors since precipitation variability is (we expected) larger near cloud base than cloud top. Indeed, we found $E_{accr}$ generally decreases from cloud base to cloud top although there is a cancellation of effects, with the increase in subgrid variability of precipitation near the lower in the cloud offset by a decrease in the correlation coefficient between cloud and precipitation water maxing ratio. But $E_{auto}$ stays relatively unchanged vertically which is expected as we assume CLWC increases linearly in the cloud. The result indicates that at least for single-layered near overcast stratocumulus as studied here one cannot likely parameterize $E_{accr}$ directly without having to account for vertical variations the subgrid variability cloud, precipitation, and their correlation. Meanwhile, care should probably be taken to recognize that vertical variations in cloud and precipitation may

impact parameterization of $f_p$ and $\rho$ based on in situ observations or other remote sensing retrievals.

In most of our analysis we focused on examining unbiased enhancement factors, mean enhancement factors calculated directly using the mean of local microphysical rates divided by the microphysical rates computed using the domain-mean value for $q_c$ and $q_p$ rather than relying on an analytical approximation based on an assumed subgrid distribution. We did, however, evaluate such a PDF approach using an assumed bivariate lognormal distribution following B2014. Overall we find while our retrieval mixing ratios are not exactly lognormally distributed, they are sufficiently close to lognormal bivariate lognormal models, and in general that if one has good estimate of $f_c$, $f_p$ and $\rho$ the analytical framework works well. We also find that estimating the values of $f_c$, $f_p$ and $\rho$ using the Method-of-Moments approach work better with this framework than estimates based on a Maximum-Likehood approach.

The Morrison and Gettelman [2008] two-moment bulk microphysics scheme (which is implemented in the NCAR Community Atmospheric Model and DOE E3SM among other climate models) includes enhancement factors for both autoconversion and accretion due to subgrid variability in cloud liquid water but does not consider subgrid variability in precipitation (or correlation between cloud and precipitation). In this scheme, $E_{auto}$ is set to 3.2 which is much larger than the values we find which are less about 1.5 (out of a 200 km grid scale), while MG2008 prescribed a value of 1.07 for $E_{accr}$ which is too small (based our analysis), though this is not surprising given that it does not include subgrid variability in precipitation (nor consider the correlation of cloud and precipitation). We find that $f_p$ actually is larger than $f_c$, which was also reported in Wood [2005a] and B2014, and likewise find that including $\rho$ in the formulation

for $E_{accr}$ is important. A PDF of $\rho$ based on layer-mean mixing ratios for all the cases at a grid size of 50 km is shown in Fig 3.13. The majority of values are between 0.2 and 0.8 although occasionally is near or even smaller than 0. The mean and median value are 0.53 and 0.57, respectively, which are very close to the value of 0.44 and 0.58 reported by L2013 using MODIS and CloudSat observations for marine stratocumulus, globally. B2014 reported a somewhat smaller mean value of 0.2 based on aircraft observations of the VOCALS-REx field campaign which focused on the Sc in southeast pacific (though we caution here this value is likely to vary with vertical position within cloud when using aircraft observations). Although these numbers are hard to compare since data came from different sources and locations, they all suggest that covariability of $q_c$ and $q_p$ should not be ignored.

In general, we want to emphasize that all the analysis presented here is limited to single-layered near overcast Sc, and does not include (trade) cumulus or deep convection. For example, all our Sc cases had an LTS of 14 K or larger, and this may explain why no correlation was found between enhancement factors and LTS. Enhancement factors have been found to be regime dependent by B2014 and Zhang et al. [2019] with subgrid variability increasing as cloud fraction decreases (going from overcast stratocumulus to broken stratocumulus to scattered cumulus). We also note that we have not considered the impact of subgrid variability in cloud droplet number concentration. Zhang et al. [2019] suggested subgrid variability of droplet number concentration (N) and its covariability with $q_c$ are important, and further research on this topic is needed.

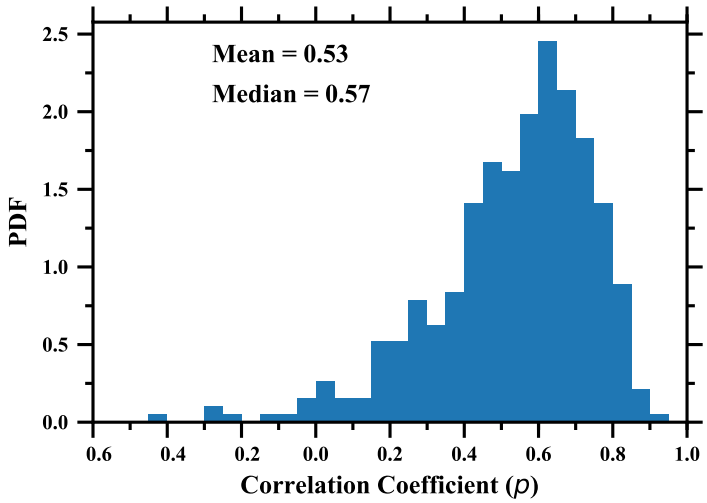


*Figure 3.13 Distribution of correlation coefficient (ρ) between $q_c$ and $q_p$ for each grid size of 50 km. The mean and median value are shown in the plot.*

# Chapter 4.

# Conclusions

CLWC and PLWC are two key properties in marine Sc which play a critical role in the aerosol-cloud-precipitation-radiation interactions. They are also directly involved in the parameterization of autoconversion and accretion rates in GCMs. However, the jointly retrieval of CLWC and PLWC is limited. This dissertation retrieves CLWC and PLWC simultaneously using ground-based observations and studies effects of their subgrid variability on autoconversion and accretion rates.

In Chapter 2, measurements in the ARM ENA site are used to retrieve CLWC and PLWC, such as the reflectivity factor, mean Doppler velocity, spectral width and Doppler spectra from a vertically pointing Ka-band cloud radar, TLWP from a three-channel MWR and radiosonde measurements. The core of the retrieval algorithm for PLWC is to separate the Doppler spectrum at each range gate into cloud and precipitation components allowing reflectivity, Doppler velocity and spectral width associated with each component be derived and used to calculate PLWC based on the theory developed by Frisch et al. [1995]. It turns out only less than 20% of the radar volumes exhibit a distinct bimodal distribution which can be separated. Power law equations thus are fitted on the case-by-case basis between total reflectivity and PLWC for bottom, middle and top third of the clouds, respectively, from the separable points. These equations are applied to radar volumes where Doppler spectra are non-separable to retrieve PLWC. Following Orr and Kropfli [1999], a power law equation between total reflectivity and drizzle fall velocity is derived assuming air velocity will average to zero on the scale of one day.

This equation is then applied to calculate PLWC below cloud based on Frisch et al. [1995]. For CLWC, when TLWP from the MWR is available (The dome of MWR is not wet), it is calculated directly by linearly distributing TLWP from cloud base to top. Otherwise, an adiabatic cloud model is used but the values are adjusted by an empirical adiabatic factor. Comparisons with aircraft observations for two example cases demonstrates that the retrieval algorithm works reasonably well. The detailed uncertainties of the retrievals are given in Chapter 2. On the scale of one day, the systematic error in the mean PLWC is estimated to be less than 75% though for a single radar volume, the uncertainty can be one order of magnitude. The uncertainty in the mean CLWC is expected to be within 30%

In Chapter 3, the CLWC and PLWC retrieved for single-layered overcast marine Sc are converted to $q_c$ and $q_p$ and the effect of their subgrid variability on autoconversion and accretion rates is studied by analyzing enhancement factors. Following Lebsock et al. [2013] and Boutle et al. [2014], the enhancement factor for autoconversion rate ($E_{auto}$) and accretion rate ($E_{accr}$) are derived by integrating the process rate over an assumed spatial mixing ratio distribution and dividing the result by the process rate calculated in terms of grid-mean $q_c$ and $q_p$. Consistent with previous studies, I find that $E_{auto}$ and $E_{accr}$ increase relatively quickly with grid size when grid size is below 100 km and slowly when grid size is between 100 and 200 km. The mean of $E_{auto}$ ($E_{accr}$) at grid size of 200 km is 1.49 (1.66) which is much smaller (larger) than the fixed value of 3.2 (1.07) used in the Morrison and Gettelman [2008] two-moment scheme. This may explain why GCMs produce precipitation too frequently but too lightly as the autoconversion rate is overestimated and accretion rate is underestimated. Meanwhile, $E_{auto}$ and $E_{accr}$ are function of precipitation fraction as previous studies indicate, and reach their maximum when fraction is in the range of 0.4 and 0.6, though the location of the maximum will change based on

grid size and the threshold used to define precipitation. The correlation of $q_c$ and $q_p$ ($\rho$), however, does not have dependency on grid size and precipitation fraction which could simplify the parameterization of $E_{accr}$. Vertical variation of $E_{auto}$ is weak due to the assumption made in the retrievals that CLWC increases linearly in the cloud. However, for $E_{accr}$, it generally decreases from cloud base to cloud top despite of the cancelling effect of an increase in correlation of $q_c$ and $q_p$ and a decrease in the magnitude of the subgrid variability of $q_p$.

Further analysis indicates that $E_{auto}$ and $E_{accr}$ have little if any correlations with relative humidity, lower tropospheric stability, liquid water path, cloud thickness but they are highly correlation with the variation of liquid water path, cloud thickness and cloud base indicating almost any knowledge of subgrid variability could be useful in further constraining the enhancement factors.

# VITA

Wei Zhao comes from Henan province which is the biggest agricultural province in China. Sitting in front of the television and watching the national weather forecast was a daily routine since the forecast would guide his parents what to do in the next a few days. Driven by his curiosity of weather and climate, he went to Lanzhou University and obtained his Bachelor's degree in Atmospheric Sciences in 2013. His journey went on as he joined the Department of Atmospheric Sciences at the University of Washington in 2014 and was advised by Prof. Roger Marchand and Prof. Qiang Fu. After six years of great time in the Department, he finished his Ph.D. in June, 2020.

# REFERENCES


Ackerman, A.S., M.C. vanZanten, B. Stevens, et al. (2009). Large-eddy simulations of a drizzling, stratocumulus-topped marine boundary layer. *Mon. Weather Rev.*, **137**, 1083-1110. https://doi.org/10.1175/2008MWR2582.1.

Ahlgrimm, M., and R. M. Forbes. (2016). Regime dependence of cloud condensate variability observed at the Atmospheric Radiation Measurement Sites. *Quart. J. Roy. Meteor. Soc.*, **142,** 1605-1617. https://doi.org/10.1002/qj.2783.

Albrecht, B. A. (1989). Aerosols, cloud microphysics, and fractional cloudiness. *Science*, **245**, 1227-1230. doi:https://doi.org/10.1126/science.245.4923.1227.

Albrecht, B. A., R. P. Penc, and W. H. Schubert. (1985). An observational study of cloud-topped mixed layer. *J. Atmos. Sci.*, **42**, 800-822. https://doi.org/10.1175/1520-0469(1985)042<0800:AOSOCT> 2.0.CO;2.

Atlas, D. (1954). The estimation of cloud parameters by radars. *J. Meteor.*, **11**, 309-317. https://doi.org/10.1175/1520-0469(1954)011<0309:TEOCPB>2.0.CO;2.

Austin, P., Y. Wang, V. Kujala, et al. (1995). Precipitation in stratocumulus clouds: Observational and modeling results. *J. Atmos. Sci.*, **52**, 2329-2352. https://doi.org/10.1175/1520-0469(1995)052<2329:PISCOA>2.0.CO;2.

Babb, D.M., J. Verlinde, and B.A. Albrecht. (1999). Retrieval of Cloud Microphysical Parameters from 94-GHz Radar Doppler Power Spectra. *J. Atmos. Oceanic Technol.,* **16**, 489-503. https://doi.org/10.1175/1520-0426(1999)016<0489:ROCMPF>2.0.CO;2.

Baedi, R., R. Boers, and H. Russchenberg. (2002). Detection of boundary layer water clouds by spaceborne cloud radar. *J. Atmos. Oceanic Technol.*, **19**, 1915-1927. https://doi.org/10.1175/1520-0426(2002)019<1915:DOBLWC>2.0.CO;2.

Barker, H. W., B. A. Wiellicki, and L. Parker. (1996). A parameterization for computing grid-averaged solar fluxes for inhomogeneous marine boundary layer clouds. Part II: Validation using satellite data. *J. Atmos. Sci.*, **53**, 2304-2316. https://doi.org/10.1175/1520-0469(1996)053<2304:APFCGA>2.0.CO;2.

Beheng, K. D. (1994). A parameterization of warm cloud microphysical conversion processes. *J. Atmos. Res.*, **33**, 193-206. https://doi.org/10.1016/0169-8095(94)90020-5.

Bender, F.A., A. Engström, and J. Karlsson. (2016). Factors Controlling Cloud Albedo in Marine Subtropical Stratocumulus Regions in Climate Models and Satellite Observations. *J. Clim.*, **29,** 3559-3587. https://doi.org/10.1175/JCLI-D-15-0095.1.

Berry, E. X. (1968). Modification of the warm rain process. Proc. First Conf. on Weather Modification, American Meteorological Society, pp81-85.

Boers, R., H. Russchenberg, J. S. Erkelens, et al. (2000). Ground-based remote sensing of stratocumulus properties during CLARA-1996. *J. Appl. Meteorol.*, **39**, 169-181. https://doi.org/10.1175/1520-0450(2000)039<0169:GBRSOS>2.0.CO;2.

Boutle, I. A., S. J. Abel, P. G. Hill, et al. (2014). Spatial variability of liquid cloud and rain: Observations and microphysical effects. *Quart. J. Roy. Meteor. Soc.*, **140**, 583-594. https://doi.org/10.1002/qj.2140.

Braun, R. A., Dadashazar, H., Macdonald, A. B., et al. (2018). Cloud adiabaticity and its relationship to marine stratocumulus characteristics over the northeast Pacific Ocean. *J. Geophys. Res. Atmos.*, **123**, 13790–13806. https://doi.org/10.1029/2018jd029287

Bretherton, C., J. McCaa, and H. Grenier. (2004). A new parameterization for shallow cumulus convection and its application to marine subtropical cloud-topped boundary layers. Part I: Description and 1D results. *Mon. Weather Rev.*, **132**, 864-882. https://doi.org/10.1175/1520-0493(2004)132<0864:ANPFSC>2.0.CO;2.

Cadeddu, M. P., D. D. Turner, and J. C. Liljegren. (2009). A neural network for real-time retrievals of PWV and LWP from Arctic millimeter-wave ground-based observations. *IEEE Trans. Geosci. Remote Sens.*, **47**, 1887-1900. doi: 10.1109/TGRS.2009.2013205.

Cadeddu, M. P., J. C. Liljegren, and D. D. Turner. (2013). The Atmospheric Radiation Measurement (ARM) program network of microwave radiometers: Instrumentation, data and retrievals. *Atmos. Meas. Tech.*, **6**, 2359-2372. doi:10.5194/amt-6-2359-2013.

Chandra, A., C. Zhang, P. Kollias, et al. (2015). Automated rain rate estimates using the Ka-band ARM zenith radar (KAZR). *Atmos. Meas. Tech.*, **8**, 3685-3699. doi:10.5194/amt-8-3685-2015.

Chen, T., W. B. Rossow, and Y. Zhang. (2000). Radiative effects of cloud-type variations. *J. Clim.*, **13**, 264-286. https://doi.org/10.1175/1520-0442(2000)013<0264:REOCTV>2.0.CO;2.

Chen, D., and A. Dai. (2019). Precipitation characteristics in the Community Atmosphere Model and their dependence on model physics and resolution. *J. Adv. Model. Earth Syst.*, **11**, 2352-2374. https://doi.org/10.1029/2018MS001536.

Chin, H. N. S., D. J. Rodriguez, R. T. Cederwall, et al. (2000). A microphysical retrieval scheme for continental low-level stratiform clouds: Impacts of the sub-adiabatic character on microphysical properties and radiation budgets. *Mon. Wea. Rev.*, **128**, 2511-2527. https://doi.org/10.1175/1520-0493(2000)128<2511:AMRSFC>2.0.CO;2.

Christensen, M. W., G. L. Stephens, and M, D, Lebsock. (2013). Exposing biases in retrieved low cloud properties from CloudSat: a guide for evaluating observations and climate data. *J. Geophys. Res. Atmos.*, **118**, 12120-12131. doi:10.1002/2013jd020224.

Clement, A. C., R. Burgman, and J. R. Norris. (2009). Observational and model evidence for positive low-level cloud feedback. *Science*, **325**, 460-464. doi:10.1126/science.1171255.

Clothiaux, E. E., T. P. Ackerman, G. G. Mace, et al. (2000). Objective determination of cloud heights and radar reflectivities using a combination of active remote sensors at the ARM CART

sites. *J. Appl. Meteorol.*, **39**, 645-665. https://doi.org/10.1175/1520-0450(2000)039<0645:ODOCHA>2.0.CO;2.

Comstock, K. K., R. Wood, S. E. Yuter, et al. (2004). Reflectivity and rain rate in and below drizzling stratocumulus. *Quart. J. Roy. Meteor. Soc.*, **130**, 2891-2918. https://doi.org/10.1256/qj.03.187.

Comstock, K. K., C. S. Bretherton, and S. E. Yuter. (2005). Mesoscale variability and drizzle in southeast Pacific stratocumulus. *J. Atmos. Sci.*, **62**, 3792-3807. https://doi.org/10.1175/JAS3567.1.

Crease, B. A., and A. Slingo (1982). A field study of nocturnal stratocumulus: I. Mean structure and budgets. *Quart. J. Roy. Meteor. Soc.*, **108**, 103-123. https://doi.org/10.1002/qj.49710845507.

Dai, A. (2006). Precipitation characteristics in eighteen coupled climate models. *J. Clim.*, **19**, 4605-4630. https://doi.org/10.1175/JCLI3884.1.

Donat, M. G., A. L. Lowry, L. V. Alexander, et al. (2016). More extreme precipitation in the world's dry and wet regions. *Nat. Clim. Chang.*, **6**, 508-513. https://doi.org/10.1038/nclimate2941.

Dong, X., B. Xi, A. Kennedy, et al. (2014). A 19-month record of marine aerosol-cloud-radiation properties derived from DOE arm mobile facility deployment at the Azores. Part I: cloud fraction and single-layered MBL cloud properties. *J. Clim.*, **27**, 3665-3682. https://doi.org/10.1175/JCLI-D-13-00553.1.

Dzambo, A. M., T. L'Ecuyer, O. O. Sy, et al. (2019). The Observed Structure and Precipitation Characteristics of Southeast Atlantic Stratocumulus from Airborne Radar during ORACLES 2016-17. *J. Appl. Meteorol. Climatol.*, **58**, 2197-2215. https://doi.org/10.1175/JAMC-D-19-0032.1.

Eastman, R., S. G. Warren, and C. J. Hahn. (2011). Variations in cloud cover and cloud types over the ocean from surface observations, 1954-2008. *J. Clim.*, **24**, 5914-5934. https://doi.org/10.1175/2011JCLI3972.1.

Eastman, R., R. Wood, and K. O. Ting. (2017). The Subtropical Stratocumulus-Topped Planetary Boundary Layer: A Climatology and the Lagrangian Evolution. *J. Atmos. Sci.,* **74**, 2633-2656. https://doi.org/10.1175/JAS-D-16-0336.1.

Fan, J., Y. Wang, D. Rosenfeld, et al. (2016). Review of Aerosol-Cloud Interactions: Mechanisms, Significance, and Challenges. *J. Atmos. Sci.,* **73**, 4221-4252. https://doi.org/10.1175/JAS-D-16-0037.1.

Fielding, M. D., J. C. Chiu, R. J. Hogan, et al. (2014). A novel ensemble method for retrieving properties of warm cloud in 3-D using ground-based scanning radar and zenith radiances. *J. Geophys. Res.*, **119**, 10,912-10,930. https://doi.org/10.1002/2014JD021742.

Frisch, A. S., C. W. Fairall, and J. B. Snider. (1995). Measurement of stratus cloud and drizzle

parameters in ASTEX with a Ka-band Doppler radar and microwave radiometer. *J. Atmos. Sci.*, **52**, 2788-2799. https://doi.org/10.1175/1520-0469(1995)052<2788:MOSCAD>2.0.CO;2.

Frisch, A. S., G. Feingold, C. W. Fairall, et al. (1998). On cloud radar and microwave radiometer measurements of stratus cloud liquid water profiles. *J. Geophys. Res.*, **103**, 23,195-23,197. doi:10.1029/98JD01827.

Fox, N., and A. Illingworth. (1997). The retrieval of stratocumulus cloud properties by ground-based cloud radar. *J. Appl. Meteorol.*, **36**, 485-492. https://doi.org/10.1175/1520-0450(1997)036<0485:TROSCP>2.0.CO;2.

Gettelman, A., H. Morrison, C. R. Terai, et al. (2013). Microphysical process rates and global aerosol-cloud interactions. *Atmos. Chem. Phys.*, **13**, 9855-9867. https://doi.org/10.5194/acp-13-9855-2013.

Gossard, E. E., J. B. Snider, E. E. Clothiaux, et al. (1997). The potential of 8-mm radars for remotely sensing cloud droplet size distributions. *J. Atmos. Oceanic Technol.*, **14**, 76-87. https://doi.org/10.1175/1520-0426(1997)014<0076:TPOMRF>2.0.CO;2.

Grosvenor, D., O. Sourdeval, P. Zuidema, et al. (2018). Remote sensing of droplet number concentration in warm clouds: A review of the current state of knowledge and perspectives. *Rev. Geophys.*, **56**, 409-453. https://doi.org/10.1029/2017RG000593.

Hagen, M., and S. A. Yuter. (2003). Relations between radar reflectivity, liquid-water content, and rainfall rate during the MAP SOP. *Quart. J. Roy. Meteor. Soc.*, **129**, 477-493. doi: https://doi.org/10.1256/qj.02.23.

Hahn, C. J., and S. G. Warren. (2007). A gridded climatology of clouds over land (1971-96) and ocean (1954-97) from surface observations worldwide. Oak Ridge, TN: Oak Ridge National Laboratory, Carbon Dioxide Information Analysis Center.

Hartmann, D. L., and D. Doelling. (1991). On the net radiative effectiveness of clouds. *J. Geophys. Res.*, **96**, 869-891. https://doi.org/10.1029/90JD02065.

Hartmann, D. L., M. E. Ockert-Bell, and M. L. Michelsen. (1992). The effect of cloud type on Earth's energy balance: Global analysis. *J. Clim.*, **5**, 1281-1304. https://doi.org/10.1175/1520-0442(1992)005<1281:TEOCTO>2.0.CO;2.

Hazelton, M. L. (2011). Methods of Moments Estimation. International Encyclopedia of Statistical Science. Springer Berlin Heidelberg.

Hildebrand, P. H., and R. H. Sekhon. (1974). Objective determination of the noise level in Doppler spectra. *J. Appl. Meteorol.*, **13**, 808-811. https://doi.org/10.1175/1520-0450(1974)013<0808:ODOTNL>2.0.CO;2.

Hill, P. G., C. J. Morcrette, and I. A. Boutle. (2015). A regimedependent parametrization of subgrid-scale cloud water content variability. *Quart. J. Roy. Meteor. Soc.*, **141**, 1975-1986. https://doi.org/10.1002/qj.2506.

Hogan, R. J., N. Gaussiat, and A. J. Illingworth. (2005). Stratocumulus liquid water content from dual-wavelength radar. *J. Atmos. Ocean. Tech.*, **22**, 1207-1218. doi:10.1175/Jtech1768.1.

Hogg, R.V., and E. A. Tanis. (2020). Probability and Statistical Inference, 10th Edition, Pearson.

Hudak, D., P. Rodriguez, and N. Donaldson. (2008). Validation of the CloudSat precipitation occurrence algorithm using the Canadian C band radar network. *J. Geophys. Res. Atmos.*, **113**, D00A07. https://doi.org/10.1029/2008JD009992.

Illingworth, A. J., R. J. Hogan, E. J. O'Connor, et al. (2007). CloudNet: continuous evaluation of cloud profiles in seven operational models using ground-based observations. *Bull. Am. Meteorol. Soc.,* **88**, 883-898. https://doi.org/10.1175/BAMS-88-6-883.

Jones, A., J. Haywood, and O. Boucher. (2009). Climate impacts of geoengineering marine stratocumulus clouds. *J. Geophys. Res.*, **114**, D10106. doi:10.1029/2008JD011450.

Kendon, E. J., R. A. Stratton, S. Tucker, et al. (2019). Enhanced future changes in wet and dry extremes over Africa at convection-permitting scale. *Nat. Commun.*, **10**, 1794. https://doi.org/10.1038/s41467-019-09776-9.

Kessler, E. (1969). On the distribution and continuity of water substance in atmospheric circulations. In On the distribution and continuity of water substance in atmospheric circulations. American Meteorological Society, Boston, MA, pp1-84.

Khain, A. P., K. D. Beheng, A. Heymsfield, et al. (2015). Representation of microphysical processes in cloud-resolving models: Spectral (bin) microphysics versus bulk parameterization. *Rev. Geophys.*, **53**, 247-322. https://doi.org/10.1002/2014RG000468.

Khairoutdinov, M., and Y. Kogan. (2000). A new cloud physics parameterization in a large-eddy simulation model of marine stratocumulus. *Mon. Weather Rev.*, **128**, 229-243. https://doi.org/10.1175/1520-0493(2000)128<0229:ANCPPI>2.0.CO;2.

King, N. J., K. N. Bower, J. Crosier, et al. (2013). Evaluating MODIS cloud retrievals with in situ observations from VOCALS-REx. *Atmos. Chem. Phys.*, **13**, 191-209. https://doi.org/10.1175/BAMS-88-6-883.

Klein, S. A., and D. L. Hartmann. (1993). The seasonal cycle of low stratiform clouds. *J. Clim.*, **6**, 1587-1606. https://doi.org/10.1175/1520-0442(1993)006<1587:TSCOLS>2.0.CO;2.

Kogan, Y. L. (1991). The simulation of a convective cloud in a 3-D model with explicit microphysics. Part I: Model description and sensitivity experiments. *J. Atmos. Sci.*, **48**, 1160-1189. https://doi.org/10.1175/1520-0469(1991)048<1160:TSOACC>2.0.CO;2.

Kogan, Y. L., Z. N. Kogan, and D. B. Mechem. (2007). Assessing the errors of microphysical retrievals based on Doppler radar parameters. *J. Hydrometeorol-Special Section*, **8**, 665-677. https://doi.org/10.1175/JHM603.1.

Kollias, P., B. A. Albrecht, R. Lhermitte, et al. (2001). Radar observations of updrafts, downdrafts, and turbulence in fair-weather cumuli. *J. Atmos. Sci.*, **58**, 1750-1766. doi:10.1175/1520-0469(2001)058<1750:ROOUDA>2.0.CO;2.

Kollias, P., B. A. Albrecht, and F. Marks Jr. (2002). Why Mie? Accurate observations of vertical air velocities and raindrops using a cloud radar. *Bull. Amer. Meteor. Soc.*, **83**, 1471-1483. doi:10.1175/ BAMS-83-10-1471.

Kollias, P., J. Rémillard, E. Luke, et al. (2011a). Cloud radar Doppler spectra in drizzling stratiform clouds: 1. Forward modeling and applications. *J. Geophys. Res.*, **116**, D13201. doi:10.1029/2010JD015237.

Kollias, P., W. Szyrmer, J. Rémillard, et al. (2011b). Cloud radar Doppler spectra in drizzling stratiform clouds: 2. Observations and microphysical modeling of drizzle evolution. *J. Geophys. Res.*, **116**, D13203. doi:10.1029/2010JD015238.

Kollias, P., B. Puigdomènech Treserras, and A. Protat. (2019). Calibration of the 2007-2017 record of Atmospheric Radiation Measurements cloud radar observations using CloudSat. *Atmos. Meas. Tech.*, **12**, 4949-4964. https://doi.org/10.5194/amt-12-4949-2019.

Küchler, N., S. Kneifel, P. Kollias, et al. (2018). Revisiting liquid water content retrievals in warm stratified clouds: The modified Frisch. *Geophys. Res. Lett.*, **45**, 9323-9330. https://doi.org/10.1029/2018GL079845.

Larson, V. E., R. Wood, P. R. Field, et al. (2001). Systematic biases in the microphysics and thermodynamics of numerical models that ignore subgrid-scale variability. *J. Atmos. Sci.*, **58**, 1117-1128. https://doi.org/10.1175/1520-0469(2001)058<1117:SBITMA>2.0.CO;2.

Larson, V. E., D. P. Schanen, M. Wang, et al. (2012). PDF parameterization of boundary layer clouds in models with horizontal grid spacings from 2 to 16 km. *Mon. Weather Rev.*, **140**, 285-306. https://doi.org/10.1175/MWR-D-10-05059.1.

Larson, V. E., and B. M. Griffin. (2013). Analytic upscaling of a local microphysics scheme. Part I: Derivation. *Quart. J. Roy. Meteor. Soc.*, **139**, 46-57. https://doi.org/10.1002/qj.1967.

Lee, H., and J. Baik. (2017). A Physically Based Autoconversion Parameterization. *J. Atmos. Sci.,* **74**, 1599-1616. https://doi.org/10.1175/JAS-D-16-0207.1.

Lebsock, M., H. Morrison, and A. Gettelman. (2013). Microphysical implications of cloud-precipitation covariance derived from satellite remote sensing. *J. Geophys. Res. Atmos.*, **118**, 6521-6533. https://doi.org/10.1002/jgrd.50347.

Leinonen, J., M. D. Lebsock, G. L. Stephens, et al. (2016). Improved retrieval of cloud liquid water from CloudSat and MODIS. *J. Appl. Meteorol.*, **55**, 1831-1844. https://doi.org/10.1175/JAMC-D-16-0077.1.

Lenschow, D.H., I. R. Paluch, A. R. Bandy, et al. (1988). Dynamics and chemistry of marine stratocumulus (DYCOMS) experiment. *Bull. Am. Meteorol. Soc.*, **69**, 1058-1067. https://doi.org/10.1175/1520-0477(1988)069<1058:DACOMS>2.0.CO;2.

Lilly, D. K. (1968). Models of cloud-topped mixed layers under a strong inversion. *Quart. J. Roy. Meteor. Soc.*, **94**, 292-309. https://doi.org/10.1002/qj.49709440106.

Liu, Y., and P. H. Daum. (2004). Parameterization of the autoconversion process. Part I: Analytical formulation of the Kessler-type parameterizations. *J. Atmos. Sci.*, **61**, 1539-1548. https://doi.org/10.1175/1520-0469(2004)061<1539:POTAPI>2.0.CO;2.

Lohmann, U., and J. Feichter. (2001). Can the direct and semi-direct aerosol effect compete with the indirect effect on a global scale?. *Geophys. Res. Lett.*, **28**, 159-161. https://doi.org/10.1029/2000GL01205.

Lohmann, U. (2009). Marine boundary layer clouds, in Surface Ocean-Lower Atmosphere Processes. *Geophys. Monogr. Ser.*, **187**, 57-68. doi:10.1029/2008GM000761.

Luke, E. P., P. Kollias, and M. D. Shupe. (2010). Detection of supercooled liquid in mixed-phase clouds using radar Doppler spectra. *J. Geophys. Res.*, **115**, D19201. doi:10.1029/2009JD012884.

Luke, E. P., and P. Kollias. (2013). Separating cloud and drizzle radar moments during precipitation onset using Doppler spectra. *J. Atmos. Oceanic Technol.*, **30**, 1656-1671. https://doi.org/10.1175/JTECH-D-11-00195.1.

Marchand, R., N. Beagley, S. E. Thompson, et al. (2006). A bootstrap technique for testing the relationship between local-scale radar observations of cloud occurrence and large-scale atmospheric fields. *J. Atmos. Sci.*, **63**, 2813-2830. https://doi.org/10.1175/JAS3772.1.

Marchand, R., J. Haynes, G. G. Mace, et al. (2009). A comparison of simulated cloud radar output from the multiscale modeling framework global climate model with CloudSat cloud radar observations. *J. Geophys. Res. Atmos.*, **114**, D00A20. https://doi.org/10.1029/2008JD009790.

Matrosov, S. Y. (1999). Retrievals of vertical profiles of ice cloud microphysics from radar and IR measurements using tuned regressions between reflectivity and cloud parameters. *J. Geophys. Res.*, **104**, 16741-16753. doi:10.1029/1999JD900244.

Matrosov, S. Y., T. Uttal, and D. A. Hazen. (2004). Evaluation of radar reflectivity-based estimates of water content in stratiform marine clouds. *J. Appl. Meteorol.*, **43**, 405-419. doi:10.1175/1520-0450(2004)043<0405:EORREO>2.0.CO;2.

McCoy, D. T., R. Eastman, D. L. Hartmann, et al. (2017). The change in low cloud cover in a warmed climate inferred from AIRS, MODIS, and ERA-Interim. *J. Clim.*, **30**, 3609-3620. https://doi.org/10.1175/JCLI-D-15-0734.1.

Mellado, J. P. (2017). Cloud-top entrainment in stratocumulus clouds. *Annu. Rev. Fluid Mech.*, **49**, 145-169. https://doi.org/10.1146/annurev-fluid-010816-060231.

Merk, D., H. Deneke, B. Pospichal, et al. (2016). Investigation of the adiabatic assumption for estimating cloud micro- and macrophysical properties from satellite and ground observations. *Atmos. Chem. Phys.*, **16**, 933-952. https://doi.org/10.5194/acp-16-933-2016.

Michibata, T., and T. Takemura. (2015). Evaluation of autoconversion schemes in a single model framework with satellite observations. *J. Geophys. Res. Atmos.*, **120**, 9570-9590. https://doi.org/10.1002/2015JD023818.

Miles, N. L., J. Verlinde, and E. E. Clothiaux. (2000). Cloud droplet size distributions in low-level stratiform clouds. *J. Atmos. Sci.*, **57**, 295-311. https://doi.org/10.1175/1520-0469(2000)057<0295:CDSDIL>2.0.CO;2.

Min, Q., E. Joseph, Y. Lin, et al. (2012). Comparison of MODIS cloud microphysical properties with in-situ measurements over the Southeast Pacific. *Atmos. Chem. Phys.*, **12**, 11,261-11,273. https://doi.org/10.5194/acp-12-11261-2012.

Morrison, H., and A. Gettelman. (2008). A new two-moment bulk stratiform cloud microphysics scheme in the Community Atmosphere Model, version 3 (CAM3). Part I: Description and numerical tests. *J. Clim.*, **21**, 3642-3659. https://doi.org/10.1175/2008JCLI2105.1.

Nam, C. C., and J. Quaas. (2012). Evaluation of clouds and precipitation in the ECHAM5 general circulation model using CALIPSO and CloudSat satellite data. *J. Clim.*, **25**, 4975-4992. https://doi.org/10.1175/JCLI-D-11-00347.1.

Nicholls, S., and J. Leighton. (1986). An observational study of the structure of stratiform cloud sheets: Part I. Structure. *Quart. J. Roy. Meteor. Soc.*, **112**, 431-460. https://doi.org/10.1002/qj.49711247209.

O'Connor, E. J., R. J. Hogan, and A. J. Illingworth. (2005). Retrieving stratocumulus drizzle parameters using Doppler radar and lidar. *J. Appl. Meteorol.*, **44**, 14-27. doi:10.1175/JAM-2181.1.

Ohata, S., N. Moteki, T. Mori, et al. (2016). A key process controlling the wet removal of aerosols: new observational evidence. *Sci. Rep.*, **6**, 34113. https://doi.org/10.1038/srep34113.

Oreopoulos, L., and R. F. Cahalan. (2005). Cloud inhomogeneity from MODIS. *J. Clim.*, **18**, 5110-5124. https://doi.org/10.1175/JCLI3591.1.

Orr, B. W., and R. A. Kropfli. (1999). A method for estimating particle fall velocities from vertically pointing Doppler radar. *J. Atmos. Oceanic Technol.*, **16**, 29-37. https://doi.org/10.1175/1520-0426(1999)016<0029:AMFEPF>2.0.CO;2.

Painemal, D., and P. Zuidema. (2011). Assessment of MODIS cloud effective radius and optical thickness retrievals over the Southeast Pacific with VOCALS-REx in situ measurements. *J. Geophys. Res.*, **116**, D24206. https://doi.org/10.1029/2011JD016155.

Pincus, R., and S. A. Klein. (2000). Unresolved spatial variability and microphysical process rates in large-scale models. *J. Geophys. Res. Atmos.*, **105**, 27059-27065. https://doi.org/10.1029/2000JD900504.

Posselt, R., and U. Lohmann. (2009). Sensitivity of the total anthropogenic aerosol effect to the treatment of rain in a global climate model. *Geophys. Res. Lett.*, **36**, L02805. https://doi.org/10.1029/2008GL035796.

Randall, D. A., J. A. Coakley, C. W. Fairall, et al. (1984). Outlook for research on marine subtropical stratocumulus clouds, *Bull. Amer. Meteor. Soc.*, 65, 1290–1301. https://doi.org/10.1175/1520-0477(1984)065<1290:OFROSM>2.0.CO;2.

Rémillard, J., A.M. Fridlind, A.S. Ackerman, et al. (2017). Use of cloud radar Doppler spectra to evaluate stratocumulus drizzle size distributions in large-eddy simulations with size-resolved microphysics. *J. Appl. Meteorol. Climatol.*, **56**, 3263-3283. https://doi.org/10.1175/JAMC-D-17-0100.1.

Roach, W. T., R. Brown, S. J. Caughey, et al. (1982). A field-study of nocturnal stratocumulus: 1. Mean structure and budgets. *Quart. J. Roy. Meteor. Soc.*, **108,** 103-123. https://doi.org/10.1002/qj.49710845507.

Rosenfeld, D. (1999). TRMM observed first direct evidence of smoke from forest fires inhibiting rainfall. *Geophys. Res. Lett.*, **26**, 3105-3108. doi:https://doi.org/10.1029/1999GL006066.

Rusli, S. P., D. P. Donovan, and H. W. Russchenberg. (2017). Simultaneous and synergistic profiling of cloud and drizzle properties using ground-based observations. *Atmos. Meas. Tech.*, **10**, 4777-4803. https://doi.org/10.5194/amt-10-4777-2017.

Salter, S., G. Sortino, and J. Latham (2008). Sea-going hardware for the cloud albedo method of reversing global warming. *Philos. Trans. R. Soc. A*, **366**, 3989-4006. https://doi.org/10.1098/rsta.2008.0136.

Seifert, A., and K. D. Beheng. (2006). A two-moment cloud microphysics parameterization for mixed-phase clouds. Part 1: Model description. *Meteorol. Atmos. Phys.*, **92**, 45-66. https://doi.org/10.1007/s00703-005-0112-4.

Seinfeld, J. H., C. Bretherton, K. S. Carslaw, et al. (2016). Improving our fundamental understanding of the role of aerosol-cloud interactions in the climate system. *Proc. Nat. Acad. Sci. U.S.A.*, **113**, 5781-5790. https://doi.org/10.1073/pnas.1514043113.

Shupe, M. D., and J. M. Intrieri. (2004). Cloud radiative forcing of the Arctic surface: The influence of clouds properties, surface albedo, and solar zenith angle. *J. Clim.*, **17**, 616-628. doi:10.1175/1520-0442(2004)017<0616:CRFOTA>2.0.CO;2.

Shupe, M. D., P. Kollias, M. Poellot, et al. (2008). On deriving vertical air motions from cloud radar Doppler spectra. *J. Atmos. Oceanic Technol.*, **25**, 547-557. https://doi.org/10.1175/2007JTECHA1007.1.

Slingo, A. (1990). Sensitivity of the Earth's radiation budget to changes in low clouds. *Nature*, **343**, 49-51. https://doi.org/10.1038/343049a0.

Song, H., Z. Zhang, P. L. Ma, et al. (2018). An evaluation of marine boundary layer cloud property simulations in the Community Atmosphere Model using satellite observations: Conventional subgrid parameterization versus CLUBB. *J. Clim.*, **31**, 2299-2320. https://doi.org/10.1175/JCLI-D-17-0277.1.

Stephens, G. L., and T. J. Greenwald. (1991). The Earth's radiation budget and its relation to atmospheric hydrology, 1, Observations of the clear sky greenhouse effect. *J. Geophys. Res.*, **96**, 15325-15340. DOI: 10.1029/91JD00973.

Stephens, G. L. (2005). Cloud feedbacks in the climate system: A critical review. *J. Clim.*, **18**, 237-273. doi:10.1175/JCLI-3243.1.

Stephens, G. L., D. G. Vane, S. Tanelli, et al. (2008). CloudSat mission: Performance and early science after the first year of operation. *J. Geophys. Res. Atmos.*, **113**, D00A18. https://doi.org/10.1029/2008JD009982.

Stephens, G. L., T. L'Ecuyer, R. Forbes, et al. (2010). Dreary state of precipitation in global models. *J. Geophys. Res. Atmos.*, **115**, D24211. https://doi.org/10.1029/2010JD014532.

Stevens, B., D. H. Lenschow, G. Vali, et al. (2003). Dynamics and Chemistry of Marine Stratocumulus-DYCOMS-II. *Bull. Amer. Meteor. Soc.,* **84**, 579-594. https://doi.org/10.1175/BAMS-84-5-579.

Tompkins, A. M. (2002). A prognostic parameterization for the subgrid-scale variability of water vapor and clouds in large-scale models and its use to diagnose cloud cover. *J. Atmos. Sci.*, **59**, 1917-1942. https://doi.org/10.1175/1520-0469(2002)059<1917:APPFTS>2.0.CO;2.

Toto, T., and M. Jensen. (2016). Interpolated sounding and gridded sounding value-added products. No. DOE/SC-ARM-TR-183. Pacific Northwest National Lab.(PNNL), Richland, WA (United States).

Trenberth, K. E. (2011). Changes in precipitation with climate change. *Clim. Res.*, **47**, 123-138. https://doi.org/10.3354/cr00953.

Trenberth, K. E., Y. Zhang, and M. Gehne. (2017). Intermittency in precipitation: Duration, frequency, intensity, and amounts using hourly data. *J. Hydrometeorol.*, **18**, 1393-1412. https://doi.org/10.1175/JHM-D-16-0263.1.

Tripoli, G. J., and W. R. Cotton. (1980). A numerical investigation of several factors contributing to the observed variable intensity of deep convection over south Florida. *J. Appl. Meteorol.*, **19**, 1037-1063. https://doi.org/10.1175/1520-0450(1980)019<1037:ANIOSF>2.0.CO;2.

Twomey, S. (1977). Influence of pollution on shortwave albedo of clouds. *J. Atmos. Sci.*, **34**, 1149-1152. doi:https://doi.org/10.1175/1520-0469(1977)034<1149:TIOPOT>2.0.CO;2.

Wang, Q., and B. A. Albrecht. (1994). Observations of cloud-top entrainment in marine stratocumulus clouds. *J. Atmos. Sci.*, **51**, 1530-1547. https://doi.org/10.1175/1520-0469(1994)051<1530:OOCTEI>2.0.CO;2.

Wang, J., and B. Geerts. (2003). Identifying drizzle within marine stratus with W-band radar reflectivity. *Atmos. Res.*, **69**, 1-27. https://doi.org/10.1016/j.atmosres.2003.08.001.

Wang, J., P. H. Daum, S. S. Yum, et al. (2009). Observations of marine stratocumulus microphysics and implications for processes controlling droplet spectra: Results from the Marine Stratus/Stratocumulus Experiment. *J. Geophys. Res.*, **114**, D18210. doi:10.1029/2008JD011035.

Wang, M., S. Ghan, X. Liu, et al. (2012). Constraining cloud lifetime effects of aerosols using A-Train satellite observations. *Geophys. Res. Lett.*, **39**, L15709. https://doi.org/10.1029/2012GL052204.

Wang, J., X. Dong, and R. Wood. (2016). Aerosol and Cloud Experiments in Eastern North Atlantic (ACE-ENA) Science Plan. No. DOE/SC-ARM-16-006. DOE Office of Science Atmospheric Radiation Measurement (ARM) Program (United States).

Warren, S. G., C. J. Hahn, J. London, et al. (1988). Global distribution of total cloud cover and cloud type amounts over the ocean. No. DOE/ER-0406; NCAR/TN-317-STR. USDOE Office of Energy Research, Washington, DC (USA). Carbon Dioxide Research Div.; National Center for Atmospheric Research, Boulder, CO (USA), 1988.

Weber, T., and J. Quaas. (2012). Incorporating the subgrid-scale variability of clouds in the autoconversion parameterization using a PDF-scheme. *J. Adv. Model. Earth. Sy.*, **4**, M11003. https://doi.org/10.1029/2012MS000156.

Witte, M. K., P. Y. Chuang, O. Ayala, et al. (2019). Comparison of Observed and Simulated Drop Size Distributions from Large-Eddy Simulations with Bin Microphysics. *Mon. Weather Rev.*, **147**, 477-493. https://doi.org/10.1175/MWR-D-18-0242.1.

Wood, R., P. R. Field, and W. R. Cotton. (2002). Autoconversion rate bias in stratiform boundary layer cloud parameterizations. *Atmos. Res.*, **65**, 109-128. https://doi.org/10.1016/S0169-8095(02)00071-6.

Wood, R. (2005a). Drizzle in stratiform boundary layer clouds. Part I: Vertical and horizontal structure. *J. Atmos. Sci.*, **62**, 3011-3033. https://doi.org/10.1175/JAS3529.1.

Wood, R. (2005b). Drizzle in stratiform boundary layer clouds. Part II: Microphysical aspects. *J. Atmos. Sci.*, **62**, 3034-3050. https://doi.org/10.1175/JAS3530.1.

Wood, R., and C. S. Bretherton. (2006). On the relationship between stratiform low cloud cover and lower-tropospheric stability. *J. Clim.*, **19**, 6425-6432. https://doi.org/10.1175/JCLI3988.1.

Wood, R., and D. L. Hartmann. (2006). Spatial variability of liquid water path in marine low cloud: The importance of mesoscale cellular convection. *J. Clim.*, **19**, 1748-1764. https://doi.org/10.1175/JCLI3702.1.

Wood, R. (2012). Stratocumulus clouds. *Mon. Weather Rev.*, **140**, 2373-2423. https://doi.org/10.1175/MWR-D-11-00121.1.

Wood, R., M. Wyant, C.S. Bretherton, et al. (2015). Clouds, aerosols, and precipitation in the marine boundary layer: An arm mobile facility deployment. *Bull. Am. Meteorol. Soc.*, **96**, 419-440. https://doi.org/10.1175/BAMS-D-13-00180.1.

Wu, P., X. Dong, and B. Xi. (2015). Marine boundary layer drizzle properties and their impact on cloud property retrieval. *Atmos. Meas. Tech.*, **8**, 3555-3562. https://doi.org/10.5194/amt-8-3555-2015.

Wu, P., B. Xi, X. Dong, et al. (2018). Evaluation of autoconversion and accretion enhancement factors in general circulation model warm-rain parameterizations using ground-based measurements over the Azores. *Atmos*. *Chem*. *Phys*., **18**, 17405-17420. https://doi.org/10.5194/acp-18-17405-2018.

Yuan, J., Q. Fu, and N. McFarlane. (2006). Tests and improvements of GCM cloud parameterizations using the CCCMA SCM with the SHEBA data set. *Atmos*. *Res*., **82**, 222-238. https://doi.org/10.1016/j.atmosres.2005.10.009.

Zhang, Z., H. Song, P. L. Ma, et al. (2019). Subgrid Variations of the Cloud Water and Droplet Number Concentration Over Tropical Ocean: Satellite Observations and Implications for Warm Rain Simulation in Climate Models. *Atmos*. *Chem*. *Phys*., **1919**, 1077-1096. https://doi.org/10.5194/acp-19-1077-2019.

Zhao, W., R. Marchand, and Q. Fu. (2017). The diurnal cycle of clouds and precipitation at the ARM SGP site: Cloud radar observations and simulations from the multiscale modeling framework. *J. Geophys. Res. Atmos.*, **122**, 7519-7536. https://doi.org/10.1002/2016JD026353.

Zheng, Y., D. Rosenfeld, Y. Zhu, et al. (2019). Satellite-based estimation of cloud top radiative cooling rate for marine stratocumulus. *Geophys*. *Res*. *Lett*., **46**, 4485-4494. https://doi.org/10.1029/2019GL082094.

Zhou, X., and C. S. Bretherton. (2019). Simulation of mesoscale cellular convection in marine stratocumulus: 2. Nondrizzling conditions. *J. Adv. Model. Earth. Sy.*, **11**, 3-18. https://doi.org/10.1029/2018MS001448.